UNIVERSITY OF OKLAHOMA

GRADUATE COLLEGE

ASSESSMENT OF SPECTRAL ATTRIBUTES IN IDENTIFYING GAS
HYDRATES IN SEISMIC DATA FROM THE PEGASUS BASIN, OFFSHORE
NEW ZEALAND

A THESIS

SUBMITTED TO THE GRADUATE FACULTY

in partial fulfillment of the requirements for the

Degree of

MASTER OF SCIENCE

BY

EMILY R JACKSON

Norman, Oklahoma

2023

ASSESSMENT OF SPECTRAL ATTRIBUTES IN IDENTIFYING GAS
HYDRATES IN SEISMIC DATA FROM THE PEGASUS BASIN, OFFSHORE
NEW ZEALAND

A THESIS APPROVED FOR THE
SCHOOL OF GEOSCIENCES

BY

THE COMMITTEE CONSISTING OF

Dr. Heather Bedle, Chair

Dr. Matt Pranter

Dr. Megan Elwood-Madden

Acknowledgements

including me in your lives and showing me how special our diverse group is: Alex, Diana, Pamela, Bobby, April, Ahmet, Marcus, Ryan, Dai, Evan, and Jake. Best of luck to you all and Boomer Sooner!

To Dr. Pranter and Dr. Megan Elwood Madden, thank you for serving on my committee. Dr. Pranter, your reservoir characterization final project was one of the hardest I've ever completed, but I felt like a better geologist for it; thank you for letting me learn from you. Dr. Elwood Madden, thank you for all the help understanding the fascinating world of hydrates better. I value each of your unique insight into my project and the time commitment you made to serve on my committee.

To my former professor Dr. Dengliang Gao at West Virginia University, thank you for getting me interested in geophysics and seismic attributes in the first place.

Finally, to each of my loved ones, especially those hundreds of miles away, that may never read this thesis or understand what gas hydrates are, thank you for helping me see that my life isn't all about success or the degrees I have but about the relationships I form and people I meet as I follow where the Lord leads me. Thank you for being present for me even when it was inconvenient for you or required a couple plane rides, listening to me cry over the phone, or giving me a place to stay over the summer. A big shout out to my sister Elizabeth, Drew, my dear friends in West Virginia, Danielle, my family, and my church in Moore, OK. To those that tirelessly supported me and encouraged me to stick to my values, find joy in the everyday, choose gratitude in the midst of hardship, and to stay rooted in my identity in Christ: this is for you.

"If we knew what it was we were doing, it would not be called research, would it?" -Einstein

Table of Contents

Chapter 1: Assessment of spectral attributes in identifying gas hydrates in seismic data from the Pegasus basin, offshore New Zealand

Chapter 2: Synthetic seismic study and application of spectral attributes to analyze attenuation response in gas hydrates

List of Figures

Figure 1-12. 2D color map and 2D histogram from APB13 line # 38 far angle stack seismic line. The 2D histogram represents the clusters of facies, and also helps visualize the connectivity or "distance" the individual facies have from each other

Figure 1-13. a full stack seismic line with high and low amplitude BSRs, **b** SOM results calculated from the full stack seismic line, **c** SOM results calculated from the far angle stack, and **d** SOM results calculated from the near angle stack; seafloor bathymetry map from GeoMapApp

Figure 1-14. a full stack seismic line showing high and low amplitude BSRs, **b** SOM results calculated from the full stack seismic line between the ocean bottom and BSR horizons, **c** SOM results calculated from the far angle stack seismic line between the ocean bottom and BSR horizons, and **d** SOM results calculated from the near angle stack seismic line between the ocean bottom and BSR horizons; seafloor bathymetry map from GeoMapApp

Figure 2-1. Synthetic seismic trace and well logs. Track 1, time (ms); track 2, Ricker wavelet at 45 Hz; track 3, statistical wavelet; track 4, density (g/cm^3); track 5, p-wave velocity (m/s); track 6, gas hydrate saturation (%) within the pore space of the rock, with the remaining percentage filled with water; track 7, s-wave velocity (m/s); and track 8, TVD measured from 0 ft below surface

Figure 2-2. a seismic amplitude with Ricker and statistical wavelets, and lithology and gas hydrate saturation sequence, **b** spectral skewness with Ricker and statistical wavelets, and **c** spectral kurtosis with Ricker and statistical wavelets

Figure 2-3. a mean frequency, in Hertz, with Ricker and statistical wavelets, and **b** spectral bandwidth, in cycles per second with Ricker and statistical wavelets

Figure 2-4. a seismic amplitude with Ricker and statistical wavelets, and lithology and gas hydrate saturation sequence, **b** spectral skewness with Ormsby and statistical wavelets, and **c** spectral kurtosis with Ormsby and statistical wavelets

Figure 2-5 a mean frequency, in Hertz, and **b** spectral bandwidth, in cycles per second for the Ormsby wavelet scenario

List of Tables

Abstract

Gas hydrates are formed in the subsurface along shallow ocean basins or in permafrost settings, and are commonly identified in the seismic data by the bottom-simulating reflector (BSR). Various methods have been employed in the past to measure gas hydrates from lab analyses, well log, or velocity data, but few studies have demonstrated methods to identify gas hydrates in seismic data when the BSR is sparse or lacking. One approach is to measure the expected attenuation, or the reduction in the seismic waveform, caused by hydrates in the gas hydrate stability zone (GHSZ). This study proposes the application of two statistical attributes—skewness and kurtosis—that measure the asymmetry of the seismic amplitude spectrum in order to quantify the attenuation responses throughout the GHSZ. Although the study area does not contain well log data, there are numerous studies that confirm hydrates exist throughout the Pegasus Basin. These attributes, in addition to other instantaneous and amplitude-related attributes, demonstrate that frequency-related variations are the major contributors to attenuation response, rather than seismic amplitude or geology effects. The spectral attribute results show that strong positive skewness and kurtosis variations above the high amplitude BSR is likely due to attenuation through an interval of hydrates. Negative skewness and kurtosis may correspond to an interval that does not contain hydrates, therefore suggesting that the GHSZ in the Pegasus Basin consists of discontinuous intervals of hydrates, rather than one continuous layer from ocean bottom to BSR.

Chapter 1, Assessment of spectral attributes in identifying gas hydrates in seismic data from the Pegasus Basin, offshore New Zealand

1. Introduction

Methane gas hydrates are emerging as a new energy horizon and have significant impact on engineering, climate, and energy resources. Hydrates can pose significant risk during drilling oil and gas wells, and while shear strength of the sediment increases with hydrate accumulation, dissociation of hydrates can lead to seafloor instability or slumping (Chand and Minshull, 2004), and hydrates also have implications for climate concerns if they become destabilized and released into the ocean (Maslin et al., 2010). Estimates for global hydrate accumulations are 250,000 Tcf, which is nearly 90% higher than natural gas estimates for the United States alone (NETL, 2020), demonstrating the enormous magnitude of hydrates that exist globally. Nonetheless, the extent of hydrates and exact regimes of occurrence still contains significant uncertainty.

Gas hydrates form in the shallow subsurface off-shore or in permafrost regimes at higher latitudes. They form under constrained high pressure and low temperature settings when water molecules trap gas molecules (usually methane) and freeze, forming a solid hydrate structure (Sloan, 2003). The pore-filling hydrates can form a seal, trapping migrating free gas in the zone below where hydrates fill the pore space of the rocks. The theoretical zone, modelled based on local pressure and temperature regimes, where hydrates are stable is called the gas hydrate stability zone (GHSZ), and its base is sometimes signaled by an anomalous seismic reflector referred to as the bottom simulating reflector (BSR). In seismic, the BSR is observed as a negative impedance contrast between the hydrate-filled sediment zone and the free gas in the underlying zone (Singh et al., 1993; Dev and McMechan, 2010; Davies et al., 2021). BSRs, which have the opposite seismic polarity of the ocean bottom reflector, are perhaps most evident when they cross-cut

stratigraphy, and they roughly parallel the ocean bottom (Hornbach et al., 2003) due to the temperature (which is related to depth below seafloor) constraints under which hydrates form (Dvorkin et al., 2014). While the presence of a BSR is good indicator that hydrates exist in the subsurface, BSRs do not directly indicate the *concentration* of gas hydrate accumulations (Holbrook et al., 1996; Boswell et al., 2005) as BSRs can also be due to processes unrelated to gas hydrate accumulation and trapped free gas (Sloan, 2003) such as diagenesis of opalA to opal CT (Berndt et al., 2000). The absence of BSRs can be due to lack of migrating gas in the system, failure of the hydrates to trap free gas, or depending on lithology, the impedance contrast between the hydrate filled sediments and non-hydrate filled sediments may not be large enough for a seismic reflector (Bedle, 2019). Weak, discontinuous, or absent BSRs complicate the process of identifying hydrates and require implementing other methods to image the extent of the gas hydrates (Chenin and Bedle, 2020; Clairmont et al., 2021). Therefore, relying on clear BSRs alone in seismic data is unreliable (Holbrook et al., 1996), and other methods are often needed to confirm the existence of gas hydrates within the GHSZ.

A new method of detecting gas hydrates in seismic data is to use spectral shape seismic attributes to measure the attenuation in seismic frequencies that are caused by gas hydrates within the gas hydrate stability zone. Seismic frequencies naturally attenuate with depth; however, hydrates also attenuate the seismic frequencies, although the exact mechanism has proven complex (Chand et al., 2004; Dvorkin et al., 2014) and will be discussed in detail in a later section. The attenuation of the seismic frequency should be visible in the seismic amplitude spectrum, which can be computed across the entire seismic dataset, or limited to a zone above, in, or below the GHSZ. Gas hydrates are shown to attenuate seismic waves from numerous seismic or well studies (Guerin and Goldberg, 2002; Chand and Minshull, 2004; Dvorkin and Uden, 2004; Sahoo et al,

2019, and others), and this effect is even observed in synthetic seismic data created from real-world, hydrate-bearing well log data (Dvorkin et al, 2014). To quantify the attenuation response for hydrocarbon accumulations, Li et al. (2015 and 2016) proposed skewness and kurtosis, two statistical measures, in combination with five other attenuation-related attributes, to measure attenuation in hydrocarbon-filled sediments in both conventional and unconventional reservoirs. Their research showed that the high attenuation generally correlated with high productivity in the gas-producing regions, but noted that while these attributes point to high-frequency energy reduction, there is no one-to-one correlation between attenuation and gas presence since reservoirs are largely complex. These statistical attributes Li et al. applied are called "shape attributes" and measure the shape of the seismic amplitude spectrum. Although these spectral attributes have not previously been applied to measure attenuation within hydrates, instantaneous and AVO attributes have proven useful for evaluation of gas hydrate-bearing sediment (Wang et al., submitted 2023; Clairmont et al., 2021), and are incorporated with skewness and kurtosis into unsupervised machine learning to further identify gas hydrates in seismic data in the absence of BSRs or other clear direct hydrocarbon indicators (DHIs).

The goal of this study is to 1) determine whether or not skewness and kurtosis are useful attributes for measuring attenuation related to gas hydrate accumulation in the GHSZ and can therefore serve as hydrate indicators, and 2) implement unsupervised machine learning based on spectral-, amplitude-, and frequency-related attributes to enhance attenuation-related responses and variations visible in the selected attributes.

1.1 Physical Characteristics of Gas Hydrates

Gas hydrates, chemically described as clathrate hydrates, were first discovered in 1810 by Sir Humphry Davy, but their significance was disregarded until the mid-20th century when hydrates were recognized as an engineering concern due to well-bore plugging within the oil and gas industry (Engeloz, 1993; Rieldel et al., 2010). Hydrogen-bonded water molecules form the lattice of the clathrate structure, in which the "guest" or methane molecule is enclosed (Engeloz, 1993). The configuration of the chemical lattice can vary across three main structures (I, II and H) of clathrates, with a simple methane hydrate classified as type I (Riedel et al, 2010).

	V_p (km/s)	V_s (km/s)	Density (g/cm^3)
Gas Hydrates	3.6	1.9	0.91
Ice	3.89	1.97	0.917
Gas Sands	2.857	1.666	2.275
Water Sands	4.01	2.41	2.37
Shales	2.898	1.29	2.425

Table 1. V_p, V_s, and densities for gas hydrates, shales, gas-filled sandstones, water-filled sandstones, and ice. References from Dvorkin et al., 2014, Helgerud, 2001, Goodway, 2001, Mavko et al., 2013, and Han et al., 1986.

Methane hydrates have similar physical properties to ice (see properties in Table 1) and subsequently, hydrates behave as a solid and therefore increase the rigidity of the hydrate-filled sediments, as opposed to water- or brine-filled sediments. Furthermore, hydrates increase the resistivity of a formation compared to water- or bring-filled sediments (Riedel et al., 2010) while reducing porosity due to hydrate filling pore space, which has an effect on the velocities and elastic moduli of the hydrate-filled rock (Dvorkin et al., 2014). Two separate models for hydrate occurrence within sediment pore space were described by Dvorkin et al. (2014) and constitute 1) hydrates existing within the *mineral frame* of the pore space and 2) hydrates existing in the *pore fluid* of the pore space. In the first model, the elastic moduli and velocity are impacted by gas hydrates within the new solid mineral frame. In the second model, the elastic moduli (and

therefore, shear modulus) of the mineral frame is not impacted by hydrate presence since hydrates are contained only within the pore fluid, separate from the mineral frame, therefore impacting only the bulk modulus of the pore fluid. S-wave velocities have been widely shown to increase along with P-wave, ruling out the likelihood of model 2. Whichever model is applied, the reduction in porosity due to hydrates leads to the increase in velocity and consequently, elastic moduli (Dvorkin et al., 2014).

1.2 Seismic Attenuation Associated with Gas Hydrates

Attenuation is energy loss exhibited in the seismic signal, and is denoted by the quality factor, Q, which is inverse attenuation (Riedel et al., 2010). Attenuation is expected to result in a reduction in higher-frequencies over low-frequencies (Raikes and White, 1984), and there is evidence of a low-velocity shadow zone (LVSZ) below high attenuation zones associated with hydrates (Taylor et al., 2000) and other types of gas accumulations (Castagna et a.l, 2003). Although there are several mechanisms proposed for attenuation, the exact nature of attenuation within hydrates is not yet fully realized since the attenuation responses have proven to be complex (Dvorkin et al., 2014; Riedel et al., 2010) and lacking a clear one-to-one correlation between hydrate saturation and attenuation (Liu et al, 2022 and references therein). Furthermore, while there is evidence that attenuation increases with stiffer rock (Klimentos and McCann, 1990 and others), there is less research that supports the same effect in hydrates, though one might expect lower attenuation due to lower energy loss in hydrate-filled sediments (from porosity reduction). Rather, opposite effect of increasing attenuation with hydrate saturation is overwhelmingly observed (Guerin and Goldberg, 2002; Chand and Minshull, 2004; Dvorkin and Uden, 2004, Riedel et al., 2010, and references therein; Dvorkin et al., 2014 and references therein; Zhan and Matsushuma, 2018; Sahoo et al., 2019), to the extent that some researcher advocate for attenuation

to be considered within the realm of physics-driven seismic attributes for both conventional and unconventional reservoir characterization (Dvorkin and Mavko, 2006) and methane hydrate reservoir characterization (Cordon et al., 2006).

1.2.1 The Current Understanding of the Geophysical Impact from Gas Hydrates

Although significant research has been conducted on hydrates and their impact on seismic wave velocities and frequencies, fewer studies have shown the impact of attenuation related to hydrates in 2D or 3D seismic surveys. Much of the research on hydrates has been from well logs, synthetic data, or laboratory studies. A selection of studies on gas hydrates and attenuation are detailed below to give the current state of attenuation-focused gas hydrate research. Proposed mechanisms are discussed in the following section.

A laboratory study using a resonant column to study in-situ hydrates within sands, conducted by Best et al (2010) showed that hydrate saturation between 0-5% resulted in the largest attenuation ($1/Q$) values, after which attenuation decreased up to approximately 18% hydrate saturation, then increased to 35% hydrate saturation (no data was reported after 35% hydrate saturation). In contrast to attenuation, both P-wave and S-wave velocities increased with hydrate saturation up to 35%, although at a slower rate following 3-5% hydrate saturation, which the author attribute to rapid cementation of hydrates between 3-5% hydrate saturation resulting in a higher rate of velocity increase below 3%. Furthermore, the authors noted that higher attenuation occurred within solidified methane hydrates compared to methane gas after hydrate dissociation.

A study by Liu et al. (2022) used seismic data from a deep-water setting and corresponding rock physics equations to calculate P-wave attenuation through three modes of hydrate occurrence: suspension (hydrates within the pore fluid), particle-contact (hydrates as part of the solid frame of the rock/mineral), and cementation (hydrates acting as cement along the mineral grains) with

varying models for calculating the elastic properties within the rock. The authors found that for the suspension mode of hydrate occurrence, attenuation of P-wave velocities were correlated with hydrate saturation, while for the particle-contact and cemented modes of hydrate occurrence, P-wave velocities were inversely correlated with hydrate saturation.

Numerous reports and studies (Uchida et al., 1999; Walia et al., 1999; Guerin and Goldberg, 2002; Chand and Minshull, 2004; Dvorkin, and Uden 2004; Cordon et al, 2006; and others) have been conducted on the JAPEX/JNOC/GSC Mallik 2L-28 well in the Mackenzie Delta, Northwest Territories, Canada. The Mallik 2L-28 well was drilled in 1998 through a joint operation by the Japan Petroleum Exploration Company (JAPEX), Geological Survey of Canada (GSC), and the Japan National Oil Corporation (JNOC) for the purpose of investigating permafrost-related gas hydrates suspected to occur at the well location (Dallimore et al., 1999). In addition to drilling and coring activities through the permafrost and hydrate-bearing sand-clay-silt layers (Riedel et al, 2010), a seismic, VSP (vertical seismic profiling), geophysical logging, and electromagnetic surveys have also been conducted at the Mallik 2L-38 well location (Walia et al., 1999). One study that constructed a set of synthetic seismic data based on properties in the Mallik well and applied a Q^{-1} parameter showed that higher frequencies (50 Hz) exhibited greater reduction in amplitude than did lower frequencies (20 and 30 Hz) when compared to the same synthetic seismic with no Q^{-1} factor applied (Cordon et al, 2006). Another study showed that hydrate saturation resulted in increased attenuation seen in the P-wave velocity measured from cross hole tomography and sonic logging (Chand and Minshull, 2004), while yet another showed that even low hydrate saturation resulted in amplitude losses while simultaneously increasing both compressional and shear velocities due to stiffening of the pore space (Guerin and Goldberg, 2002).

1.2.2 Proposed Mechanisms for Attenuation in Gas Hydrates

In order to describe the complexities of attenuation in a hydrate setting, several proposed mechanisms for attenuation have been used to model the response seen in the well, seismic, or synthetic data. White (1975) proposed the patchy-saturation model of attenuation that states that the uneven or "patchy" saturation of a rock increases the pressure gradient and fluid flow against the grain matrices of a rock, resulting in more energy loss of the seismic wave, and therefore, higher attenuation than in a homogeneously saturated rock. Liu et al. (2022) applied the patchy saturation model of attenuation to determine attenuation characteristics across three modes of hydrate occurrence: suspension, cementation, and particle-contact. The results from the Liu et al study found that while the attenuation response was directly correlated to hydrate saturation for the suspension mode, the mode of hydrate occurrence and how the mode impacted the strength and cementation of the hydrates, and subsequently, the differential fluid flow caused by heterogeneities in the patchy-saturated sediment, had the greatest effect on attenuation of the P-wave velocities.

Other proposed mechanisms for attenuation are the macroscopic fluid flow proposed by Biot (1956a and 1956b) and squirt flow mechanism proposed by Mavko and Nur (1975). Biot states that energy loss results from fluid flow within the pore space (caused by shear stress within the fluid) against a compressible medium that has been deformed by an acoustic wave. The amount of dissipation that occurs is related to the skin depth (distance from the pore wall) and is dependent on frequency, with intermediate frequencies causing the highest dissipation rates (Winkler and Nur, 1982). The squirt flow mechanism states that attenuation occurs when compression of

saturated sediments causes flow between non-parallel cracks of the rock (Mavko and Nur, 1975). The macroscopic fluid flow, or Biot model, was combined with the squirt-flow mechanism by Dvorkin and Nur (1993), resulting in the BISQ model of attenuation which combines attenuation at different scales (Chand and Minshull, 2004). The BISQ method describes attenuation from deformation of pore spaces which results in energy loss with stress dissipation, and compression of micro-cracks that causes energy loss with flow between the cracks (Chand and Minshull, 2004; Sahoo et al., 2019). A study by Chand and Minshull (2004) applied the BISQ method to the Mallik 2L-38 well in the McKenzie Delta, Canada, and found that hydrate saturation resulted in increased attenuation up to a peak frequency. These studies illustrate the complex nature of attenuation and that attenuation effects from hydrates should be observable in seismic or well data and related frequency spectra.

Generalizing several other findings, research has shown that higher friction or diffusion within the pore fluid resulting from elastic heterogeneities and squirt-flow mechanisms could be two compelling reasons for increasing attenuation in hydrate settings (Riedel et al., 2010, and references therein). Furthermore, Guerin and Goldberg (2002) argued that the complex nature of attenuation within hydrates may be better understood not in terms of porosity and velocity fluctuations, but by pore-scale interactions, some of which are described by the Liu et al. (2022) study. Regardless of the exact mechanism, increased attenuation, often observed by reduction of p- and s-wave amplitudes in a gas hydrate setting, has been widely reported. Based on these previously discussed findings and the current understanding of attenuation in hydrates, observing increased attenuation due to known presence of gas hydrates in the Pegasus Basin is a primary objective of this study.

1.3 Attribute and Attenuation Variation with Angle

A unique aspect of this project is that it gives the opportunity to study how attenuation effects may be seen at different angles in the seismic reflection data. While this is not strictly an amplitude variation with offset (AVO) or angle (AVA), there are expected variations between a full stack, near angle stack, or far angle stack. The frequency content is expected to vary from the far to near angle stacks; while there is naturally occurring attenuation in the far angle stacks as the seismic wave travels further through the earth to those angle location, there may also be impacts from NMO (normal move-out) corrections resulting in reduced frequency in the far angle stacks (Hilterman and Van Schuyver, 2003). This may impact skewness and kurtosis response across the different angles as the spectrum will subsequently be impacted by the degree of attenuation of the seismic frequencies.
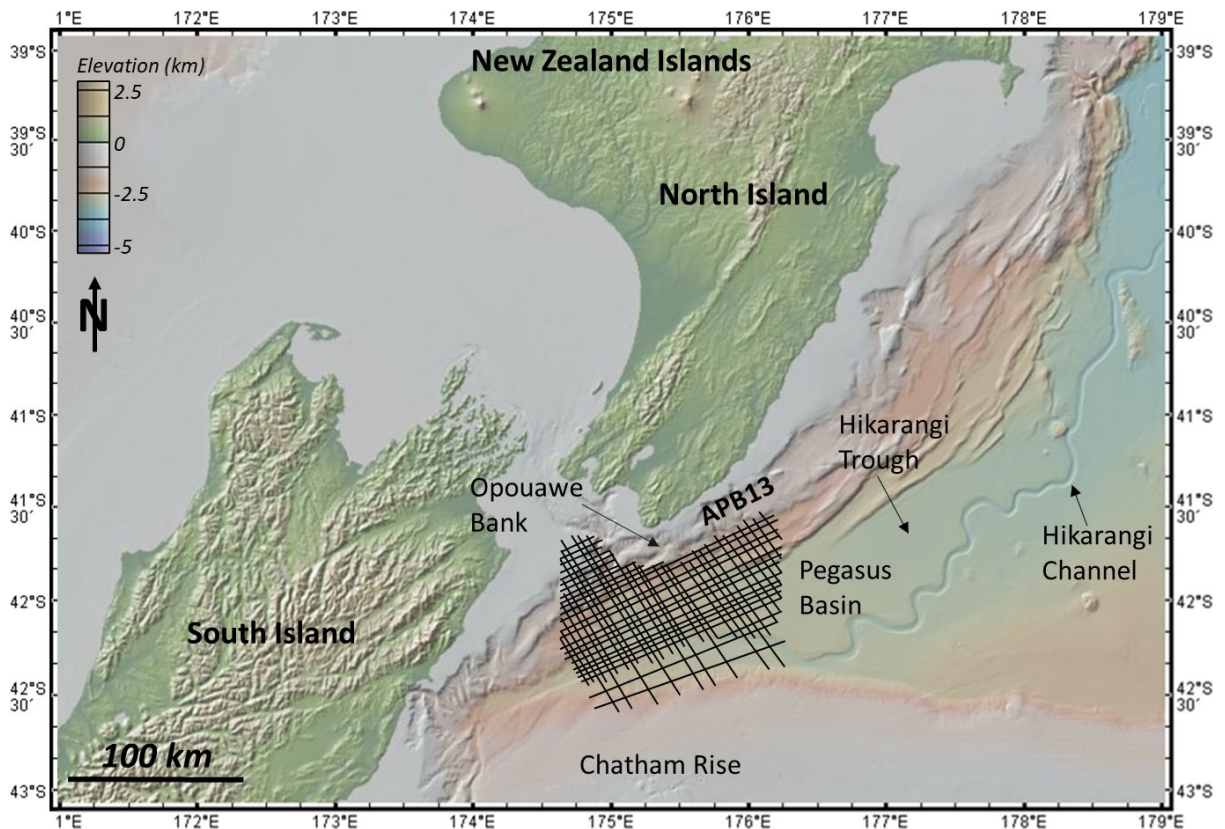
Fig. 1 Pegasus Basin and ABP13 2D seismic survey location, offshore New Zealand. All bathymetry maps herein are created from GeoMapApp (2023)

2. Geologic Setting of the Pegasus Basin

2.1 Structural Setting and Basin History

The Pegasus Basin is a triangular-shaped basin located offshore New Zealand between the North Island and the Chatham Rise (Figure 1). The area is characterized by a series of NE-SW trending reverse and strike-slip faulting which represent the convergence of and subduction zone between the Pacific plate to the northeast and the Australian plate to the southwest. Along the North Islands, the Hikurangi Trough serves as the boundary between the subducting Pacific plate, forming a thrust fault as the Pacific plate subducts below the North Island, while to the southwest, the Alpine Fault comprises a series of left-lateral strike-slip faults along the plate boundary which cuts across the northern South Island and then parallels the western extent of the island. Along the southern border of the Hikurangi Trough is the Chatham Rise, an east-west linear bathymetric feature that is remnant from the once-active eastern margin of Gondwana (Bland et al., 2015; King, 2017). Within the Hikurangi Trough is the Hikurangi Channel, which is sourced by sediments from the Southern Alps (Kroeger et al., 2015). Overall, the Pegasus Basin covers an area of approximately 25,000 km^2, although the eastern extent of the basin is not covered by seismic surveys such that the true size of the basin could be nearly double. While the deepest part of the Pegasus Basin is over 3000 meters below seafloor (mbsf) in the northeastern end, the average depth is 1000-1500 mbsf (Bland et al., 2015). The vertical and horizontal extent of hydrates and the occurrence over a subduction zone with thermogenic and biogenic methane sources make this an excellent basin to study the seismic expression of hydrates.

2.2 Stratigraphy

Within the Pegasus Basin, the stratigraphy is considerably enigmatic since there is no well control in the basin, with the closest well 150-200 km away in the East Coast Basin, located

11

to the northwest of the Hikurangi Trough. Nevertheless, seismic data acquired over the past few decades, as well as bathymetry and core (gravity and piston) data have proven useful to interpretations of the stratigraphy throughout the Pegasus Basin, which is predominately interpreted as mixed siliciclastics (mudstone, siltstone, and sandstone) from turbidite deposits (Lewis and Pantin, 2002) or seafloor current deposits (Kroeger et al., 2015, and references therein), with evidence of sediment waves and levee deposits in relation to the paleo-Hikarangi Channel (Lewis and Pantin, 2002). Additionally, studies have been conducted to tie the stratigraphy from the nearby wells, which penetrated into Middle and Late Miocene rocks, to the Pegasus Basin, although given the distance to nearby wells, significant uncertainty exists (Bland et al., 2015). However, Collier (2015) tied Cretaceous-Neogene outcrops onshore New Zealand to seismic data from the PEG09 2D seismic survey. This study characterized the Cretaceous rocks of the Pegasus Basin as being undeformed, mixed siliciclastics, primarily from fan-delta deposits, which overlie the chaotic basement reflectors of the metasedimentary Torlesse Supergroup (Uruski and Bland, 2011). There is also evidence of Early Cretaceous coal beds, suggested from several high-amplitude seismic reflectors. The thin interval of Paleogene rocks shows more signs of deformation than the underlying Cretaceous facies, and represents a sediment-starved time in Pegasus Basin history. Several large impedance contrasts seen in the seismic used in the Collier study are interpreted to represent major changes in lithology, and Paleogene lithology inferred from onshore outcrop analogs varies from pelagic limestones to paleosols and karsts to clastic sediments. Finally, in the late Neogene, sedimentation rates were higher and resulted in thicker sediment packages in the basin. From the seismic, the Miocene deposits are interpreted as flysch deposits based on their seismic response (continuous, high-

frequency reflectors), and a "cut-and-fill" geometry that indicates coarse-grained channel deposits (Collier, 2015).

2.3 Hydrate Studies in the Pegasus Basin

Hydrates have been recovered along the Opouawe Bank in the Pegasus Basin by the IMG-GEOMAR NEMESYS cruise in 2011 which sought to map the extent of the active methane seepage along the Hikurangi Margin (Bialas, 2011; see map inset in Figure 5). In addition to the hydrates that occur deeper in the subsurface at Pegasus Basin, hydrates have also been recovered from gravity cores in the Hikurangi subduction margin (Plaza-Faverola et al., 2015). A recent study conducted over the Pegasus Basin showed that seismic attributes and machine learning can help detect weak and discontinuous BSRs (Chenin and Bedle, 2020). This research utilized principal-component analysis (PCA) to identify seismic attributes that contributed most to variability in the seismic, with the focus on the shallow hydrate zones. The attributes that were characterized by the PCA (instantaneous frequency, sweetness, thin bed, fluid factor, and gas indicator) were then used as input into an unsupervised machine learning algorithm (SOMs) to cluster the data into meaningful fields and enhance the weak and or discontinuous BSR identified in the PEG09 and APB13 seismic survey 2D lines. Another study (Clairmont et al., 2021) over the Pegasus Basin used primarily frequency attributes (instantaneous frequency and sweetness) and spectral decomposition to resolve weak BSRs, and sparse-spike decomposition to estimate the quality factor, Q, which is the inverse of attenuation. The results showed that the frequency-related attributes helped identify gas-saturated zones below the BSRs and the spectral decomposition helped differentiate the low-frequency shadow zones and BSRs from the background seismic, while the Q-estimation gave clues as to gas accumulation below the identifiable, high amplitude BSRs.

While many studies and researchers rely on the BSR as a primary indicator of gas hydrates and have even shown that BSRs can be enhanced through careful seismic attribute selection and machine learning, there are very few studies that attempt to detect gas hydrates from attenuation alone, especially in systems where a BSR or other direct hydrocarbon indicators may be absent. As is shown from these studies, hydrates can exist in systems that lack a clear BSR, and when well data is unavailable, quantifying attenuation through seismic attributes may prove to be the most compelling evidence of hydrates, in addition to being a straightforward and cost-effective alternative to acquiring well or core data. The presence of high amplitude BSRs in conjunction with low amplitude, weak, and or discontinuous BSRs seen in seismic data, as well as core reports indicating the presence of hydrates throughout the basin, makes the Pegasus Basin a valuable study area to delineate the statistical attributes' ability to quantify attenuation across a variety of geophysical expressions of hydrates, while in a relatively homogeneous geologic setting.

2.4 Available Data

The Explora survey over the Pegasus Basin was acquired in the 1990s, the 'PEG09' survey in 2009-2010 (Bland et al., 2015), and the 'APB-13' data that was acquired by Anadarko New Zealand Ltd in 2014. The APB-13 dataset was chosen for this study because it was higher-resolution than the PEG09 dataset. The APB-13 dataset contained 56 2D lines and 648 traces surveyed at a record length of 10,500 ms at a sample rate of 2 ms, and the SP interval was 37.5 m (New Zealand Petroleum & Minerals Report PR5169, 2014). The data was processed by CGG Services (Singapore) Pte Ltd in 2014 using a full Kirchhoff pre-stack time migration (PTSM) and a post-stack processing utilizing Q-compensation and time variant scaling (New Zealand Petroleum & Minerals Report PR5170). The seismic data is normal SEG polarity with the ocean

bottom being a strong peak seismic reflector. In addition to the full stack data, the near (NAS), mid (MAS), and far (FAS) angle stacks are also available, and incorporated into this project for additional analysis at varying angles. The range for the individual angle stacks is as follows: 5-18° for the near angle stack, 18-32° for the middle angle stack, 32-45° for the far angle stack, and an inner/outer mute of 40° for the full angle stack (New Zealand Petroleum & Minerals Report PR5170, 2014). While the middle angle stacks are available, for this research, they were not utilized as there is not expected to be a significant response due to angle offset seen in the middle angles.

Although there is no available well data in the Pegasus Basin due to lack of drilling, the presence of gas hydrates has been confirmed by seafloor cores (see map inset in Figure 5; Bialas, 2011; Plaza-Faverola et al., 2015) from the IMF-GEOMAR cruise in 2011, and indicators of gas hydrates can be clearly seen in the seismic amplitude data, making the APB-13 seismic survey a valuable asset in determining attenuation through hydrates.
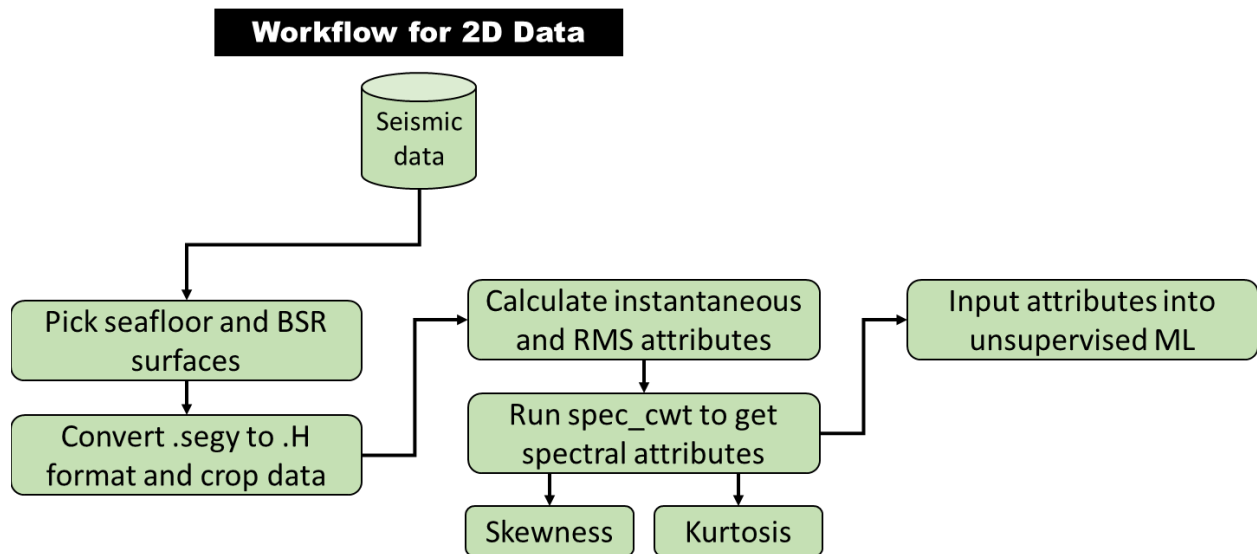
Fig. 2 Project methodology and workflow for seismic data handling, attribute calculation, and machine learning implementation

3. Methods

When gas hydrates exist within the gas hydrate stability zone, there may or may not be a BSR that visually signals the presence of hydrates. When a BSR is not present, other methods are required to identify hydrates in seismic data. The goal of this research is to use seismic attributes, specifically those related to attenuation, and therefore, frequency, to determine the nature of the attenuation response due to hydrate presence in the system. The first step to measuring attenuation with spectral shape attributes is to show how these attributes behave on synthetic seismic data created from rock physics properties. This allows for testing the attributes before applying them to real-world data, and sets up a framework for how the attributes should behave in a similar gas hydrate setting. Furthermore, access to the angle stacks allows for analyzing attenuation variations (by attribute response) across the different angles and provides a unique opportunity to test the spectral attributes in a new way. Lastly, incorporating seismic attributes into unsupervised machine learning allows for additional visualization and enhancement of subtle attenuation-related responses and variations in the data, and provides the researcher the opportunity to correlate the results with the known geology and hydrate system.

3.1 Data Conditioning

The methodology for this study, as outlined in Figure 2, begins with the seismic amplitude volume. Care must be taken at the beginning to determine whether or not the seismic amplitude has been previously spectrally-balanced during the processing stage. It is expected that spectrally balancing the data, while improving the vertical resolution and preconditioning the data for subsequent spectral analysis, would undermine the accuracy of specific spectral shape attributes which measure the asymmetry of the seismic amplitude spectrum. While spectrally-

balanced data may be used for other attribute calculations, for consistency within this study, only non-balanced data was used for all the attribute calculations.

3.1.1 Seismic Spectra and Bandwidth of the APB13 Seismic Survey

Bandwidth is the useable range of frequencies within a dataset, often defined within a low-cut/high-cut or low-pass/high-pass filter (Hart, 2011). While bandwidth is not the main focus of this research project, it is of interest due to its relationship to frequency and the seismic amplitude spectrum. As it has been shown that the frequency and therefore seismic spectrum of the dataset are impacted by attenuation effects, it follows that there will be an impact in the bandwidth of the data as well. Bandwidth may be most closely related to the kurtosis attribute, which is described below, since kurtosis is based on outliers in the data, which may be observable in the changing bandwidth.

Additionally, in order to compare the spectral attribute response to the fluctuations in the spectra and bandwidths of the data, the amplitude spectrum was computed across several intervals of interest. Specifically, zones that corresponded to strong positive and strong negative skewness and kurtosis were of interests, respectively. The cutoff values across which the seismic amplitude spectra were calculated are shown in Table 2. These correspond to negative skewness, positive skewness, negative kurtosis, and positive kurtosis, respectively. Results are shown in Appendix C.

3.1.2 Cropping Data to Area of Interest and Computing Bounding Horizons

Each of the following seismic attributes were computed from a cropped interval of the 2D seismic data. Cropping helped constrain the area of interest and may reduce computational power when running complex machine learning on large datasets. The data boundary was specified at 3.3-4.3 seconds TWT and between 3500-5500 CDP across APB-13 seismic line 38 (see Figure 6

for cropped area). There are two approaches that can be taken when determining an interval over which to implement machine learning. The first approach is to crop the data to a smaller, more manageable size such that outlier data is generally excluded. The second is to pick a top and base horizon—in this case the ocean bottom and BSR, where it exists—and compute the machine learning between those two horizons. The horizons were picked on each respective full, far, and near angle stack on the ocean bottom and BSR and formatted at gridded EarthVision files. The second method using distinct top and base horizons is likely to give more robust details about the specific zone of interest (the gas hydrate stability zone), but both approaches are shown here. For the cropped example, the seismic amplitude data volume was cropped to 3.3-4.3 seconds and 3500-5500 CDP across APB-13 seismic line 38.

Furthermore, once data was appropriately cropped, the seismic line was subdivided into five zones with distinct seismic characteristics and attribute variations. The zones correspond to the following approximate depth or seismic feature cutoffs throughout the GHSZ: Ocean bottom (Zone 1), immediately below ocean bottom reflector to 3.53 seconds (Zone 2), 3.54 – 3.79 seconds (Zone 3), 3.8 – BSR (Zone 4), BSR (Zone 5).

3.2 Spectral Decomposition

After picking the major stratigraphic reflectors of interest and/or cropping the seismic amplitude volume, a spectral decomposition method based on the continuous wavelet transform is used to decompose the seismic into its frequency components. Grossmann and Morelet (1984) first define the CWT as a cross-correlation between the seismic trace and a dilated version of a basic wavelet, which allows the CWT results to include information about the time/depth and frequency of the seismic trace. The continuous wavelet transform has been used for many applications in geophysics from improving seismic resolution for reservoir geometry studies

(Matos et al., 2012) to application of spectral components (computed from CWT) for resolving subtle stratigraphic features in carbonate and clastic reservoirs (Davogustto et al., 2013) and improving vertical imaging within 3D seismic datasets (Peyton et al, 1998). In this research, the spectral decomposition is necessary to decompose the seismic into its spectral components; this allows the algorithm to compute the statistics (ie, skewness and kurtosis), on the spectrum across each sample (rather than by trace, line, or volume). Therefore, the statistical response is calculated from the spectrum at each individual point or sample in the data, rather than across the entire seismic line or cropped volume.

3.3 Seismic Attributes

As the focus of the study is to identify the attenuation in the seismic due to gas hydrate presence, seismic attributes that are related to frequency were chosen as they best detect attenuation of the seismic waveform. Among these, spectral skewness and kurtosis attributes represent the frequency spectrum of the seismic amplitude volume computed using a continuous wavelet transform. These attributes are implemented through a spectral attributes utility which is a spectral decomposition method based on the continuous wavelet transform, as discussed previously.
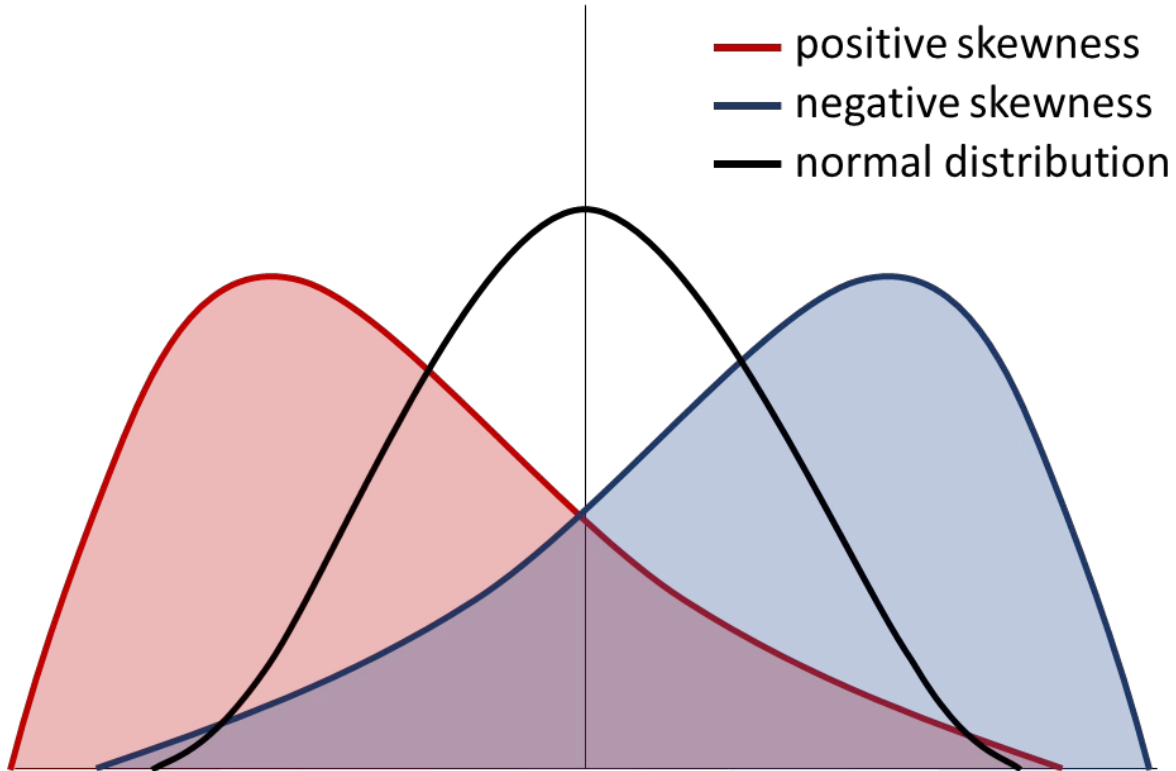
Fig. 3 Skewness variations with positive (red line and shading), negative (blue line and shading), and normal or zero skewness (black line and no shading)

3.3.1 Spectral Skewness Attribute

Skewness is a statistical measure that defines how much a dataset deviates from the mean of the data (Figure 3). It is the 3rd moment of the standard score of the variable y (seen in the equation below, Equation 1). Data that is skewed toward the left has positive skewness, data that is skewed toward the right has negative skewness, and data that is perfectly symmetric around the mean has 0 skewness. A calculation for skewness comes from Sharma (2020) and is simply the difference between the mean and the mode (or 3 times the median minus 2 times the mean) of the dataset divided by the standard deviation. Skewness has been used for seismic analysis before as seen by Li et al. (2016) to characterize attenuation within conventional and unconventional hydrocarbon reservoirs, and is given by the equation

$$Skewness = \frac{\sum_i^n (Y_i - \bar{Y})^3}{(n-1)\sigma^3} \qquad \text{Equation 1}$$

where σ is the standard deviation of the dataset and Y is the random variable to be defined, or in this case, amplitude. In this study, skewness is applied as an attribute to measure attenuation seen in the frequency spectrum of the seismic data. Since it has been shown that hydrates often attenuate high frequencies over low frequencies (Raikes and White, 1984), attenuation of high frequencies is expected to give a positive skewness response as the data becomes skewed toward the low-frequency end of the spectrum (Figure 3, see positive skewness example). However, one consideration is that these metrics are in comparison to a normal or Gaussian distribution of data, and it is important to note that seismic data is inherently non-Gaussian. A typical seismic spectrum is expected to be overall positively skewed due to seismic data containing generally a higher percentage of low frequency to high frequency as the earth is a natural attenuator.
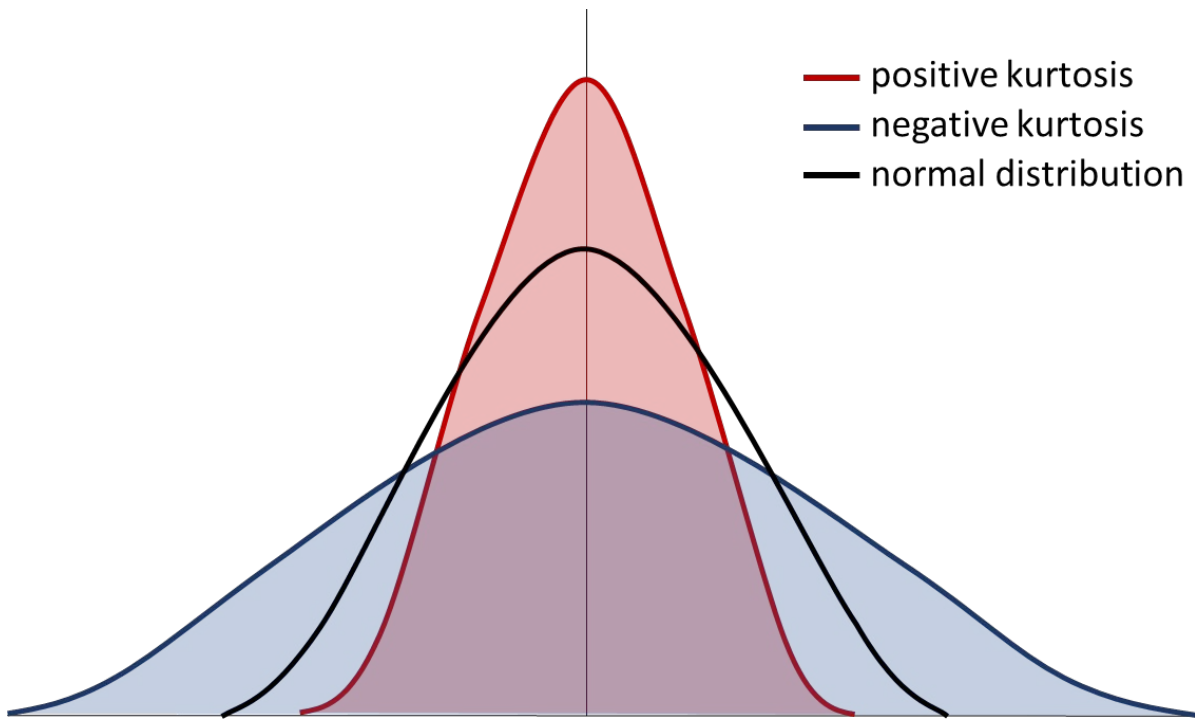
Fig. 4 Kurtosis variations with positive (red line), negative (blue line), and normal or 0 kurtosis

3.3.2 Spectral Kurtosis Attribute

Kurtosis is a statistical measure that defines the "tailedness" of, or the distance of the tails from the mean in a normal distribution (Figure 4) of a dataset. It is the 4th moment of the standard score of the variable y (as seen in Equation 2 below). Although kurtosis is always positive and ranges from 1 to infinity, "excess positive" refers to data that is heavily-tailed and has a large amount of outliers, also referred to as *leptokurtic*. "Excess negative" describes data that is light-tailed and has very few outliers, sometimes referred to as *platykurtic*. A normal distribution of data will have a kurtosis value of 3, so normalizing the data about 3 gives excess negative kurtosis at a value of -2 and while excess positive is a value of +2 (Sharma, 2020). Kurtosis was also applied by Li et al. (2016) and is given by the equation

$$Kurtosis = \frac{\sum_i^n (Y_i - \bar{Y})^4}{(\sum_i^n (Y_i - Y)^2)^2} \qquad \text{Equation 2}$$

A lower peak frequency, as demonstrated by Li et al (2015) is expected to present as positive kurtosis. Positive kurtosis may also be thought of in relationship to bandwidth; a narrower bandwidth from attenuated frequencies should therefore exhibit positive kurtosis. Kurtosis is often casually described in terms of the "peaked-ness" of a dataset, with negative kurtosis being low-peaked and positive kurtosis being high-peaked. While these descriptions may be useful for understanding the shape of a spectrum in some circumstances, it is more accurate to describe kurtosis in relationship to the outliers, ie, tails.

3.3.3 RMS Amplitude Attribute

RMS amplitude is a commonly applied seismic attribute that is computed such that the root-mean-square (RMS) of the data, d(t), is given by:

$$d_{RMS}(j\Delta t) \equiv \sigma(j\Delta t) = \left(\frac{1}{2K+1} \sum_{K=K}^{+K} \{d[(j+k)\Delta t)]\}^2 \right)^{1/2} \quad \text{Equation 3}$$

and calculated over a user-defined analysis window (Chopra and Marfurt, 2007) with range equal

to -T =KΔt to +T=+KΔt. RMS amplitude is applied to this study as it is a good indicator of

changes in amplitude and can be contrasted with the frequency attributes to determine whether

attenuation response is tied to amplitude or frequency variations across the GHSZ and how those

relate to the geology and stratigraphic nature within the Pegasus Basin.

3.3.4 Envelope Attribute

Envelope, also called the instantaneous amplitude attribute or reflection strength, is a

complex trace attribute that was described by Taner et al. (1979) as related to a reflection event

along the seismic trace and is calculated from the seismic trace (t) and the Hilbert transform

[u^H(t)] such that

$$e(t) = \{[u(t)]^2 + [u^H(t)]^2\}^{1/2} \qquad \text{Equation 4}$$

Envelope is useful as a thin-bed tuning indicator and also can be used to represent changes in

lithology, porosity, and hydrocarbon accumulation due to its relationship to acoustic impedance

contrast (Chopra and Marfurt, 2007). For this study, envelope is useful for enhancing the BSR

related to gas hydrate accumulation and for determining non-frequency-related responses in a

hydrate system. Additionally, envelope is one of the parameters used to calculate the sweetness

attribute, which is described in Section 3.3.6.

3.3.5 Instantaneous Frequency Attribute

The instantaneous frequency attribute is calculated as the derivative of the instantaneous

phase attribute by the equation (Eq. 3)

$$f(t) = 2\pi \frac{d\varphi(t)}{dt} \qquad \text{Equation 5}$$

where *φ(t)* is the instantaneous phase and *f(t)* is the seismic trace. Instantaneous frequency is

commonly used for thin-bed tuning and, since it is a frequency-derived attribute, can also give

clues about attenuation (Chopra and Marfurt, 2007). Instantaneous attributes such as instantaneous frequency and envelope (described below) have been applied in the Pegasus Basin by other authors and were found to be useful for highlighting attenuation response (Clairmont et al., 2021) and for detecting weak BSRs (Chenin and Bedle, 2020). In this study, instantaneous frequency is used in addition to skewness and kurtosis to give feedback about the attenuation response and how hydrates impact the frequency spectra of the seismic data.

3.3.6 Sweetness Attribute

Sweetness is another commonly-used attribute for hydrocarbon settings and enhancing low frequency, high amplitude zones that may be representative of hydrocarbon-filled sands. Sweetness is calculated from the instantaneous frequency and envelope attribute, so it gives a unique combination of both frequency and amplitude responses:

$$s(t) = \frac{e_{resp}(t)}{[f_{resp}(t)]^{1/2}} \quad \text{Equation 6}$$

where e is the envelope of the seismic trace and f is the frequency of the seismic trace. For this study, sweetness is useful for channel detection, highlighting clean sand layers (Hart, 2008), and subtle changes in amplitude and frequency, the latter of which is especially useful for measuring attenuation.

3.4 Unsupervised Machine Learning—SOMs Methodology

Machine learning is a type of data science that uses an algorithm or set of algorithms to learn from and train on a dataset, with the end goal being a model able to make predictions relative to the research question the machine learning is applied to answer (Allen, 2020). While machine learning (ML) has gained popularity over the recent decades, with many people viewing it as the all-encompassing solution to any problem involving data, the trite saying often associated with machine learning is true: "Garbage in, garbage out." Therefore, not only is it

important to have quality input data into machine learning, but it is also critical to have at least a cursory knowledge about the type of machine learning being utilized. Herein is presented an overview of the ML method, self-organizing maps (SOMs), chosen for this project.

3.4.1 Self-organizing Maps Theory and Previous Applications

At its basic level, SOMs are a pattern-recognition method of machine learning based on theory that allows the algorithm to take input data (in this case, seismic attributes) and group that data into "feature maps" that can be tied to some meaningful geological or geophysical relationship (Kohonen, 1982, 1990). More technically, Teuvo Kohonen, the researcher that first developed self-organizing maps described them as "a nonlinear, ordered, smooth mapping of high-dimensional input data manifolds onto the elements of a regular, low-dimensional array," (2001). In other words, the mapping process takes N-dimensions of data (set by the number of input attributes), determines how those J-vectors comprising the attributes are related to each other within the latent space, and projects the output vectors into a lower-dimensional space or "manifold" in which space the algorithm can form clusters (Zhao et al., 2015, 2018), also called neurons, "prototype vectors," or SOM units (AASPI som3d program documentation, 2020). These neurons or vectors are then colored by a 2D color bar that has the number of classes determined during the input parameters (discussed below) and the SOM implementation. For this research, the goal is to use SOMs to help show features beyond a single attribute's ability to classify or visualize the seismic data, therefore increasing our understanding of the attribute response in a gas hydrate setting.

The self-organizing maps application is a straightforward and relatively simple way to implement a machine learning method as it does not require a significant number of inputs beyond training iteration and decimation, and while some users may feel this method has some

"black box" characteristics that are typical of many unsupervised machine learning techniques, it is an effective and proven method of classifying beyond attribute selection and visualization. SOMs have been applied in other seismic studies to interpret deepwater seismic facies and architectural elements (La Marca and Bedle, 2021; La Marca, et al., 2019) and characterize turbidites in seismic data (Zhao et al., 2016), to evaluate reservoir lithology and rock type changes (Hussein et al., 2021), enhance weak or discontinuous BSRs (Chenin and Bedle, 2020), and combining PCA and SOMs to discriminate BSRs from surrounding lithology (Lubo-Robles et al., 2023). It's important to note that when apply SOMs to a particular research problem, the input attributes should be appropriate to the specific research goal; that is, geometric attributes should be used to answer questions about the structure or stratigraphy of a seismic dataset (Zhao et al., 2018), or spectral shape attributes to measure attenuation of the amplitude spectrum, and so forth.

3.4.2 Self-organizing Maps Implementation

The primary input for the SOM implementation is, of course, the seismic attributes. In total, the six attributes (spectral skewness, spectral kurtosis, instantaneous frequency, envelope, sweetness, and RMS amplitude) described above were input into the algorithm, and each attribute was normalized using a z-score algorithm. Besides the input attributes, however, there are other primary parameters that need to be input by the user that will determine the output feature maps. The maximum number of classes for each SOM case was set to 256 as this is the maximum number many software can visualize, although the algorithm determines the final (if smaller than 256) number of classes (AASPI som3d documentation, 2020). The number of data training iterations was set to 30; the initial approach utilized fewer than 30 iterations but found that the output left certain gaps or "non-classified" data, so 30 was determined to be optimal. The

CDP decimation in training, line decimation in training, and vertical sample decimation in training were all set to 2 as this value was considered a robust decimation rate for the dataset.

The first approach (Case 1) to implementing the SOM algorithm was calculated across a user-defined constant time window of 3.3-3.4 seconds, as described in Section 3.1.2. This interval corresponds to slightly above the ocean bottom and approximately 0.2 seconds below the BSR as expressed in the selected area of interest. The second approach (Case 2) to implementing the SOM algorithm was calculated across a window defined by a top and base horizon. These two bounding horizons were the ocean bottom horizon (top) and BSR horizon (bottom). The horizons were mapped and gridded from the 2D seismic lines (for each of the full, far, and near angle stacks) in a separate seismic interpretation software. While the vertical window was different for the two cases, the lateral extent was the same for both cases.

Finally, the output from the implementation are two SOM projection axes (Projection Axes 1 and Projection Axes 2). The final SOM output or facies map is created by cross-plotting the two projection axes against each other. The SOM facies are colored based on a 2D color map, which is generated from the number of classes determined during input and by the algorithm and co-rendered with the histogram of clusters that occur in the data.

4. Results

The results for the spectral shape and supplemental attributes, and unsupervised machine learning are presented below, with careful descriptions to aid understanding of how attribute response is related to attribute theory.

4.1 Seismic amplitude volume description

In the APB13 survey across the Pegasus Basin, the ocean bottom occurs as a strong peak reflector that is easily identifiable across the Opouawe Bank of the North Island, Hikarangi

Trough, and Hikarangi Channel. The BSR roughly mimics the ocean bottom reflector, however with opposite reflectivity/polarity. In the seismic data, the BSR appears from 2-5 seconds TWT ranging from the northwest along the Opouawe Bank to the southeast across the Hikurangi Channel and corresponds to a continuous medium to high amplitude trough (Figure 5 and 6). There are discontinuous BSRs, also observed by Chenin and Bedle (2020) and Clairmont et al. (2021) that extend throughout the central part of the Pegasus Basin (between 3000-4500 CDP on ABP-13 line 38) and more continuous BSRs that extend upward along the Opouawe Bank to the northwest and from CDP 4500 to the edge of the seismic survey in the Hikurangi Channel (Figures 5 and 6). The BSR is most easily identified where it crosscuts structure and stratigraphy along the flank of the Opouawe Bank and the southeast edge of the survey. These areas present high amplitude BSRs and are associated with microbial methane accumulations (Kroeger et al., 2015) and high Q^{-1} (inverse quality factor or attenuation) values below, and in some cases, above, the BSR (Clairmont and Bedle, 2021). While analyzing the BSR itself and the area below the base of the GHSZ is outside the scope of this project, the seismic expression below the high amplitude BSRs shown in Figure 6 and 7 contain several "bright spots" that are likely due to trapped free gas beneath the GHSZ, while low amplitudes (or possible amplitude blanking) below the low amplitude, weak, or discontinuous BSR could be due to a low-frequency shadow zone or more simply, a low impedance contrast between relatively homogeneous mixed siliciclastics that are present throughout the basin. Where the BSR itself is absent or weak, there could be less free gas in the system being trapped by the hydrates, therefore creating the weak seismic reflector, but from a visualization standpoint, throughout the central section of the basin (Figure 6) the BSR is more parallel to stratigraphy, which may be causing lower contrast compared to areas where the BSR cross-cut stratigraphy. Since it is already known that hydrates

do occur in this area of the Pegasus Basin, now the aim of the project is to build on the previous work to measure the attenuation *within* the GHSZ instead of below the BSR.

Using the BSR as an indicator of the base of the GHSZ, attenuation is expected to occur anywhere within the GHSZ where hydrate accumulation occurs. To limit the area of focus to exclusively the hydrates within the GHSZ, a smaller cropped interval (roughly between 3.3 to 4.3 seconds and between CDP [common depth point] numbers 3500 to 5500) was analyzed (Figures 6b and 7). This area contains high amplitude BSRs in addition to low amplitude BSRs, providing an opportunity to study attenuation in the presence *and* absence of BSRs. This might give clues as to the hydrate presence, especially where BSRs are absent, and establish statistical attributes' ability to delineate subtle changes within the GHSZ. Within this cropped interval of data, the BSR exhibits as a high amplitude seismic reflector, sub-parallel to the ocean bottom toward the western edge of the Hikarangi Channel, and transitions to low amplitude toward the central section of the basin (Hikarangi Trough). The seismic reflectors throughout the seismic line (Figures 6b and 7 and corresponding attribute figures) are horizontal to sub-horizontal, parallel, and fairly continuous; however, between 3.53-3.8 seconds (TWT), there is a series of higher amplitude, thin, sub-parallel reflectors (see Figures 6b and 7) that exhibit amplitude increase with offset and that may represent sediment waves described by Lewis and Pantin (2002).
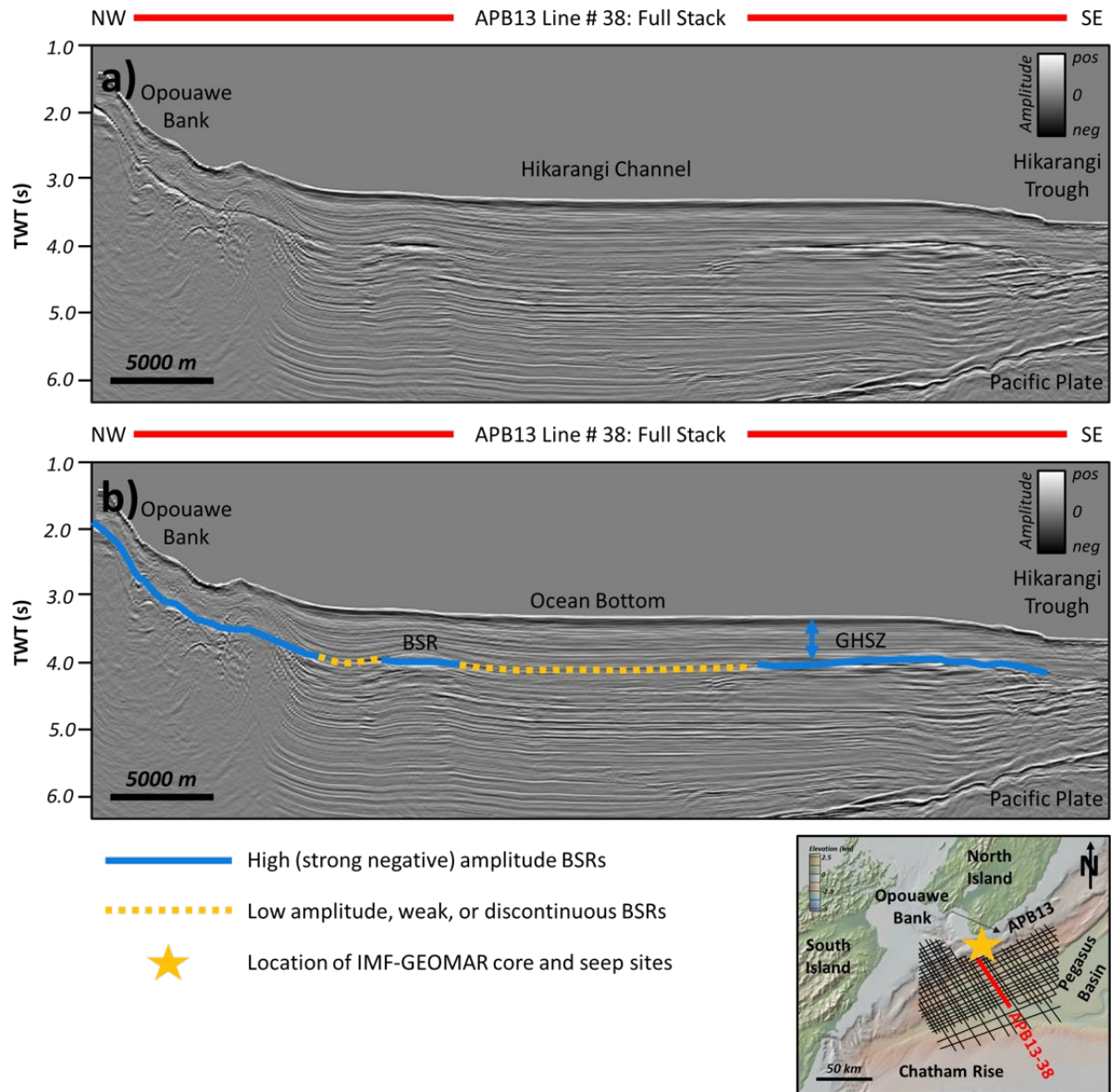
Fig. 5 a full stack seismic line across the Pegasus basin and **b** interpreted areas showing BSR extent throughout the seismic line, with the GHSZ, and ocean bottom
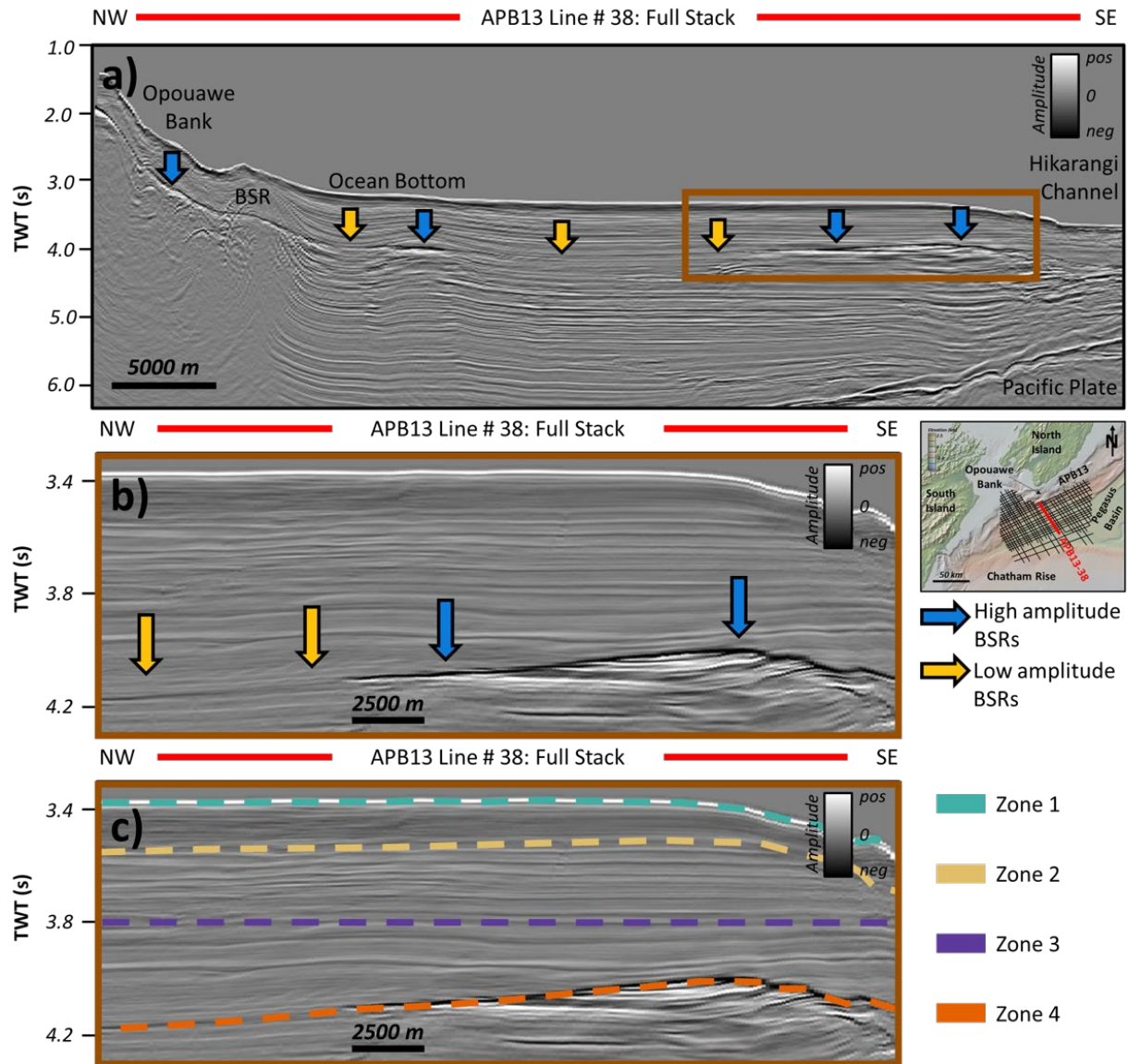
Fig. 6 a full stack seismic line across the Pegasus basin, **b** interpreted areas showing BSR extent (both high and low amplitude) throughout the seismic line, and **c** zones 1 - 4; seafloor bathymetry map from GeoMapApp
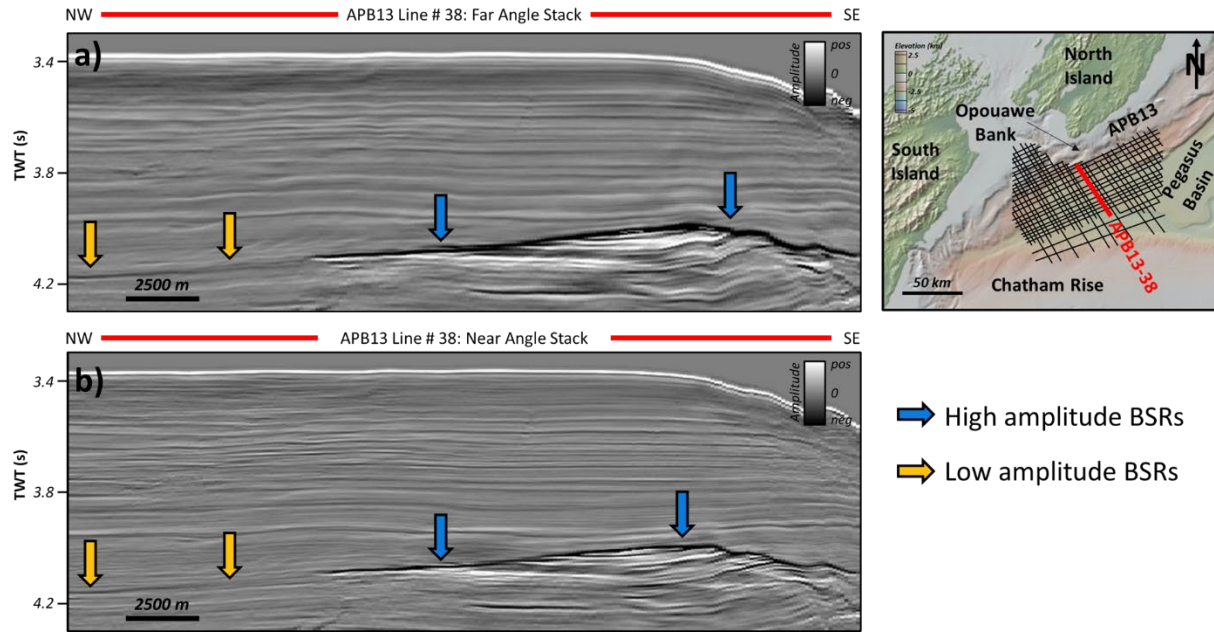
Fig. 7 a far angle stack seismic line with high and low amplitude BSRs, and **b** near angle stack with high and low amplitude BSRs; the seismic amplitudes are plotted on the same scale for each of the full, far, and near angle stacks

4.2 Attribute volumes

Seismic attribute analysis was performed on each of the statistical attributes and on the five supplemental frequency-, trace-, and amplitude-related attributes prior to implementing the machine learning to assess whether the attributes could contribute to enhancing variations in the GHSZ due to attenuation from hydrate accumulation. While the main focus is the statistical attributes, as they are novel and untested in this approach and the four supplemental attributes are already proven to be applicable in a hydrocarbon setting, all the attributes were carefully inspected from the ocean bottom to the base of the gas hydrate stability zone to determine each individual attribute's contribution to understanding the hydrate system. Furthermore, the combination of frequency- and amplitude-related attributes provides a wholistic suite of attributes for the SOM implementation in the machine learning phase. The attribute response for each attribute in the corresponding zone is reported in Table 2.

Volume	Stack	Zone 1, OB to 3.53 sec TWT	Zone 2, 3.53 - 3.8 sec TWT	Zone 3, 3.8 sec TWT - BSR	Zone 4, BSR
Seismic Amplitude	Full	OB: high amplitude, continuous peak. Below, fairly continuous, horizontal to sub-horizontal reflectors	Some slightly chaotic seismic reflectors; amplitude relatively continuous throughout	Fairly continuous, horizontal to sub-horizontal reflectors; thicker beds than in Zone 2	High amplitude trough to low amplitude trough
	Far	OB: high amplitude, continuous peak. Below, fairly continuous, horizontal to sub-horizontal reflectors	Some slightly chaotic seismic reflectors; amplitude lower than full stack	Fairly continuous, horizontal to sub-horizontal reflectors; thicker beds than in Zone 2, lower amplitude than full and near stack	High amplitude trough to low amplitude trough; higher amplitude than full and far stacks
	Near	OB: high amplitude, continuous peak. Below, fairly continuous, horizontal to sub-horizontal reflectors	Some slightly chaotic seismic reflectors; amplitude higher than full stack	Fairly continuous, horizontal to sub-horizontal reflectors; thicker beds than in Zone 2; higher amplitude than full and far stack	High amplitude trough to low amplitude trough; lower amplitude than full stack
Skewness	Full	OB: strong positive. Below, mixed, predominantly medium positive	Mixed low positive to medium negative in the chaotic reflector interval	Predominately strong to medium positive; strong positive dominates over the high-amplitude BSR	Low negative with patches of 0 to low positive
	Far	OB: strong positive. Below, mixed, predominately medium positive	Predominately medium positive; low negative mainly in the sediment wave interval, but skew-AVO is reduced compared to full	Strong positive, especially above the high-amplitude BSR; higher amplitude of skewness than the full stack	Varies between low negative to 0 with some patches of low positive
	Near	OB: strong positive. Below, mixed, medium positive to negative	Predominately medium negative with patches of medium positive; highest negative skew-AVO in sediment waves	Medium to low positive, with patches of medium negative above the low-amplitude BSR	Low negative with patches of 0 to low positive; more negative than in full
Kurtosis	Full	OB: strong negative. Below, mixed, predominately medium negative	Predominately medium negative throughout	Strong positive, especially above the high-amplitude BSR, with patches of low negative throughout	Medium negative throughout
	Far	OB: strong negative. Below, mixed, medium/high positive to medium negative	Mixed medium negative to medium/high patches throughout	Strong positive, especially above the strong BSR; higher amplitude of kurtosis than the full	Medium negative throughout
	Near	OB: strong negative. Below, predominately strong negative	Predominately medium to strong negative throughout	Strong negative, with small patches of medium to strong positive	Medium to strong negative throughout, especially over the weak BSR
RMS Amplitude	Full	OB: 700-900. Below, low	Low	Low	Medium to high
Instantaneous Frequency	Full	OB: 600. Below, low to medium	Low to medium, predominately medium in the sediment wave reflectors	Medium to low	Medium, mixed medium to low over the low-amplitude BSR
Envelope	Full	OB: 900-1800. Below, low	Low	Low	Medium to high; low over the low-amplitude BSR
Sweetness	Full	OB: strong positive. Below, medium	Low to medium	Medium to low	Medium to high, medium to low over the low-amplitude BSR

Table 2. Result summary table for seismic amplitude and the skewness, kurtosis, RMS amplitude, instantaneous frequency, envelope, and sweetness attributes. Results are per zone 1 – 5 with corresponding start/stop time and CDP cutoff values. Skewness and kurtosis results include attribute variations observed in each angle stack

Fig. 8 a full stack seismic line with high and low amplitude BSRs, **b** skewness attribute calculated from the full stack seismic line, **c** skewness attribute calculated form the far angle stack seismic line, **d** skewness attribute calculated from the near angle stack seismic line, **e** amplitude co-rendered with skewness attribute, and **f** zones 1 - 4 on the full stack seismic line

4.2.1 Spectral Skewness Attribute

Skewness is inherently a dual-polarity (negative to positive, with perfect symmetry or no skewness at 0) statistical measure, and the histogram of the attribute was useful for determining the most appropriate end-point values for plotting the attribute results. The end-point values roughly ranged from -1.5 to 1.5 in the full stack data, and for consistency, those values were used when plotting the far and near angle stacks as well. With respect to the variations across the angle stacks described below: while the skewness variation is not strictly an AVO-type response, since it's not the amplitude of the seismic that is being analyzed, the amplitude *of the skewness* response is varying with angle, therefore, the term "skew-AVO" is used to describe the effect.

Throughout the GHSZ in Zone 1, skewness ranges from slightly positive at the ocean bottom to 0 across the (trough or ocean bottom sidelobe) reflector immediately below, and then varies from 0 to positive between approximately 3.42 to 3.6 seconds (TWT, see Figure 8a and b). At approximately 3.6 seconds in Zone 2 there is a negative skewness response that is strongest around the central to northwestern section of the basin, however this negative response varies in discontinuous patches across the entire Zone 2. The negative skewness band is seen most clearly in the full stack and near angle stack attribute lines, while it is less continuous and plots closer to 0 skewness in the far angle stack. The negative skewness described in Zone 2 roughly corresponds to the thin-bedded, sub-parallel reflectors described in the seismic amplitude line Zone 2.

Below the base of the negative skewness response at the start of Zone 3 (3.8 seconds), there is another interval of positive to strongly (around 1.5) positive skewness that extends to approximately 4.0 seconds, immediately above the high amplitude BSR (Figure 8a). The strongest skewness response is observed in the far angle stack, although it is comparable to the

full stack line's skewness response, with noticeably weaker positive skewness in the near angle stack. The near angle stack also contains larger patches of slightly negative skewness directly above the *weak* BSR toward the northwest end of the seismic line. These negative skewness patches are only weakly observed in the full and far angle stack lines. The skewness response at the high amplitude BSR at the base of the GHSZ in Zone 4 is observed as stronger negative skewness in the near angle stack, slightly less negative in the full angle stack, and weakly negative to 0 skewness in the far angle stack. Along the low amplitude, discontinuous BSR at the northwest end of the seismic line, there is a weakly negative skewness response that is more apparent in the near angle stack, and approximately 0 to weakly negative skewness in the full and far angle stacks. Although the area below the GHSZ is outside the scope of this project, the skewness response is generally 0 to positive, with slightly more negative skewness observed in the near angle stack. Due to the contrast between the negative skewness response at the BSR and the positive skewness directly above and below the BSR, the GHSZ is easily discernible from the underlying, hydrate-free interval.

To summarize the skewness response throughout the GHSZ, there are two zones of strong positive skewness between roughly 3.4-3.59 (Zone 1 into Zone 2) seconds and from 3.8 to the base of the GHSZ (Zone 3). From 3.6-3.8 seconds (Zone 2), there is a 0 to negative skewness response that is most evident in the near angle stack. Finally, at the base of the GHSZ/BSR (Zone 4), there is a weak to medium negative skewness response that is strongest in the near angle stack.
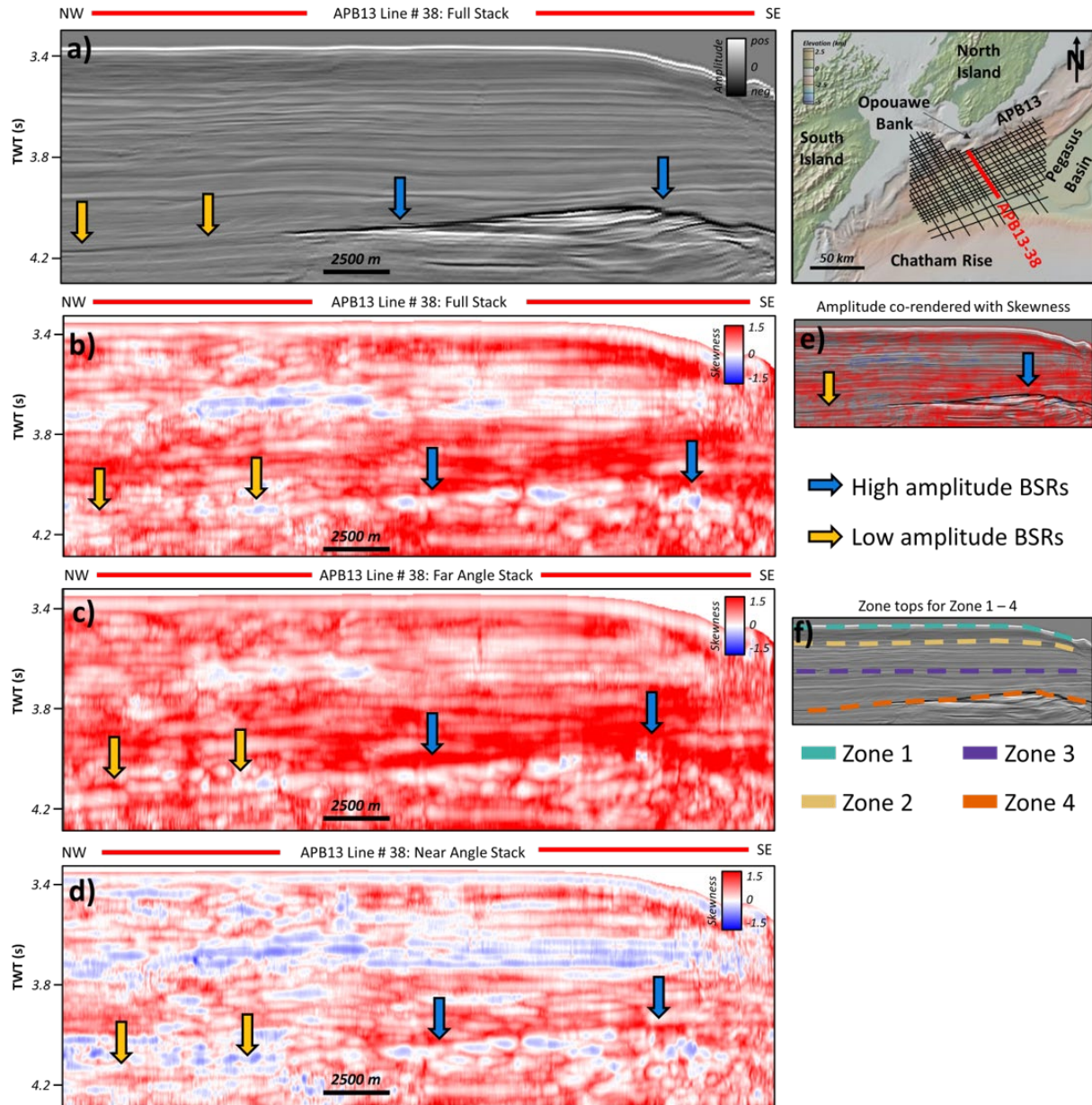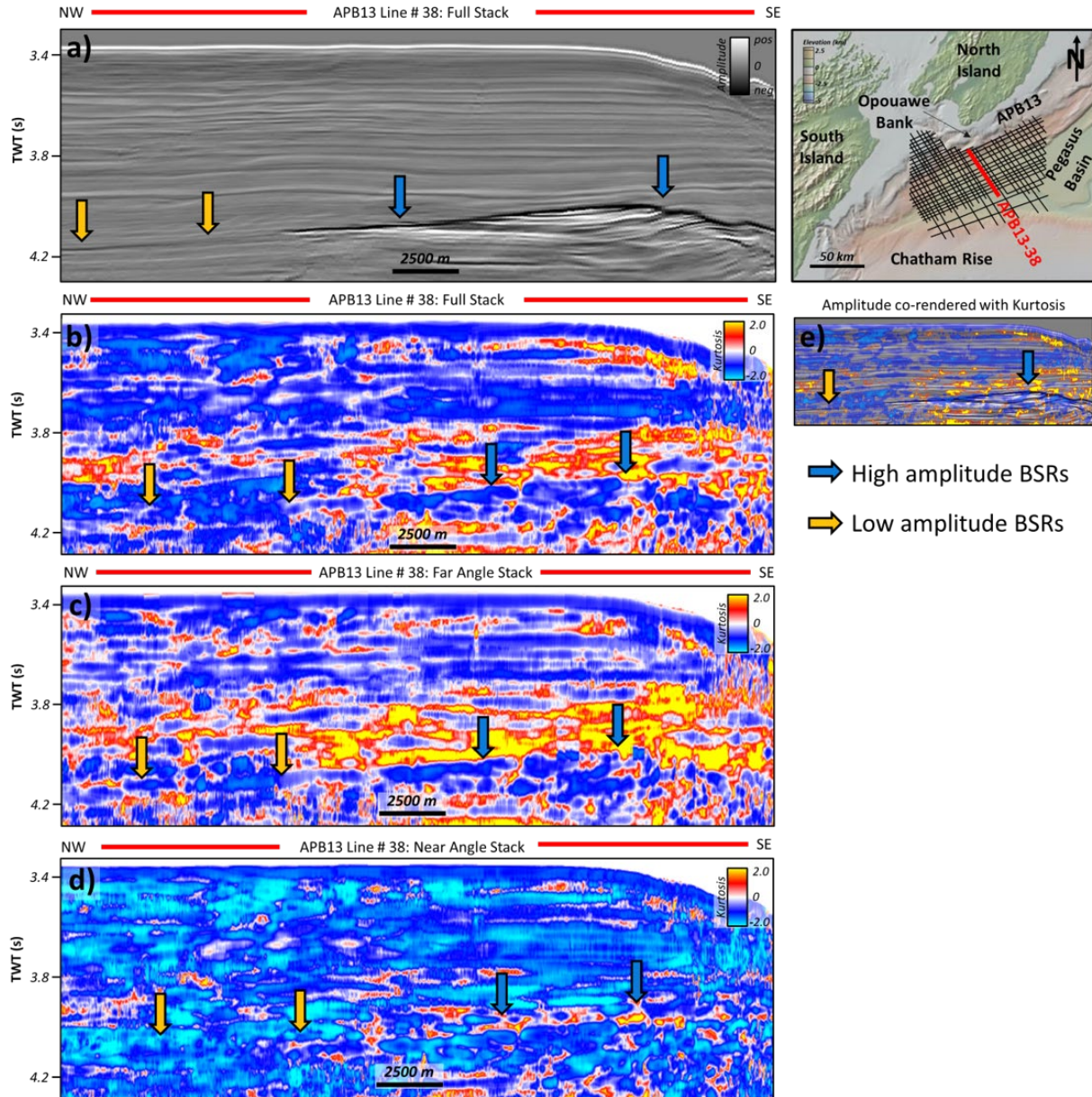
Fig. 9 a full stack seismic line with high and low amplitude BSRs, **b** kurtosis attribute calculated from the full stack seismic line, **c** kurtosis attribute calculated form the far angle stack seismic line, **d** kurtosis attribute calculated from the near angle stack seismic line, **e** amplitude co-rendered with kurtosis attribute, and **f** zones 1 - 4 on the full stack seismic line

4.2.2 Spectral Kurtosis Attribute

Kurtosis is inherently an all-positive statistical measure; however, "excess" is used to refer to values that define the outlier data within the metric. It is possible to select "all positive values" when plotting the kurtosis attribute, and then set the data end-points using the histogram

or through simple trial and error. For this dataset, -2.0 to 2.0 was determined to best capture the variability within the kurtosis results, and these values were used for each of the angle stacks. As mentioned in the previous skewness results, there is a similar kurtosis variation that is observed in the different angles. Again, while this is not strictly a classical AVO-type response, the variations are in the amplitude *of the kurtosis response* and are referred to as "kurt-AVO" in the later discussion section.

Within the GHSZ Zone 1, the first kurtosis response is a medium negative at the ocean bottom reflector. Immediate below the ocean bottom reflector is a thin interval of mixed strong positive to weak positive from the full angle stack to the near angle stack, respectively. This thin, high kurtosis response appears in the southeastern half of the seismic line into the slope of the Hikarangi Channel and is strongest in the full angle stack. Excluding the thin positive kurtosis response previously described, the rest of Zone 1 is general characterized by negative kurtosis with patches of 0 to medium positive kurtosis. In Zone 2, there is an interval of primarily negative kurtosis extending to the base of Zone 2. The negative kurtosis response in Zone 2 is strongest negative, approximately -2, in the near angle stack, then medium negative kurtosis in the full stack, and weakest negative with more thin patches of 0 to low positive kurtosis in the far angle stack. In the far angle stack, the kurtosis response follows a somewhat vertically stratified pattern which diminishes in the full and near angle stacks.

In Zone 3, below 3.8 seconds to the base of the GHSZ, the full and far angle stack show strong positive, around 2, kurtosis response directly above the high amplitude BSR. The far angle stack contains a broader and thicker extent of the positive kurtosis response compared to the full angle stack. The near angle stack only shows a very thin interval of positive kurtosis directly above the high amplitude BSR, with the majority of Zone 3 being negative to strong

negative, around -2, kurtosis. Above the low amplitude, discontinuous BSR, there is an interval of negative kurtosis that is more easily observed in the near and full stacks, and is weaker, discontinuous, and variable in the far angle stack. As previously mentioned for the skewness attribute, although the interval below the GHSZ is outside the scope of this project, the kurtosis response is predominately medium to strong negative, with patches of positive seen in all three angle stacks.

To summarize the kurtosis response, kurtosis proved to be more variable throughout the GHSZ than the skewness response, at least with respect to variations observed across the angle stacks. In the full and far stacks, the kurtosis response showed negative kurtosis at the ocean bottom reflector and between 3.6-3.8 seconds (Zone 2), with a variable positive response above 3.6 seconds and directly below the ocean bottom (Zone 1). Between 3.8 and the base of the GHSZ/BSR (Zone 3), there was a zone of strong positive kurtosis in the full and far stacks, while the near stack showed mostly negative response. Similar to skewness, kurtosis appears to be roughly vertically "stratified," that is, it is closely laterally continuous (negative or positive) and these zones are separated by thin 0-value or weak positive/negative kurtosis.
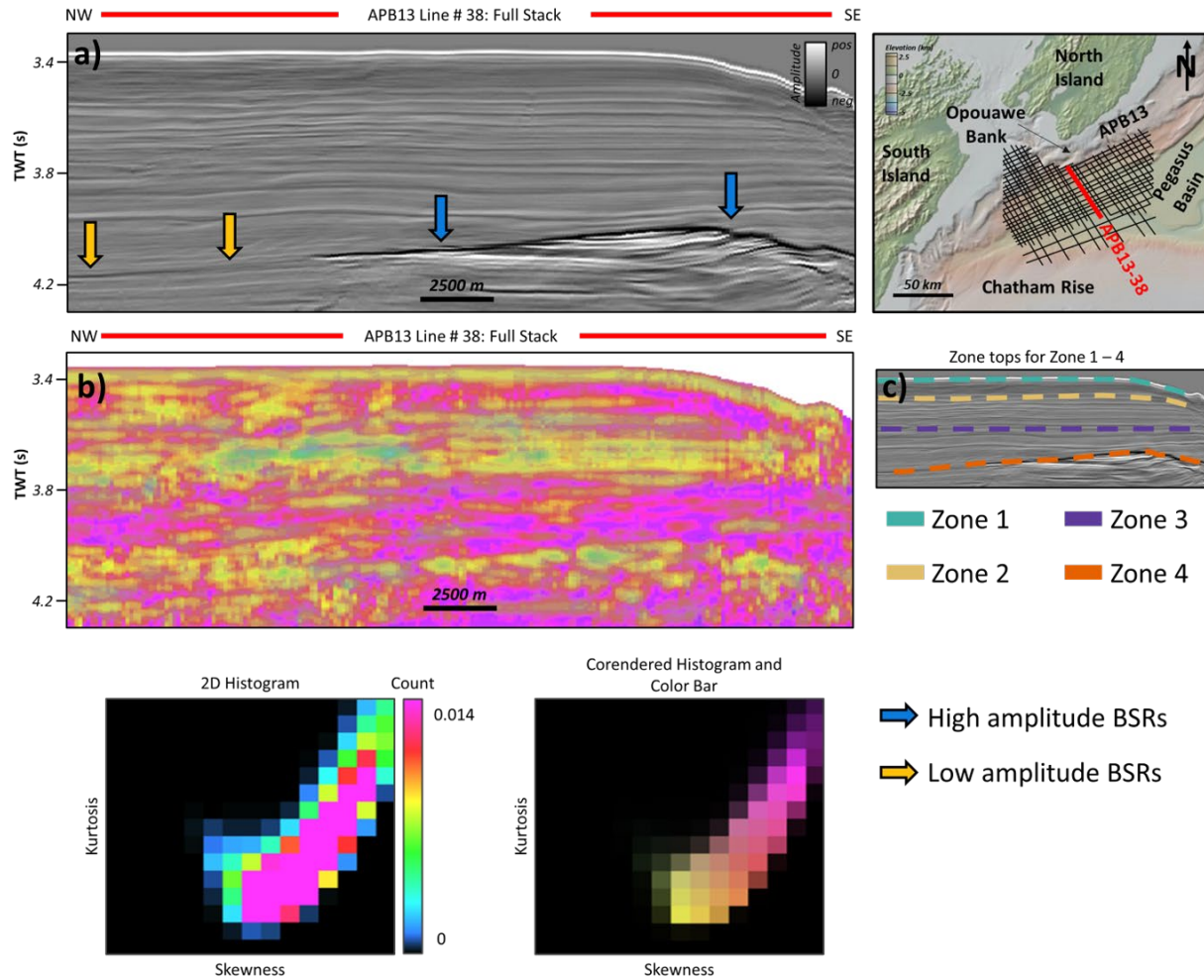
Fig. 10 a full angle stack seismic line with high and low amplitude BSRs, **b** crossplot of kurtosis verses skewness calculated on the full stack seismic line, and **c** Zones 1 – 4 on the full stack seismic line. The histograms and 2D color map are used to determine the colors represented in **Fig 10b**

Skewness and Kurtosis Crossplot

Crossplotting skewness verses kurtosis shows that there is a clear linear trend between the two attributes. There is a strong positive correlation between the two attributes where skewness is low positive and kurtosis is low negative (in Zone 2 and in Zone 3 above the weak BSR) and where skewness is positive to strong positive and kurtosis is low positive (in Zone 1 toward the Hikurangi Channel and in Zone 3 above the strong BSR). Skewness and kurtosis were crossplotted using the same scales that defined the color bars for each respective attribute.
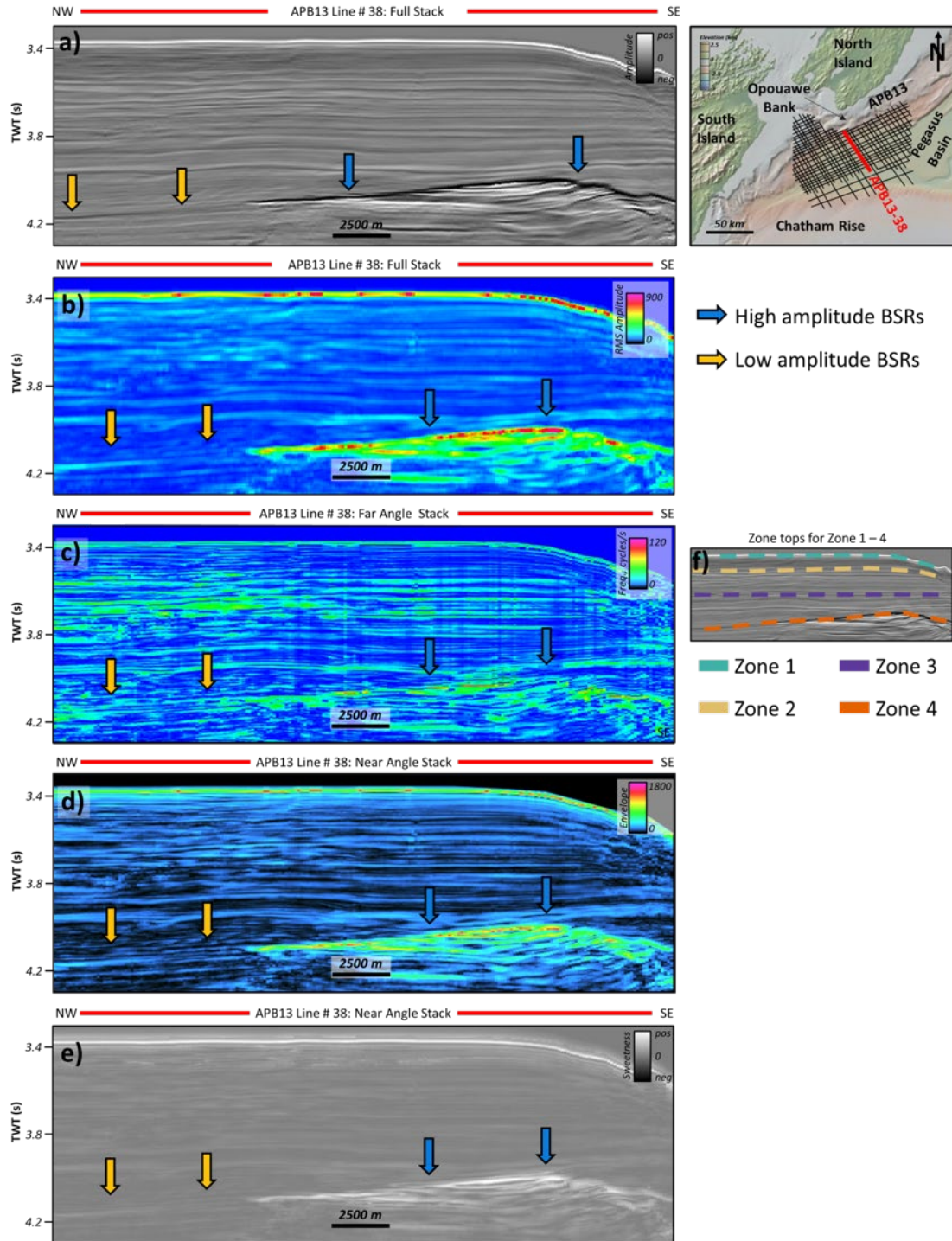
Fig. 11 a full stack seismic line with high and low amplitude BSRs, **b** RMS amplitude attribute, **c** instantaneous frequency attribute, **d** envelope attribute, **e** sweetness attribute, and **f** zones 1 – 4 on the full stack seismic line. All attributes are calculated on the full stack seismic line with high and low amplitude BSRs shown by the arrows

4.2.3 Supplemental Attributes Results

Only the results from the attributes calculated on the full stack seismic line are shown here, as it was outside the scope of the project to investigate the supplemental attributes' variation across the different angle stacks. However, future work may include investigation of the attribute variation with offset in this study area. In the full stack line, RMS amplitude (Figure 11b) response throughout the GHSZ is generally low to 0, with the exception of the ocean bottom and BSR, especially around the high-amplitude BSR, as would be expected for an amplitude-related attribute. There are slight variations throughout Zone 2 in the non-parallel, possible sediment wave reflectors, and slight enhancement of the weak BSR in Zone 4 where the BSR was discontinuous at the northwest end of the seismic line. Below the high-amplitude BSR seen in the seismic line, there is an interval of high RMS amplitude response, although the response is somewhat smeared.

The instantaneous frequency attribute ranges from 0-120 cycles/s with the highest frequency response at the ocean bottom, between 3.6 and 3.8 seconds (Zone 2), and along the high amplitude BSR (Zone 4). The instantaneous frequency was lowest in Zone 1 immediately below the ocean bottom reflector, and in Zone 3, with thin layers of medium to high frequency. The high frequency response in Zone 2 roughly corresponds to the skewness and kurtosis attribute variations that were seen throughout that zone; there are higher frequencies observed in the interval corresponding to the negative skewness response throughout the sub-parallel reflectors. In both Zone 1, immediately below the ocean bottom, and in Zone 3, the low frequency variations correspond to positive skewness and kurtosis variations, with the exception of kurtosis in the near angle stack through Zone 3. Additionally, there are slightly higher frequency values along the high amplitude BSR that correspond to negative skewness and

kurtosis responses at the same interval. Frequency also has a medium-strength attribute response along the weak/discontinuous and low amplitude BSR (as seen in Figure 11c). Below the BSR, there are several high frequency intervals, with the response falling in a more discrete expression than the RMS amplitude or envelope response.

The envelope attribute (Figure 11d) response was similar to the RMS amplitude response and values ranged from 0 – 1800. There were strong responses at the ocean bottom and along the high-amplitude BSR, respectively, and throughout the main GHSZ, envelope varied from around 0 to 200. Envelope is generally vertically stratified throughout with no strong discernable patterns except for slightly higher envelope in Zone 2. Below the BSR (Zone 4), there were several high envelope intervals. When analyzing the attribute response with offset, both envelope and RMS amplitude increased with offset from around 1000 to 1400 (unit of envelope) and 900 to 1100 (amplitude), respectively, although AVO-type responses were not comprehensively described for the supplemental attributes.

The sweetness attribute calculated on the full stack line shows weak variations throughout the GHSZ, with the ocean bottom and high amplitude BSR being the main strong positive sweetness responses (Figure 11e). Sweetness also generally follows the response pattern similar to the original seismic amplitude line. Below the BSR (Zone 4), there are several thin beds of high positive sweetness following a similar expression as the amplitude and envelope attribute response sub-BSR.

Each of the attributes summarized here appear to follow a similar pattern as the statistical attributes in that they are vertically "stratified" and follow some of the same vertical trends as the original seismic amplitude. This of course is not unexpected, however it may speak to the

attributes' ability to highlight features that are unrelated to amplitude and/or the geology of the basin.

4.3 Machine Learning Results

The output files from the SOM classification are a 2D histogram, 2D color legend, and then a co-rendered 2D color legend and histogram (Figure 12). The 2D histogram identifies the number of clusters from a crossplot of the two SOM projection axes. The main variability of the data is contained within clusters that were closely related to each other in the latent space during classification, and the anomalous data is represented by the outliers. When overlain with the 2D color legend, these colors can be used to identify anomalies in the SOM results. Those vectors classified together by one color are therefore expected to share similarities from the input seismic attributes. On the other hand, facies such as the BSR and ocean bottom facies are classified by a fewer histogram count and are also farther separated from the mixed siliciclastic facies than the variable frequency facies (see Figure 12), which contain a majority of the data and represents the largest cluster in the SOM projection.
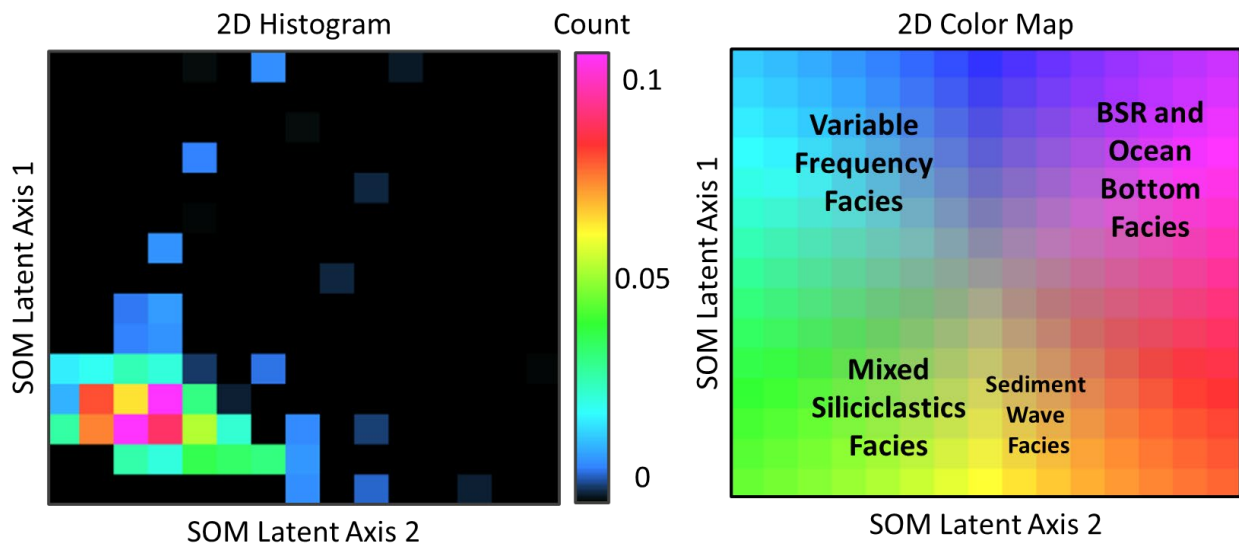
Fig. 12 2D color map and 2D histogram from APB13 line # 38 far angle stack seismic line. The 2D histogram represents the clusters of facies, and helps visualize the connectivity or "distance" the individual facies have from each other

Based on the understanding of the geologic setting and seismic facies present in the Pegasus Basin, the clusters of colors observed in the SOM are correlated with the interpreted seismic facies, geologic features seen in the seismic data, or attribute observations. The three main seismic facies clusters recognized from the seismic attribute and SOM results are 1) high amplitude reflectors representing the ocean bottom facies (including a strong possible ocean bottom side lobe clustered in magenta) and BSR facies, 2) mixed siliciclastic facies representing the majority of the data as fairly continuous, parallel reflectors, and 3) the variable frequency facies that are most closely associated with spectral skewness and kurtosis and instantaneous frequency variations throughout Zones 1 and 3. There is a fourth possible facies adjacent to the Mixed Siliciclastic Facies that is weakly observed in some SOM angle stacks and is termed the "Sediment Wave Facies" referring to the sub-parallel, possible sediment wave reflectors observed in Zone 2. In some SOM angle stacks, this facies is not distinguishable from the Mixed Siliciclastic Facies or only weakly distinguishable in some areas throughout the SOM.

SOM Case	Stack	Zone 1, Ocean bottom - 3.53 sec TWT	Zone 2, 3.53 - 3.8 sec TWT	Zone 3, 3.8 sec TWT - BSR	Zone 4, BSR
Case 1	Full	Ocean bottom and side lobe: continuous, magenta cluster. Below: discontinuous; some variable frequency facies, but predominantly mixed siliciclastic facies	Continuous to discontinuous; green and yellow clusters representing the mixed siliciclastic facies	Continuous to discontinuous; green to blue clusters representing the mixed siliciclastic and variable frequency facies	Continuous to weak/discontinuous toward the central part of the basin; and ocean bottom facies toward the mixed siliciclastic facies where the BSR is weak
	Far	Ocean bottom and side lobe: continuous, BSR and OB cluster. Discontinuous; predominantly green and yellow clusters representing the mixed siliciclastic facies, with very few teal clusters representing the variable frequency facies	Continuous to discontinuous; green and yellow clusters representing the mixed siliciclastic facies	Continuous to discontinuous; mixed siliciclastic and variable frequency facies; more variable frequency clusters than in the Full Stack	Continuous to weak/discontinuous toward the central part of the basin; magenta to green, representing the BSR and ocean bottom facies toward the mixed siliciclastic facies where the BSR is weak
	Near	Ocean bottom and side lobe: continuous clustering of BSR and OB facies, thinner than the full and far stack. Below: discontinuous; some teal representing the variable frequency facies, but predominantly green and yellow clusters representing the mixed siliciclastic facies	Continuous to discontinuous; mixed siliciclastic facies with a few patches of tan/brown clusters representing the high amplitude, sub-parallel facies	Continuous to discontinuous; mixed siliciclastic and variable frequency facies; slightly more variable frequency clusters than in the Full Stack, but fewer than in the Far Angle Stack	Continuous to weak/discontinuous toward the central part of the basin; BSR and ocean bottom facies toward the mixed siliciclastic facies where the BSR is weak; the BSR cluster is thinner than in the full or far angle stacks
Case 2	Full	Thin OB/BSR facies at top. Below, continuous to discontinuous clustering of the mixed siliciclastic facies with patchy clustering of the variable frequency facies toward the western edge of the Hikarangi Channel	Continuous to discontinuous mixed siliciclastic facies with few patches of the variable frequency facies	Continuous mixed siliciclastic facies with large, somewhat continuous patches of the variable frequency facies, especially above the high amplitude BSR	BSR facies over the high amplitude BSR and mixed siliciclastic facies over the low amplitude BSR
	Far	Thin OB/BSR facies at top. Below, continuous clustering of mixed siliciclastic facies with patches of more orange and yellow sediment wave and very few variable frequency facies clusters	Continuous to discontinuous mixed siliciclastic facies	Continuous to somewhat continuous with fewer patches of variable frequency facies above the high amplitude BSR than the Full angle stack	Thicker BSR facies over the high amplitude BSR than the full and near angle stack; mixed siliciclastic facies over the low amplitude BSR
	Near	Thin OB/BSR facies at top. Below, continuous to discontinuous mixed siliciclastic facies with patches of variable frequency facies, however, fewer than the full stack	Continuous to discontinuous mixed siliciclastic facies with few patches of the variable frequency facies, and few tan/yellow sediment wave facies	Continuous mixed siliciclastic facies with somewhat continuous, smaller patches of the variable frequency facies than the full angle stack but more discrete patches than the far angle stack	Thinner BSR facies over the high amplitude BSR than the full and far angle stacks; mixed siliciclastic facies over the low amplitude BSR

Table 3. Result summary table for seismic amplitude and self-organizing maps for SOM Case 1 (calculated from a cropped volume) and SOM Case 2 (calculated between the computed ocean bottom and bottom simulating reflector seismic horizons).
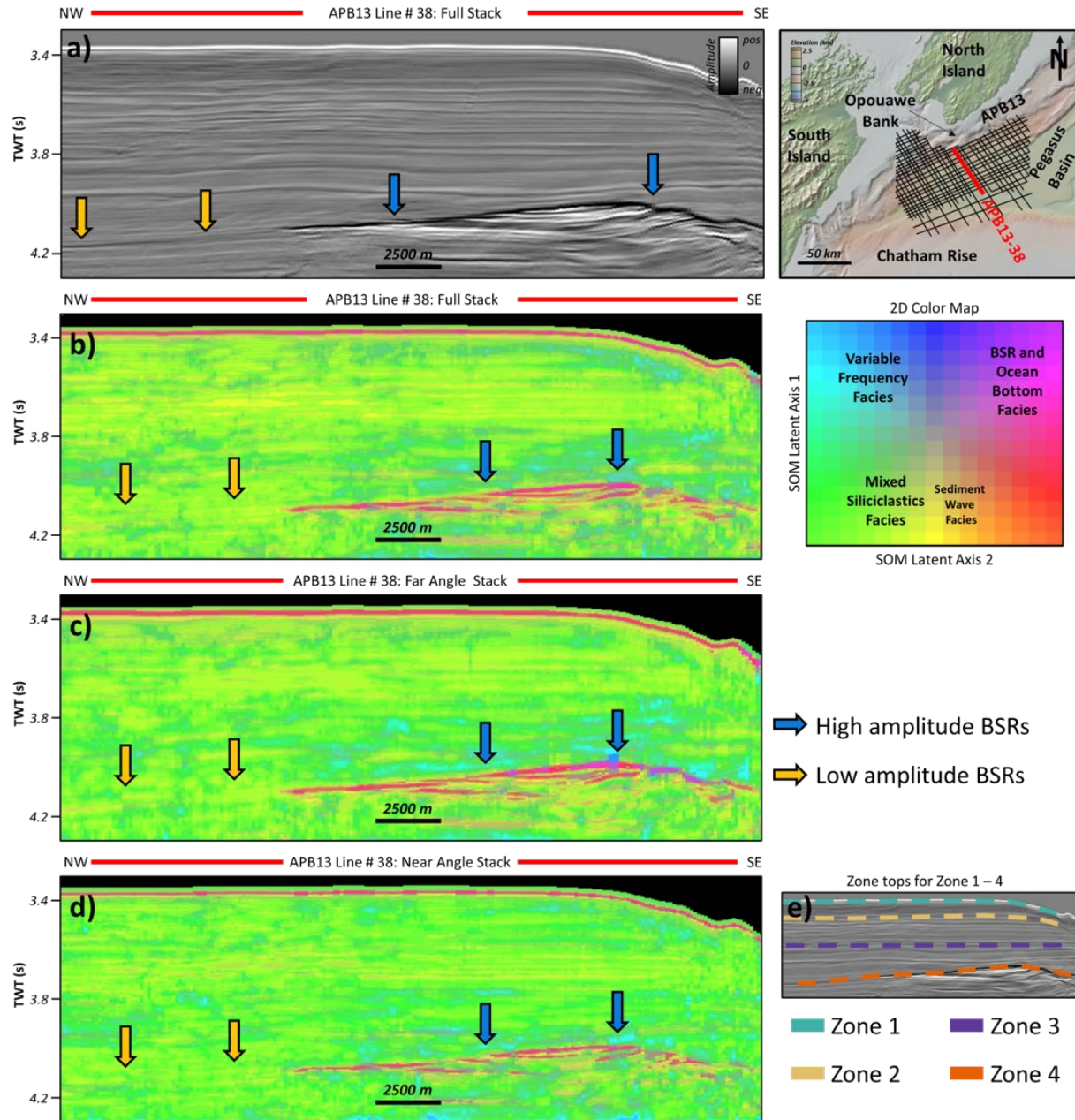
Fig. 13 a full stack seismic line with high and low amplitude BSRs, **b** SOM results calculated from the full stack seismic line, **c** SOM results calculated from the far angle stack, **d** SOM results calculated from the near angle stack, and **e** zones 1 – 4 on the full stack seismic line

4.3.1 SOM Case 1: Computed between ocean bottom to 4.3 seconds TWT

Zone 1 for each of the angle stacks corresponds to a continuous ocean bottom reflector classified in green followed by a strong ocean bottom side-lobe classified by magenta, or the BSR and ocean bottom facies cluster (Figure 13 b – d). Immediately below in Zone 1, the

interval contains primarily continuous to patchy clustering of the mixed siliciclastic facies with some patches of the variable frequency facies toward the Hikarangi Channel on the southeastern end of the seismic line. The variable frequency facies is more apparent in the full and near angle stacks than in the far angle stack. Zone 2 is characterized primarily of mixed siliciclastic facies with patches of stronger yellow clusters (Sediment Wave Facies") that correspond to sub-parallel, possible sediment wave features seen in the 2D seismic. These clusters are more apparent in the full and near angle stacks than the far angle stack. In Zone 3, there is still a majority of the mixed siliciclastic facies, however, above the high amplitude BSR, there are stronger patches of the variable frequency facies, which are more visible in the full and far angle stack than in the near. Zone 4, the BSR, is a strong magenta cluster where the BSR was high amplitude in the 2D seismic, and is classified as mixed siliciclastic where the BSR was weak in the 2D seismic. Below the BSR, there are several smaller clusters of BSR facies and mixed siliciclastic facies clusters. In general, it appears that the SOMs for each of the angle stacks follows the trends as previously mentioned in the attribute analysis section. Additional detailed descriptions of SOM Case 1 results are summarized in Table 3.
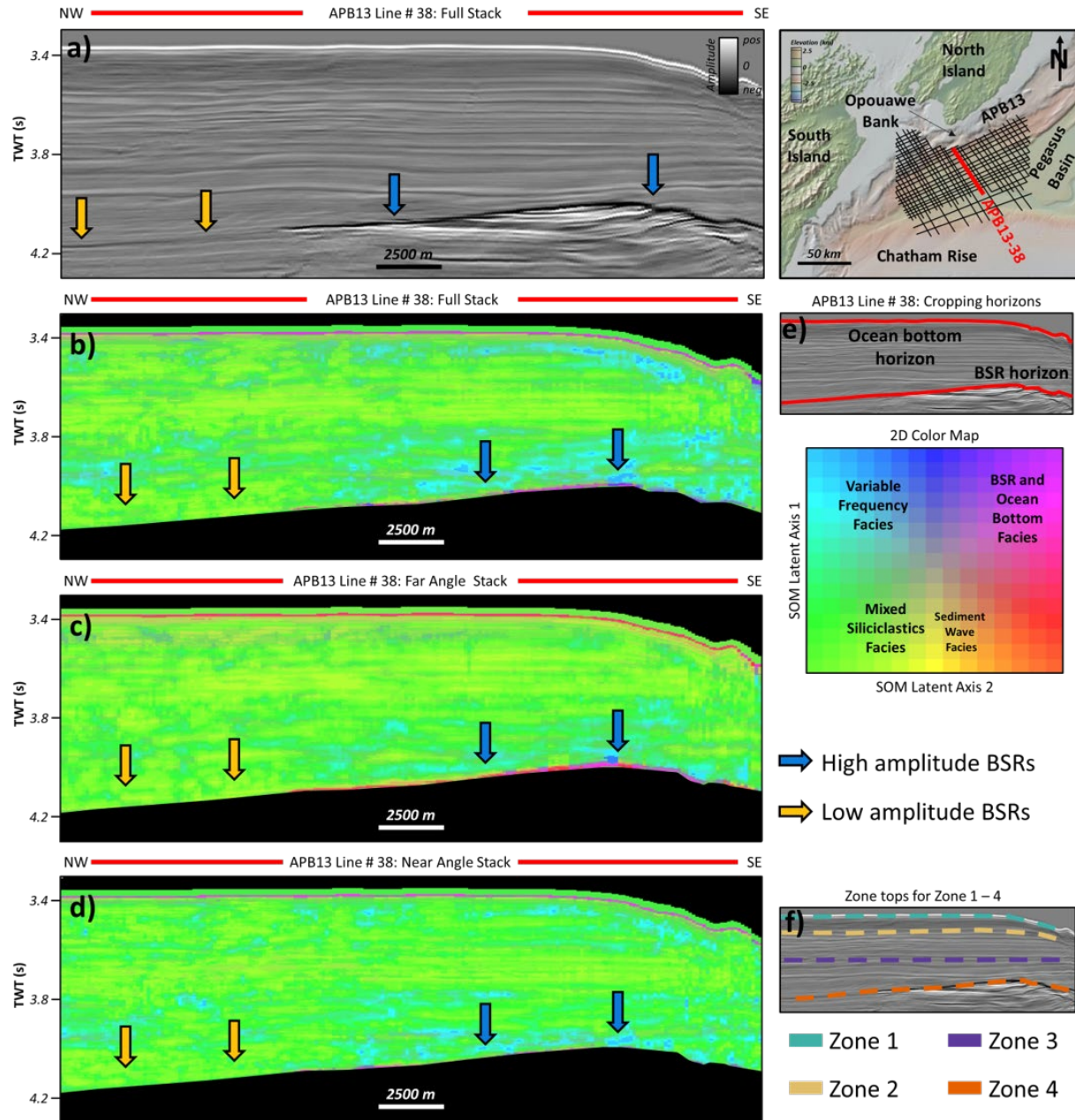
Fig. 14 a full stack seismic line showing high and low amplitude BSRs, **b** SOM results calculated from the full stack seismic line between the ocean bottom and BSR horizons, **c** SOM results calculated from the far angle stack seismic line between the ocean bottom and BSR horizons, **d** SOM results calculated from the near angle stack seismic line between the ocean bottom and BSR horizons, **e** ocean bottom horizon and BSR horizon for vertical window cuttoff, and **f** zones 1 – 4 on the full stack seismic line

4.3.2 SOM Case 2: Computed between ocean bottom horizon to BSR horizon

The results for the SOMs computed between the ocean bottom and BSR horizons were

more differentiable than the SOM Case 1. Zone 1 for each of the angle stacks corresponds to a

continuous ocean bottom reflector and then variable clustering for each of the three angle stacks (Figure 14 b – d). In the full stack, there are larger patches of the variable frequency facies toward the southeastern end of the seismic line, with few similar patches in the near, and almost none in the far angle stack. However, in the far angle stack (Figure 14c), there are several beige clusters that follow the low-amplitude trough response in the 2D seismic line throughout Zone 1; these clusters are not observed in any other SOM angle stack. In Zone 2 the clustering is fairly continuous mixed siliciclastic facies with a few of the sediment wave facies clusters through the sub-parallel, possible sediment wave reflectors seen in the 2D seismic line; Zone 2 shows no significant variations among the angle stacks. Zone 3 contains both mixed siliciclastic facies and large patches of the variable frequency facies, which are more evident in the full stack than far and near, though the near stack patches appear more discrete than the other two angle stacks. Zone 4 contains the BSR shown by the magenta facies where the BSR was high amplitude in the 2D seismic, and is characterized by the mixed siliciclastic facies where the BSR was low amplitude in the 2D seismic. No data was classified below the BSR in SOM Case 2. More detailed descriptions of SOM Case 2 results are summarized in Table 3.

5. Discussion

The discussion will first cover the attribute analysis of the spectral and supplemental attributes, and make comments on possible limitations and considerations for interpretations and future application of attributes. The discussion on SOM Case 1 and Case 2 will follow the attribute discussion, and include comparisons between the two cases and which case was better able to delineate the attenuation-related clusters from the background facies, with SOM Case 2 resulting in more robust frequency- and attenuation-related clusters.

5.1 Attribute Analysis

5.1.1 Spectral Skewness Attribute

Skewness is used to define how much a dataset deviates from the normal distribution of a dataset (Figure 3). When comparing the spectral skewness attribute's response across the angle stacks to the original seismic amplitude, it is apparent that, while amplitude does play a role in skewness response along the bottom-simulating reflector, amplitude alone is not a significant contributing factor to the major variations seen in the skewness response. Rather than a direct correlation between amplitude and skewness, it is likely that, specifically within the sub-parallel reflector interval seen from 3.53-3.8 seconds in the seismic amplitude line (Figures 6b and 7), this is due to an underlying geologic feature causing the small-scale amplitude variation and reflector shape. These anomalous reflectors follow a sediment wave geometry, and based on the interpretation of the geologic setting and deposition within the Pegasus Basin, they may correspond to the sediment wave facies that were described by Lewis and Pantin (2002). There are minor variations in the supplemental attribute lines, most notably an increase in the instantaneous frequency and low-amplitude attribute variations in the envelope and RMS amplitude. Envelope can give indications as to lithology and porosity, and considering that instantaneous frequency also can be used to enhance thin-bed tuning, these variations could also correspond to tuning effects throughout the thinner-bedded interval.

Zone 1 and Zone 3 contain the strongest positive skewness responses, which also correspond to lower frequencies described in the instantaneous frequency attribute section. The combination of positive skewness with low frequency values indicates that more attenuation is occurring across these intervals, especially compared to zones with high frequency and negative skewness. Positive skewness means the data is skewed toward the lower frequencies, which is

confirmed by the low instantaneous frequency responses. The converse of this is observed by comparing negative skewness intervals with frequency, as well. Zone 2 and 4 both contain intervals of negative skewness in conjunction with higher instantaneous frequency, confirming that negatively skewed data do contain a higher frequency content than positively skewed data. These effects demonstrate the frequency-dependent nature of attenuation.

As described in the spectral skewness attribute results section, there is a stronger negative skewness response (that is, the amplitude *of the skewness response* is more negative) visible in the near angle stack compared to the full and far angle stacks. A negative skewness response (see Figure 3) indicates that the seismic frequencies on the left end of the seismic spectrum are being attenuated more than those on the right, therefore skewing the spectrum to the right (which is negative skewness). With respect to the frequency content represented by the seismic amplitude spectrum over which skewness is calculated, this indicates that the *lower* frequencies are being attenuated more than the higher frequencies (also see Appendix C Figure 2). When considering the expected attenuation within near angle stacks, there is a lower expected attenuation, and therefore, a higher frequency content, within the near angles (between 5-18°) since the seismic waves do not have to travel through the earth as much as to the far (between 32-45°) angles. This correlates with the skewness response that is visible across the different angle stacks. While the near angle stack shows a strong negative skewness response, the far angle stack shows a weak negative to 0 skewness response, which is probably due to attenuation by the Earth causing an impact on the natural attenuation occurring within the hydrates themselves. This phenomenon is especially observed in Zone 2 which shows increasing negative skewness from the far to near angle stack while simultaneously reducing the positive skewness response from far to near angle stack (Figure 8 c and d).

In summary, the spectral skewness attribute delineated two separate zones (Zone 1 and Zone 3) with consistently positive skewness in all three angle stacks. Although some of the variations in the skew-AVO response is likely due to attenuation from offset, the zone boundaries remain constant. The strong positive skewness response in Zone 3 directly above the base of the high amplitude BSR is most likely occurring from gas hydrate accumulation near the base of the GHSZ in Zone 3, whereas the negative skewness response in Zone 2 may correspond to a zone with a low or no concentration of hydrates. Zone 1, especially toward the southeastern end by the Hikarangi Trough, may also contain hydrates evidenced by another strong skewness response, although there is less confidence in this location. Although there exists some uncertainty due to lack of well data and depths of hydrate accumulation, skewness proves to be useful for distinguishing zones in the seismic which are experiencing reduction in frequency and amplitude, and based on the understanding of the hydrate system in the Pegasus Basin, this attenuation is tied to gas hydrates in the GHSZ.

5.1.2 Spectral Kurtosis Attribute

Kurtosis is a statistical measure that defines the "tailedness" of dataset from the mean in a normal distribution (Figure 4) of a dataset. With kurtosis, there is a kurt-AVO response occurring similar to the skew-AVO response described previously. The kurtosis response in Zone 3 is strong positive (high-peaked, large tails) in the far angle stack, whereas in the near angle stack throughout the same zone, the kurtosis response is strong negative (low-peaked, small tails); indeed, the values are curiously nearly opposite in the two different angle stacks. In relationship to the theory of kurtosis, positive kurtosis indicates that there are few outliers and a higher peaked-ness to the data as measured from the spectrum at that sample location, while negative kurtosis indicates more outliers and a lower peaked-ness in the data as measured from the

spectrum at that sample location. So, comparing that to the frequency content of the data, that could mean that, where there is a higher kurtosis response in the far angles, the frequency content contains a narrower spectrum or bandwidth of frequencies compared to the normal distribution. On the other hand, the negative kurtosis implies that there is a broader distribution or bandwidth of frequencies, both high *and* low, when compared to the normal distribution of the data.

In the full and far angle stacks, the strong positive kurtosis response above the high amplitude BSR indicates a narrower bandwidth of data compared to the overlying negative kurtosis in Zone 2. Zone 3 also contains lower frequency, which may indirectly be driving the bandwidth and subsequently, kurtosis response. In the near angle stack, Zone 3, and indeed, nearly the entire GHSZ, contains negative kurtosis. The positive kurtosis in Zone 3 in both the full and far angle stacks is likely due to gas hydrates attenuating the seismic spectrum and reducing the bandwidth of the data. The mechanism of negative kurtosis in Zone 3 in the near angle stack is more difficult to understand, but likely is due to some interaction between attenuation from hydrates and attenuation due to offset; however, this exact response is not well understood.

In summary, kurtosis delineated two primary zones of skewness variation, with a third zone with slight variation that may be correlated with hydrates. Zone 3 exhibited strong kurt-AVO response: positive kurtosis response in the full and far angle stacks, and strong positive in the near angle stack. This variation shows changes in the bandwidth of the data, and in the full and far angles, represents a narrower bandwidth, likely due to hydrate causing attenuation, although there may be an impact from naturally occurring attenuation due to offset. Within Zone 2, there is a strong negative kurtosis response that may represent no hydrates, whereas in Zone 1 along the southeastern edge of the Hikarangi Trough, the strong positive kurtosis may be related

to another thin accumulation of hydrates, albeit the source of hydrates near the ocean bottom

may by biogenic instead of thermogenic, which is expected at the base of the GHSZ. Since

hydrates have been recovered within the shallow sediments of the Pegasus Basin (see Figure 1),

there is likelihood the strong attenuation in Zone 1 also corresponds to gas hydrate accumulation.

Although there is some uncertainty due to lack of well data to confirm intervals with hydrate

accumulation, based on the understanding of the GHSZ in the Pegasus Basin, the kurtosis

response and variation is likely due to discontinuous zones of gas hydrate accumulation.

Spectral Attribute Considerations and Summary

Both skewness and kurtosis attributes show a positive attribute response that corresponds

to the strong BSR seen throughout the seismic amplitude volume. However, to varying degrees

of visibility, usually greater in the far-angle stack and decreasing toward the near, both attributes

also show positive attribute response where the BSR was weak or discontinuous. This is

contrasting with the instantaneous and RMS amplitude attributes which are less consistent at

resolving the BSR along the weak section. And, as stated before, although the goal is not to

enhance weak BSRs, the skewness and kurtosis's ability to detect attenuation response above the

BSR is a strong indication that hydrates are indeed present, even without a strong BSR. Taking

the BSR as an indicator of hydrates within the GHSZ and based on the interpretation of skewness

and kurtosis' relationship to attenuation, these spectral attributes help reduce uncertainty, similar

to the traditional direct hydrocarbon indicators that do not explicitly confirm hydrocarbon

presence, but are commonly used to de-risk a reservoir or exploratory location.

However, although there is hydrate recovered from drop cores along the Opouawe Bank

(see Figure 5 and Bialas, 2011), indicating that hydrates may exist from the base of the GHSZ up

to the surface of the ocean bottom, the skewness and kurtosis attributes show the strongest

response toward the base of the GHSZ, although there is a zone of lower skewness seen in the western extents in the full and angle stacks, which does not correspond to any particular amplitude feature or anomaly. It seems more plausible that there are discontinuous zones or patches of hydrates throughout the GHSZ rather than one solid hydrate-filled sediment package; indeed, studies have shown that hydrates can occur in discontinuous intervals of the subsurface of the GHSZ (Cordon et al., 2006; Guerin and Goldberg, 2002).

Another useful aspect of the spectral attributes is that they were able to distinguish statistical variations in the amplitude and frequency spectrum that were seldom apparent in the supplemental attributes. In particular, spectral skewness and kurtosis show strong responses and skew- or kurt-AVO variations in Zone 3, which do not correspond to any particular amplitude anomaly or supplemental attribute feature, with the exception of the instantaneous frequency attribute.

Based on the results of the skewness and kurtosis crossplot (Figure 10), there is a clear positive correlation between skewness and kurtosis, especially throughout intervals that likely correspond to attenuation from gas hydrate accumulation. The simple cross-correlation is useful as an additional visual representation of how these attributes are related to each other and potential zones of hydrate accumulation, as well as being a simple method to quality control check the results and interpretation from the machine learning.

And lastly, based on the observations from the spectral attributes in the Pegasus Basin, these attributes have the potential to be considered another type of DHI (direct hydrocarbon indicator). Although there are some uncertainties in the exact locations of gas hydrates due to lack of well data in the Pegasus Basin, even well-accepted DHIs do not explicitly confirm the existence of hydrocarbons, but rather indicate hydrocarbon existence based on the attribute

theory, concepts, and thorough, scientific interpretation of the attribute response. In the same way, spectral attributes give a response based on the statistical shape of the seismic spectrum and, when interpreting that in terms of attenuation specifically in a gas hydrate setting, can indicate zones with gas hydrates.

5.1.3 Supplemental Attributes—RMS Amplitude, Instantaneous Frequency, Envelope, and Sweetness

The results from the instantaneous frequency attribute show high frequency variations at the same locations where there is a negative spectral skewness response, indicating that these variations are related to frequency responses, rather than changes in the amplitude volume of the seismic or lithology. This is consistent with expectations that high frequencies are being attenuated throughout the GHSZ, and the corresponding skewness and kurtosis attributes show (positive) responses that indicate lower peak frequencies compared to a non-hydrate filled zone. Furthermore, the instantaneous frequency attribute follows a somewhat similar zonation pattern; for example, low frequency in Zones 1 and 3 that correspond to positive skewness and kurtosis in the same zones, and high frequency in Zone 2 that corresponds to negative skewness. These similar patterns are not easily observed in the other supplemental attributes, which, interestingly, are closer related to amplitude (with the exception of sweetness), indicating that the spectral attributes correspond more to frequency variations than amplitude variations. Additionally, the frequency attribute may be able to enhance visualization of the weak BSR toward the northwest end of the seismic line (Figure 11 a and c). Indeed, there was an interesting increase in frequency with offset observed in the central part of the Hikarangi Trough where the BSR was weak or discontinuous, and while this was outside the main seismic section of study, future work may include further investigation on the frequency variation along the BSR. Within the main seismic crop of study, the strong frequency response throughout the non-parallel, possible sediment wave

reflectors also corresponds to the spectral attribute response in the full stack and variations observed between the far and near angle stacks.

The results from the envelope and RMS amplitude generally correspond to the high amplitude seen in the seismic amplitude volume. Below the BSR, the RMS amplitude, envelope, and sweetness responses all point toward hydrocarbon accumulation. The sweetness attribute, for example, which is calculated from the frequency and envelope attribute and often used to delineate hydrocarbon-filled sands (or "sweet" spots), shows a strong positive response below the high amplitude BSR; this response is likely due to trapped free gas below the GHSZ. The trapped free gas creates the strong impedance contrast between the hydrate-filled sediments in the GHSZ and the free gas in the zone below, therefore creating a strong BSR. RMS amplitude and envelope are also commonly used to indicate hydrocarbon accumulation, creating a strong case for free gas below the GHSZ.

While the supplemental attributes proved useful for highlighting the BSR at the base of the GHSZ, these attributes proved to be less indicative of attenuation itself, and show fewer correlations between their attribute response and the interesting spectral attribute responses and variations observed between the angle stacks. Nevertheless, they do show a clear delineation between amplitude- and frequency-related responses and what attributes are most appropriate for quantifying attenuation, in addition to providing the necessary supplemental attributes for machine learning.

5.2 Self-organizing Maps

At its core, self-organizing maps is a dimensionality-reduction technique that allows a researcher to input multiple attributes into a machine learning algorithm and analyze the output feature maps or clusters of the data. The implications of using SOM to analyze attenuation

throughout the GHSZ is that there will be influence from not only the spectral shape attributes and their variations throughout the GHSZ, but also from the supplemental attributes, which proved less useful for highlighting attenuation effects. Therefore, it is expected that while the combination of input attributes will give clues to the attenuation response through the GHSZ, attributes that use strictly frequency or attenuation attributes may prove more robust in delineating the subtle changes observed by the spectral shape attributes.

5.2.1 Comparison between SOM Case 1 and 2

Comparing the two SOM cases, it appears that running machine learning between a smaller interval allows for more detailed classification, as it excludes more of the extraneous outliers from the classification, essentially giving fewer pixels to classify. Therefore, if horizons are available, it is recommended that for future workflows, data be run between two bounding horizons for more robust and discrete classification. Comparing SOM Case 1 and 2, it appears that Case 1 is more sensitive to the small-scale amplitude variations seen in Zone 2, which contain the sub-parallel, possible sediment wave reflector features. Case 2 appears to be more sensitive to the frequency-related attribute variations in Zone 3, especially above the high amplitude BSR; Case 2 also exhibits a more distinct clustering of the variable frequency facies in Zone 1 compared to Case 1. The spectral attributes—skewness and kurtosis—especially showed large variations across angle stacks in Zone 3, with kurtosis varying from strong positive in the far angle stack to strong negative in the near angle stack. This likely contributed to more defined classification in that zone for *both* SOM Case 1 and 2.

SOM Considerations and Summary

The primary clusters in both SOM Case 1 and 2 are the ocean bottom facies and BSR facies cluster, the mixed siliciclastic facies clusters, the variable frequency facies clusters, and

where present, the sediment wave facies clusters. Although each attribute is weighted equally when computing the SOM throughout the GHSZ, certain SOM clusters are created because individual attributes have stronger or weaker responses in particular areas. For example, the RMS amplitude, envelope, sweetness, and instantaneous frequency each have a strong and relatively distinct ocean bottom and BSR response, whereas the spectral skewness and kurtosis have less distinct responses along the BSR, although fairly consistent along the ocean bottom. Therefore, the strong ocean bottom and BSR facies cluster is due largely to the supplemental attribute's input rather than strong responses from the spectral attributes. Likewise, the variable frequency facies is closer related to variations in the spectral attributes and instantaneous frequency attribute than the RMS, envelope, or sweetness attributes. In general, the results from both SOM cases are useful for delineating amplitude-related features from frequency-related features, and as was previously discussed, indicating attenuation where frequency and spectral attributes showed strong responses.

Although more work could be done to enhance the SOM classification of hydrates through the GHSZ, especially through implementation of other frequency- or attenuation-related attributes, the SOM models presented here are shown to distinguish two primary zones (Zone 1 and 3) of high attenuation or frequency variations, and one zone (Zone 2) related more closely to underlying geologic features (sediment waves). Furthermore, computing self-organizing maps between two seismic horizons is shown to enable more robust clustering by reducing the amount of data that needed to be classified.

6. Conclusions

Gas hydrates are a complex and, in many areas, poorly imaged geologic phenomenon that exist in marine and permafrost settings. In the APB-13 dataset from the Pegasus Basin offshore

the east coast of the North Island of New Zealand, gas hydrates are indicated from both clear and discontinuous BSRs, in addition to methane hydrate-bearing drop cores recovered throughout the Pegasus Basin. However, due to the inconsistent nature of BSRs, other methods are needed to identify gas hydrates within the gas hydrate stability zone. Attenuation, closely associated with hydrate filling the pore-space within the GHSZ, measured by statistical attributes—skewness and kurtosis—is proposed as a method to identify hydrates in the absence of BSRs. These statistical attributes, in combination with instantaneous and RMS amplitude attributes, are used to determine the attenuation response and variation within the GHSZ of the APB-13 2D seismic dataset, and used as input into a SOMs machine learning algorithm. The results from the attribute analysis show that the frequency-related attributes—instantaneous frequency and the spectral/statistical attributes skewness and kurtosis—are able to highlight attenuation throughout the hydrate-saturated zone within the GHSZ. Additionally, based on these attribute responses, it appears that the hydrates in the Pegasus Basin are discontinuous throughout the GHSZ, as evidence by a high skewness and kurtosis response directly above the high amplitude BSRs overlain by a zone of negative skewness and kurtosis, which may be indicative of a hydrate-free interval. As the frequency/spectral-related attribute response/variation in Zone 3 does not correspond to any noticeable amplitude attribute variation or appear within the original seismic amplitude volume, we conclude that it is related to attenuation of frequencies due to the gas hydrates.

Based on the SOM results, there was a corresponding response at the areas where the frequency attributes showed peak responses/variations. As expected from the skew-AVO and kurt-AVO analysis of the spectral attributes, the variations often reach their peak with offset in the SOM results. Comparing the two SOM cases, it is observed that running machine learning

between a smaller interval allows for more discrete classification of data, and it is therefore recommended to calculate attributes and machine learning implementation across a narrower user-defined window or cropping horizons.

From this study, it is shown that statistical/spectral attributes—skewness and kurtosis—are able to measure the attenuation variations within the GHSZ zone of the Pegasus Basin APB-13 2D seismic dataset. Based on these results and interpretations, it is recommended that spectral attributes be applied to other areas that have suspected gas hydrates but perhaps sparse BSRs or well data, in addition to settings with confirmed gas hydrates and well or core data. Future work, including synthetic modeling of hydrates and attributes, will be useful for determining how saturation of hydrates and varying lithologies impacts attenuation response, and provide more quantitative means to measure attenuation in seismic data.

6.1 Future Work Remarks

Future work may include investigating the frequency variations seen along the weak/discontinuous BSR through the central portion of the Hikarangi Trough (in the larger, uncropped seismic line; see Figure 5 and 6) and determining the nature of the attenuation response below the GHSZ and the applicability of spectral attributes to resolve a weak/discontinuous BSR. Skewness and kurtosis both displayed attribute responses, albeit somewhat subtle, along the low amplitude, discontinuous BSR, and more work may determine whether these attributes are useful for BSR-related studies. Furthermore, while the brief synthetic study discussed in Chapter 2 showed spectral attributes' response through gas hydrates, future work should include more detailed models with a proper Q-factor and preferably be based on real-world well log data, where available.

7. References

AASPI Researchers (2020) Volumetric Self-organizing maps for 3D seismic facies analysis - Program som3d, University of Oklahoma Mewbourne College of Earth and Energy, https://mcee.ou.edu/aaspi/documentation.html. Accessed 02/10/2022

Allen, R (2020) A Gentle Introduction to Machine Learning Concepts. Medium, Machine Learning in Practice, https://medium.com/machine-learning-in-practice/a-gentle-introduction-to-machine-learning-concepts-cfe710910eb. Accessed 15 February 2023

Bedle H (2019) Seismic attribute enhancement of weak and discontinuous gas hydrate bottom-simulating reflectors in the Pegasus Basin, New Zealand. Interpretation 7:SG11–SG22. https://doi.org/10.1190/INT-2018-0222.1

Berndt C, Bünz S, Clayton T, et al (2004) Seismic character of bottom simulating reflectors: examples from the mid-Norwegian margin. Marine and Petroleum Geology 21:723–733. https://doi.org/10.1016/j.marpetgeo.2004.02.003

Best AI, Priest JA, Clayton CRI (2010) A resonant column study of the seismic properties of methane-hydrate-bearing sand. In: Riedel M et al (ed) Geophysical Characteristics of Gas Hydrates. Society of Exploration Geophysicists Geophysical Developments Series No. 14. pp 337 – 347 https://doi.org/10.1190/1.9781560802197

Bialas J (2011) FS SONNE Cruise Report SO-214 NEMESYS. IMF-GEOMAR report 47, doi: 10.3289/ifm-geomar_rep_47_2011

Biot MA (1956a) Theory of propagation of elastic waves in a fluid saturated, porous solid. I. Low-frequency range, J. Acoust. Soc. Am., 28, 168–178.

Biot MA (1956b) Theory of propagation of elastic waves in a fluid saturated porous solid. II. High frequency range, J. Acoust. Soc. Am., 28, 179–191.

Bland KJ, Uruski CI, Isaac MJ (2015) Pegasus Basin, eastern New Zealand: A stratigraphic record of subsidence and subduction, ancient and modern. New Zealand Journal of Geology and Geophysics 58:319–343. https://doi.org/10.1080/00288306.2015.1076862

Boswell R, Hutchinson D (2005) Changing Perspectives on the Resource Potential of Methane Hydrates. NETL Methane Hydrate Newsletter

Castagna JP, Sun S, Siegfried RW (2003) Instantaneous spectral analysis: Detection of low-frequency shadows associated with hydrocarbons. The Leading Edge 22:120–127. https://doi.org/10.1190/1.1559038

CGG Services (Singapore) Pte. Ltd., Anadarko New Zealand Ltd (2014) Seismic Data Processing Report – APB-13-2D Pegasus Basin 2D PEP54861; NZP&M, Ministry of Business, Innovation & Employment (MBIE), New Zealand. Unpublished Petroleum Report PR5170

Chand S, Minshull T (2004) The effect of hydrate content on seismic attenuation: A case study for Mallik 2L-38 well data, Mackenzie delta, Canada. Geophys Res Lett 31:L14609. https://doi.org/10.1029/2004GL020292

Chenin J, Bedle H (2020) Multi-attribute machine learning analysis for weak BSR detection in the Pegasus Basin, Offshore New Zealand. Mar Geophys Res 41:21. https://doi.org/10.1007/s11001-020-09421-x

Chopra S, Marfurt KJ (2007) Seismic Attributes for Prospect Identification and Reservoir Characterization. Society of Exploration Geophysicists

Clairmont R, Bedle H, Marfurt K, Wang Y (2021) Seismic Attribute Analyses and Attenuation Applications for Detecting Gas Hydrate Presence. Geosciences 11:450. https://doi.org/10.3390/geosciences11110450

Collier, T (2015) The Geology of Pegasus Basin Based on Outcrop Correlatives in Southern Wairarapa and Northeastern Marl-Borough, New Zealand. Master's Thesis, Victoria University of Wellington, Auckland, New Zealand, 2015. Available online: http://hdl.handle.net/10063/4831 (accessed on 10 October 2022).

Cordon I, Dvorkin J, Mavko G (2006) Seismic reflections of gas hydrate from perturbational forward modeling. Geophysics 71:F165–F171. https://doi.org/10.1190/1.2356909

Dallimore, SR, Collett, TS, Uchida T (1999) Overview of science program, JAPEX/JNOC/GSC Mallik 2L-38 gas hydrate research well. Geological Survey of Canada. Bulletin 544, pp 11-17

Davies RJ, Maqueda MÁM, Li A, Ireland M (2021) Climatically driven instability of marine methane hydrate along a canyon-incised continental margin. Geology 49:973–977. https://doi.org/10.1130/G48638.1

Davogustto O, de Matos MC, Cabarcas C, et al (2013) Resolving subtle stratigraphic features using spectral ridges and phase residues. Interpretation 1:SA93–SA108. https://doi.org/10.1190/INT-2013-0015.1

de Matos MC, Davogustto O, Cabarcas C, Marfurt K (2012) Improving reservoir geometry by integrating continuous wavelet transform seismic attributes. In: SEG Technical Program Expanded Abstracts 2012. Society of Exploration Geophysicists, pp 1–5

Dev A, McMechan GA (2010) Interpreting structural controls on hydrate and free-gas accumulation using well and seismic information from the Gulf of Mexico. GEOPHYSICS 75:B35–B46. https://doi.org/10.1190/1.3282680

Dvorkin J, Nur A (1993) Dynamic poroelasticity: A unified model with the squirt and the Biot mechanisms. Geophysics 58:524–533. https://doi.org/10.1190/1.1443435

Dvorkin J, Gutierrez MA, Grana D (2014) Seismic Reflections of Rock Properties. Cambridge University Press, https://doi.org/10.1017/CBO9780511843655

Dvorkin J, Uden R (2004) Seismic wave attenuation in a methane hydrate reservoir. The Leading Edge 23:730–732. https://doi.org/10.1190/1.1786892

Dvorkin JP, Mavko G (2006) Modeling attenuation in reservoir and nonreservoir rock. The Leading Edge 25:194–197. https://doi.org/10.1190/1.2172312

Englezos P (1993) Clathrate hydrates. Industrial & Engineering Chemistry Research 32:1251–1274

EPI Group, Anadako New Zealand Ltd (2014) APB-13-2D Pegasus Basin 2D quality Assurance Report, PEP 54861 Marine 2D Seismic Survey PEP 54861; NZP&M, Ministry of Business, Innovation & Employment (MBIE), New Zealand. Unpublished Petroleum Report PR5169

~~GEBCO Compilation Group (2022) GEBCO 2022 grid, accessed on 12/16/2022~~

Goodway B (2001) AVO and Lamé Constants for Rock Parameterization and Fluid Detection. Canadian Society of Exploration Geophysicists 26:06

Grossmann A, Morlet J (1984) Deomposition of Hardy functions into square integrable wavelets of constant shape. SIAM Journal on Mathematical Analysis, 15:726–736

Guerin G, DS Goldberg (2002) Sonic waveform attenuation in gas hydrate-bearing sediments from the Mallik 2L-38 research well, Mackenzie Delta, Canada. J Geophys Res 107:2088. https://doi.org/10.1029/2001JB000556

Han D, Nur A, Morgan D (1986) Effects of porosity and clay content on wave velocities in sandstones. Geophysics 51:2093–2107. https://doi.org/10.1190/1.1442062

Hart BS (2008) Channel detection in 3-D seismic data using sweetness. Bulletin 92:733–742. https://doi.org/10.1306/02050807127

Hart B (2011) An Introduction to Seismic Interpretation. AAPG Datapages, Discovery Series 16

Harison, S (2010) Natural Gas Hydrates. Standford University coursework, http://large.stanford.edu/courses/2010/ph240/harrison1/. Accessed 21 February 2023

Helgerud M (2001) Wave speeds in gas hydrate and sediments containing gas hydrate: A laboratory and modeling study. PhD Dissertation, Stanford University

Hilterman F, Van Schuyver C (2003) Seismic wide-angle processing to avoid NMO stretch. In: SEG Technical Program Expanded Abstracts 2003. Society of Exploration Geophysicists, pp 215–218

Holbrook WS, Hoskins H, Wood WT, et al (1996) Methane Hydrate and Free Gas on the Blake Ridge from Vertical Seismic Profiling. Science 273:1840–1843. https://doi.org/10.1126/science.273.5283.1840

Hornbach MJ, Holbrook WS, Gorman AR, et al (2003) Direct seismic detection of methane hydrate on the Blake Ridge. GEOPHYSICS 68:92–100. https://doi.org/10.1190/1.1543196

Hussein M, Stewart RR, Sacrey D, et al (2021) Unsupervised machine learning using 3D seismic data applied to reservoir evaluation and rock type identification. Interpretation 9:T549–T568. https://doi.org/10.1190/INT-2020-0108.1

King SE (2017) The Tectonic Evolution of Pegasus Basin and the Hikurangi Trench, offshore New Zealand. Master's Thesis, Colorado School of Mines, Golden, Colorado, 2017

Klimentos T, McCann C (1990) Relationships among compressional wave attenuation, porosity, clay content, and permeability in sandstones. GEOPHYSICS 55:998–1014. https://doi.org/10.1190/1.1442928

Kohonen T (1982) Self-organizing formation of topologically correct feature maps. Biological Cybernetics 43:59-69. https://doi.org/10.1007/BF00337288

Kohonen T (1990) The self-organizing map. Proc IEEE 78(9):1464–1480

Kohonen T (2001) Self-Organizing Maps. Springer Berlin Heidelberg, Berlin, Heidelberg, https://doi.org/10.1007/978-3-642-56927-2

Kroeger KF, Plaza-Faverola A, Barnes PM, Pecher IA (2015) Thermal evolution of the New Zealand Hikurangi subduction margin: Impact on natural gas generation and methane hydrate formation – A model study. Marine and Petroleum Geology 63:97–114. https://doi.org/10.1016/j.marpetgeo.2015.01.020

La Marca K, Silver C, Bedle H, Slatt R (2019) Seismic facies identification in a deepwater channel complex applying seismic attributes and unsupervised machine learning techniques. A cas study in the Tarinaki Basin, New Zealand. 89th Annual Internation Meeting. SEG, pp. 2059-2063. Expanded abstracts. https://doi.org/10.1190/segam2019-3216705.1

La Marca K, Bedle H (2021) Deepwater seismic facies and architectural element interpretation aided with unsupervised machine learning techniques: Taranaki basin, New Zealand. Marine and Petroleum Geology 136:105427. https://doi.org/10.1016/j.marpetgeo.2021.105427

Lewis KB, Pantin HM (2002) Channel-axis, overbank and drift sediment waves in the southern Hikurangi Trough, New Zealand. Marine Geology 192:123–151. https://doi.org/10.1016/S0025-3227(02)00552-2

Li F, Zhou H, Li L, Marfurt KJ (2015) Seismic Spectral Attributes of Apparent Attenuation: Part 1 - Methodology. In: SEG Technical Program Expanded Abstracts 2015. Society of Exploration Geophysicists, New Orleans, Louisiana, pp 1966–1970

Li F, Verma S, Zhou H, et al (2016) Seismic attenuation attributes with applications on conventional and unconventional reservoirs. Interpretation 4:SB63–SB77. https://doi.org/10.1190/INT-2015-0105.1

Li F, Liu R, Lou Y, Liu N (2021) Revisit seismic attenuation attributes: Influences of the spectral balancing operation on seismic attenuation analysis. Interpretation 9:T767–T779. https://doi.org/10.1190/INT-2020-0186.1

Liu P, Huang H, Hu L, et al (2022) Hydrate Attenuation Characteristics Based on the Patchy-Saturation Model. Front Earth Sci 10:831405. https://doi.org/10.3389/feart.2022.831405

Lubo-Robles D, Bedle H, Marfurt KJ, Pranter MJ (2023) Evaluation of principal component analysis for seismic attribute selection and self-organizing maps for seismic facies discrimination in the presence of gas hydrates. Marine and Petroleum Geology 150:106097. https://doi.org/10.1016/j.marpetgeo.2023.106097

Maslin M, Owen M, Betts R, et al (2010) Gas hydrates: past and future geohazard? Phil Trans R Soc A 368:2369–2393. https://doi.org/10.1098/rsta.2010.0065

Mavko G, Nur A (1975) Melt squirt in the asthenosphere. Journal of Geophysical Research 80:1444–1448. https://doi.org/10.1029/JB080i011p01444

Mavko G, Murkerji T, Dvorkin J (2013) The Rock Physics Handbook, 5th edn. Cambridge University Press

Taner MT, Koehler F, Sheriff RE (1979) Complex seismic trace analysis. GEOPHYSICS 44:1041–1063. https://doi.org/10.1190/1.1440994

Toro F (2020) NETL Methane Hydrate R&D Program, Program Highlights 2000-2020. National Energy Technology Laboratory. https://netl.doe.gov/oil-gas/gas-hydrates

Peyton L, Bottjer R, Partyka G (1998) Interpretation of incised valleys using new 3-D seismic techniques: A case history using spectral decomposition and coherency. The Leading Edge 17:1294–1298. https://doi.org/10.1190/1.1438127

Plaza-Faverola A, Klaeschen D, Barnes P, Pecher I, Henrys S, Mountjoy J (2012) Evolution of fluid expulsion and concentrated hydrates zones across the southern Hikurangi subduction margin, New Zealand: An analysis for depth migrated seismic data. AGU Vol 13 No 8. https://doi.org/10.1029/2012GC004228

Raikes SA, White RE (1984) Measurements of Earth Attenuation From Downhole and Surface Seismic Recordings*. Geophys Prospect 32:892–919. https://doi.org/10.1111/j.1365-2478.1984.tb00745.x

Riedel, M, Willoughby EC, and Chopra S (2010) Geophysical Characteristics of Gas Hydrates. Society of Exploration Geophysicists Geophysical Developments Series No. 14. https://doi.org/10.1190/1.9781560802197

Sahoo SK, North LJ, Marín-Moreno H, et al (2019) Laboratory observations of frequency-dependent ultrasonic P-wave velocity and attenuation during methane hydrate formation in Berea sandstone. Geophysical Journal International 219:713–723. https://doi.org/10.1093/gji/ggz311

Sharma, A (2020) Skewness & Kurtosis Simplified. Medium, Towards Data Science website, https://towardsdatascience.com/skewness-kurtosis-simplified-1338e094fc85. Accessed 16 February 2023

Singh SC, Minshull TA, and Spence GD (1993) Velocity structure of a gas hydrate reflector: Science, 260, 204–207, https://doi.org/10.1126/science.260.5105.204
Taner MT, Koehler F, Sheriff RE (1979) Complex seismic trace analysis. Geophysics 44:1041–1063. https://doi.org/10.1190/1.1440994

Sloan ED (2003) Fundamental principles and applications of natural gas hydrates. Nature 426:353–359. https://doi.org/10.1038/nature02135

Taylor MH, Dillon WP, Pecher IA (2000) Trapping and migration of methane associated with the gas hydrate stability zone at the Blake Ridge Diapir: new insights from seismic data. Marine Geology 164:79–89. https://doi.org/10.1016/S0025-3227(99)00128-0

Uchida T, Matsumoto R, Waseda A, Okui T, Yamada K, Okada S, and Takano O (1999) Summary of physico-chemical properties of natural gas hydrate and associated gas-hydrate-bearing sediments, JAPEX/JNOC/GSC Mallik 2L-38 gas hydrate research well, In Dallimore SR, Uchida T, Collett TS (1999) Scientific results from JAPEX/JNOC/GSC MALLIK 2L-38 gas hydrate research well, Mackenzie Delta, Northwest Territories, Canada. Geological Survey of Canada Bulletin 544, 205–228

Uruski CI, Bland KJ (2011) Pegasus Basin and the Prospects for Oil and Gas. GNS Science Consultancy Report 2010, 291:117

Walia R, Mi Y, Hyndman RD, Sakai A (1999) Vertical seismic profile (VSP) in the JAPEX/JNOC/GSC Mallik 2L-38 gas hydrate research well, In Dallimore SR, Uchida T, Collett TS (1999) Scientific results from JAPEX/JNOC/GSC MALLIK 2L-38 gas hydrate research well, Mackenzie Delta, Northwest Territories, Canada. Geological Survey of Canada Bulletin 544, pp 341-355

Wang Y, Bedle H, Marfurt K (accepted April 2023) Seismic stratigraphy and attenuation of gas-hydrate zones within the Hikurangi and Gondwana Margins, eastern New Zealand. Geophysical Journal International. https://doi.org/10.1093/gji/ggad148

White JE (1975) Computed Seismic Speeds and Attenuation in Rocks with Partial Gas Saturation. Geophysics 40:224–232. https://doi.org/10.1190/1.1440520

Winkler KW, Nur A (1982) Seismic attenuation: Effects of pore fluids and frictional-sliding. Geophysics 47:1–15. https://doi.org/10.1190/1.1441276

Zhan L, Matsushima J (2018) Frequency-dependent P-wave attenuation in hydrate-bearing sediments: a rock physics study at Nankai Trough, Japan. Geophysical Journal International 214:1961–1985. https://doi.org/10.1093/gji/ggy229

Zhao T, Jayaram V, Roy A, Marfurt KJ (2015) A comparison of classification techniques for seismic facies recognition. Interpretation 3:SAE29–SAE58. https://doi.org/10.1190/INT-2015-0044.1

Zhao T, Zhang J, Li F, Marfurt KJ (2016) Characterizing a turbidite system in Canterbury Basin, New Zealand, using seismic attributes and distance-preserving self-organizing maps. Interpretation 4:SB79–SB89. https://doi.org/10.1190/INT-2015-0094.1

Zhao T, Li F, Marfurt KJ (2018) Seismic attribute selection for unsupervised seismic facies analysis using user-guided data-adaptive weights. GEOPHYSICS 83:O31–O44. https://doi.org/10.1190/geo2017-0192.1

Chapter 2, Synthetic Gas Hydrate-bearing Well Log and Seismic Data

1. Introduction

When data scarcity exists within a particular study area or setting, researchers often utilize synthetic data, whether seismic or well data, to further investigate phenomenon or enhance interpretations from their main body of data. Due to lack of well data from the Pegasus Basin, a brief side study was proposed to assess the nature of skewness and kurtosis' response on synthetic seismic created from synthetic well logs with known intervals of hydrate saturation. As this exact approach has never been applied before, it is novel in its application with respect to spectral attributes and hydrates, and a more concrete understanding of the exact mechanisms of attenuation within hydrates will likely lead to increasingly robust modeling in the future. However, the results of this study may aid future workflows in suspected gas hydrate settings that contain abundant seismic data but well log scarcity.

2. Background

Synthetic studies have been performed for many decades to analyze typical petroleum trapping mechanisms as observed in synthetic seismic data (May and Hron, 1978), determine the impact of fluid substitutions on synthetic seismic data and AVO observations (Dvorkin et al., 2007), and even train machine learning algorithms to detect faults in real-world data (Cunha et al., 2020), in addition to a plethora of other applications in seismology and geophysics. For the purpose of this brief study, creating synthetic data allows for strict control of layer thickness, fluid substitution (specifically for gas hydrates and methane gas), and lithology constraint. Although hydrate studies do not fall into the traditional realm of hydrocarbon exploration, the method of fluid substitution is the same, and allows for observations of how the seismic response varies with those fluids (or, in this case, solid hydrates). A study by Cordon et al. (2006) described below

utilized fluid substitutions in synthetic data and the resulting impact on attenuation of the seismic waveform.

Attenuation is energy loss observed in the seismic waveform as amplitude loss (Riedel et al., 2010). Attenuation has been associated with conventional and unconventional oil and gas reservoirs (Dvorkin and Mavko, 2006; Li et al., 2016), and is commonly reported in gas hydrate settings, both within gas hydrates themselves, and in free gas below, where it exists. The quality factor, Q, is the inverse of attenuation, and Dvorkin and Mavko (2006) give the simple formula

$$0.733 \times Q \times \lambda \qquad\qquad \text{Equation 1}$$

to describe the distance over which amplitude decreases by a factor of ten due to the earth's inherent attenuation of elastic waves. Dvorkin (2004) and Dvorkin and Mavko (2006) describe attenuation in terms of the compressional modulus at high and low frequencies by the equation

$$2Q_{Max}^{-1} = (M_H - M_L)/\sqrt{M_H M_L} \qquad\qquad \text{Equation 2}$$

where Q_{Max}^{-1} is the maximum inverse quality factor, and M_H and M_L are the compressional moduli at very high and low frequencies, respectively. In relationship to gas hydrates, Guerin and Goldberg (2002) describe the attenuation observed in the Mallik well by

$$Q_p^{-1} = 0.029 + 0.12 S_{gh} \qquad\qquad \text{Equation 3}$$

where Q_p^{-1} is the p-wave attenuation and S_{gh} is the gas hydrate saturation.

For synthetic studies in gas hydrate settings, synthetic well logs studies have been performed by several researchers to determine the attenuation response, but no studies are known to show correlations between attenuation and spectral shape attributes computed on synthetic data. Several studies on the Mallik 2L-38 well in the McKenzie Delta, Canada, have shown the impact of attenuation on sonic waveforms or synthetic seismic data calculated from sonic and density logs. A study by Guerin and Goldberg (2002) on the Mallik 2L-38 well showed attenuation in the sonic

waveforms in hydrate-saturated intervals (Guerin and Goldberg, 2002), and a study by Dvorkin et al. (2014) showed that synthetic seismic waveforms created using a higher (50 Hz) frequency wavelet exhibited more amplitude losses than seismic created from a lower frequency (20 Hz) wavelet, illustrating the relationship between attenuation and frequency in hydrates. One of the key studies from the Mallik data was by Cordon et al. (2006) and showed the impact of attenuation on synthetic seismic traces and compared the impact of distribution of hydrate saturation on amplitude loss. They estimated Q, the inverse of attenuation, from an empirical equation relating hydrate saturation to p-wave Q, given in Guerin and Goldberg (2002). The synthetic model used a 90 Hz Ricker wavelet and 0-offset data. Their synthetic model showed that, without applying a Q factor, there was minimal to no amplitude loss in hydrate saturated zones when compared to the synthetic data calculated with a Q factor. Then they varied their synthetic model to show the difference in attenuation on the seismic waveform across four difference cases: 1) the original calculated saturation, 2) 50% GH saturation in the top half and the original GH saturation in the bottom half of the data, 3), the original GH saturation in the top half and 50% GH saturation in the lower half, and 4) 50% GH saturation throughout. The results showed that case 4 had the lowest amplitude losses of the 4 scenarios, and the authors state that both case 1 and 4 have a similar traveltime amplitude decay/attenuation (Cordon et al., 2006). This study is an example that attenuation can be observed in synthetic data, however, a Q factor must be applied to quantify the intrinsic attenuation that occurs within hydrates.

3. Methods

3.1 Synthetic Well Logs

P-wave velocity estimation for shallow, non-hydrate bearing sediment along the continental slope and rise range between 1500-1800 m/s (Hamilton, 1980). Studies from hydrate-bearing

sediment in an ocean setting show P-wave velocities of <1680 m/s in the Cascadia Hydrate Ridge, Oregon (Kumar et al, 2006a), >2000 m/s in the Nankai Trough, Southwest Japan (Hato et al., 2004), 2100 m/s in the Blake Ridge, offshore eastern US (Hornbach et al., 2003), and up to 1800 m/s in the Storegga Slide, Voring Plateau, northeast Atlantic margin (Bunz et al., 2005).

Average frequency estimates from the full stack seismic line were between 45-50 Hz. Using a conservative estimate of velocity based on previous hydrate studies and the estimated average frequency, the wavelength of the data was estimated by Equation 1 such that

$$\lambda = V/F \qquad \text{(Eq. 1)}$$

and vertical seismic resolution of the data therefore being

$$vertical\ resolution = \ \lambda/4 \qquad \text{(Eq. 2)}$$

Therefore, the vertical resolution of the data is [(1800 m/s)/(45Hz)]/4, or 10 meters. This value seems reasonable for a shallow marine setting, and is used to determine the thickness of the shale and sandstone layers that build the gas hydrate-bearing synthetic seismic data model. Based on the seismic resolution of 10 meters, the thickness of each layer in the synthetic well logs was set to be 40 ft.

Three models were originally intended to determine the nature of attenuation in hydrates and the impact attenuation has on the skewness and kurtosis attributes. The first proposed model (Model 1) was a simple two-layer model, with layer 1 consisting of homogenous lithology (sandy shale) filled with hydrates continuously filling the layer. Layer 2 was the same lithology as layer 1 but with gas-filled pore space; the contrast between the two pore-filling materials would theoretically create the impedance contrast resulting in a BSR. Model 2 contained alternating layers of sand and shale with gas hydrate filling discontinuous intervals within the GHSZ. The BSR and sub-GHSZ was simulated with a gas-filled shale layer, similar to Model 1.

Model 3 contained alternating layers of sand and shale with gas hydrate from top to base of the GHSZ, and a BSR and sub-GHSZ simulated similar to Models 1 and 2. The layer sequence and lithologies are given in Table 1.

Model 1			
	Lithology	GH Saturation	Pore-filling fluid
Layer 1	Shale	40%	Water
Layer 2	Shale	0	Gas

Model 2			
	Lithology	GH Saturation	Pore-filling fluid
Layer 1	Shale	0%	Water
Layer 2	Sand	0%	Water
Layer 3	Shale	40%	Water
Layer 4	Sand	0%	Water
Layer 5	Shale	0%	Water
Layer 6	Sand	40%	Water
Layer 7	Shale	0%	Water
Layer 8	Shale	40%	Water
Layer 9	Sand	40%	Water
Layer 10	Sand	0%	Water
Layer 11	Shale	40%	Water
Layer 12	Shale	0%	Gas

Model 3			
	Lithology	GH Saturation	Pore-filling fluid
Layer 1	Shale	40%	Water
Layer 2	Sand	40%	Water
Layer 3	Shale	40%	Water
Layer 4	Sand	40%	Water
Layer 5	Shale	40%	Water
Layer 6	Sand	40%	Water
Layer 7	Shale	40%	Water
Layer 8	Sand	40%	Water
Layer 9	Shale	40%	Water
Layer 10	Sand	40%	Water
Layer 11	Shale	40%	Water
Layer 12	Shale	0%	Gas

Table 1 Models 1 – 3 layer sequence and lithologies

The model input parameters were hydrate saturation [h(sat)], porosity (PhiT), and volume of shale (Vsh). The output parameters were a new porosity metric, density, and p- and s-wave velocities. The input and corresponding output values are listed in Table 2.

Input values				
	Porosity (PhiT)	Volume Shale (Vsh)	Density fluid (g/cc)	Vp fluid (m/s)
Shale, 40% GH	0.1	0.7	1	1500
Shale, 0% GH	0.1	0.7	1	1500
Shale, 0% GH, gas-saturated	0.1	0.7	0.68	1300
Sand, 40% GH	0.2	0.3	1	1500
Sand, 40% GH	0.2	0.3	1	1500
Output values				
	Porosity (PhiT)	Density (g/cc)	Vp (m/s)	Vs (m/s)
Shale, 40% GH	0.06	2.4184	3022.098	1239.4
Shale, 0% GH	0.1	2.422	2726.245	1044.9
Shale, 0% GH, gas-saturated	0.1	2.39	2441.906	1051.8
Sand, 40% GH	0.12	2.2888	2761.983	1190.7
Sand, 0% GH	0.2	2.296	2451.623	1054.9

Table 2 Synthetic well log input parameters and values and corresponding output parameters and values.

3.2 Synthetic Seismic

The porosity and velocity logs were used to create the acoustic impedance log between each of the synthetic well log layers. The first approach for determining an appropriate wavelet to convolve with the acoustic impedance log was to extract the statistical wavelet from the APB13 full stack seismic line #38, to replicate the setting of the study area as much as possible. A sampling rate of 4 ms (milliseconds) was used based on the sampling rate of the APB seismic data. However, the extracted wavelet proved to be abnormally pointy, essentially coming to a distinct point at the peak of the wavelet. The second approach was to use a theoretical wavelet, namely the Ricker wavelet. A frequency of 40 Hz was chosen as it closely replicated the frequency estimated from several points throughout the GHSZ in the APB13 seismic line #38.

This wavelet was smoother than the statistical wavelet, however, the statistical wavelet was chosen as it was more closely related to the APB13 data than the Ricker. The third and final approach was to use an Ormsby bandpass filter to create synthetic seismic based on an Ormsby wavelet. The Ormsby wavelet was believed to be less inherently skewed than the statistical wavelet. The bandpass values for the wavelet computation were 5-10-60-90 Hz, and the results for the wavelet and spectrum are shown in Appendix E.

3.3 Seismic Attributes

Once the synthetic trace was converted to a 2D format and saved as a .segy file that could be modified appropriately in a seismic attribute and processing software, the spectral attributes were calculated on the seismic line via spectral decomposition following the methodology described in Chapter 1 Section 3.3.

4. Results

The results for Model 2 are shown below. The results for Model 1 and 3 are not shown as these proved to not capture the heterogeneity within the data or were too simplistic based on the current understanding of gas hydrates in the Pegasus Basin.

4.1 Synthetic Well Logs

The results from the synthetic well logs and seismic wavelet convolved with the synthetic well logs for Model 2 is shown in Figure 1. The GSHZ consists of a 440 ft thick interval of shaley sandstone and shale layers with gas hydrate concentration dispersed throughout.
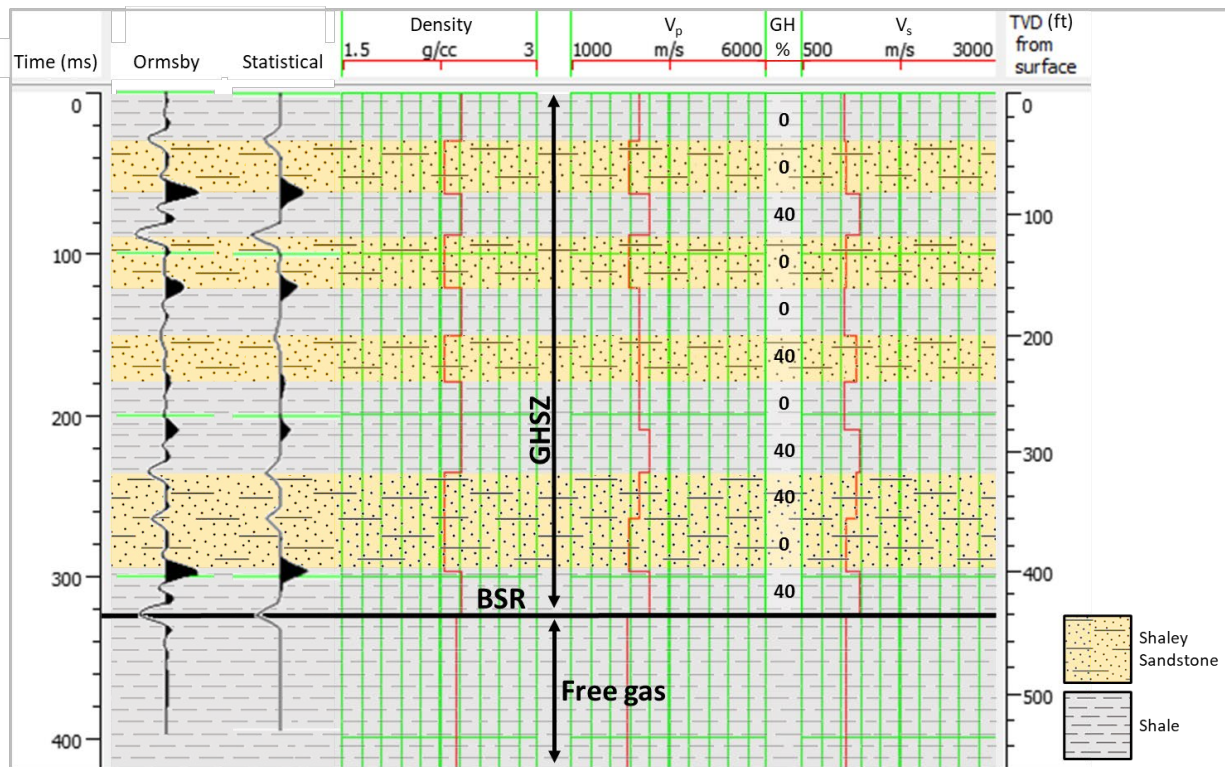
Fig. 1 Synthetic seismic trace and well logs. Track 1, time (ms); track 2, Ormsby wavelet; track 3, statistical wavelet; track 4, density (g/cm^3); track 5, p-wave velocity (m/s); track 6, gas hydrate saturation (%) within the pore space of the rock, with the remaining percentage filled with water; track 7, s-wave velocity (m/s); and track 8, TVD measured from 0 ft below surface

The acoustic impedance *increases* at the base of layer 2, 4, 6, 7, and 10, and *decreases* at the base of layer 1, 3, 5, 8, 9 and 11 (see Table 1 for layer descriptions). Hydrates are present in layer 3, 6, 8, 9, and 11. It is observed that hydrates in layer 3 increase the acoustic impedance at the interface between layer 2 and 3 compared to the acoustic impedance between layer 1 and 2 interface, which contains no hydrates in either layer. Likewise at the interface between layer 10 and 11, which follows the same sand (0% GH) to shale (40% GH) configuration as layer 2 and 3. Indeed, the reflection coefficient (RE) at the interface of a sand to shale sequence is always positive, although the amplitude varies based on hydrate saturation. The acoustic impedance between layer 5 (shale, 0% GH) and 6 (sand, 40% GH) is negative and low amplitude, as is the immediately underlying interface between layers 6 and 7 (shale, 0% GH). Indeed, the amplitudes

at those interfaces are the lowest observed along the seismic trace. At interfaces between the homogeneous lithology with one layer containing hydrates (between layer 7 and 8 and layer 9 and 10), hydrates create an increasing acoustic impedance contrast that would otherwise not exist.
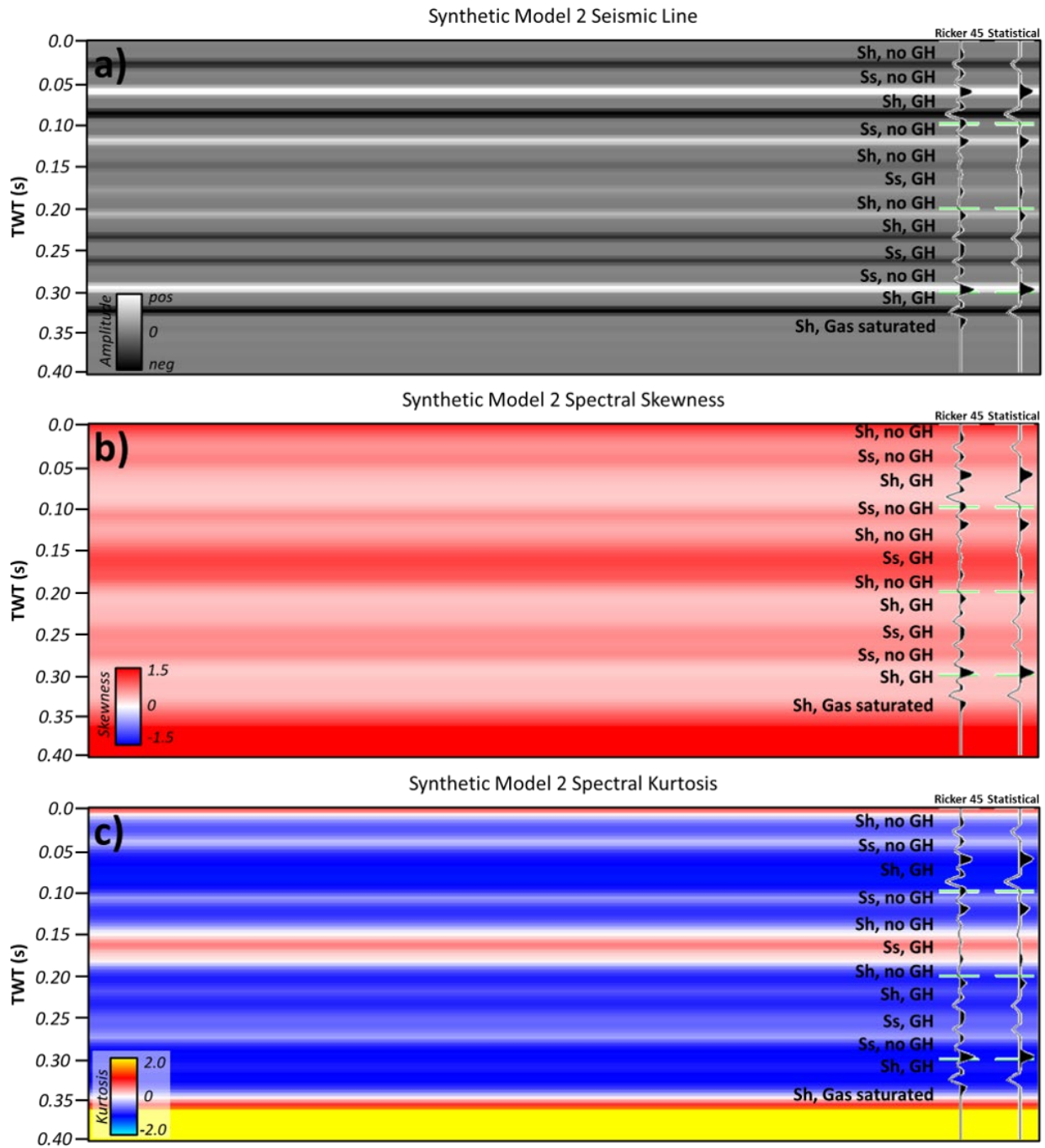

Fig. 2 a seismic amplitude with Ricker and statistical wavelets, and lithology and gas hydrate saturation sequence, **b** spectral skewness with Ricker and statistical wavelets, and **c** spectral kurtosis with Ricker and statistical wavelets
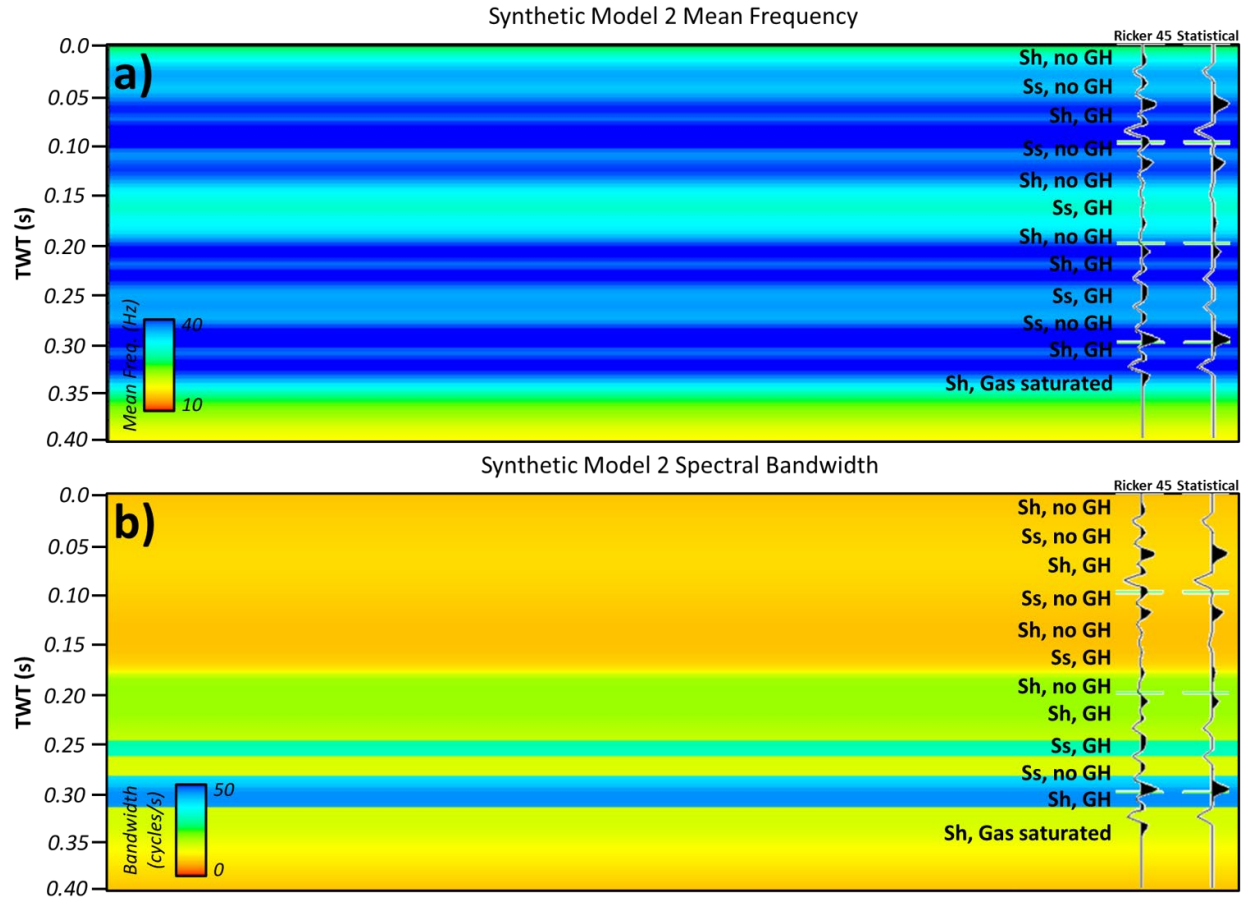
Fig. 3 a mean frequency, in Hertz, and **b** spectral bandwidth, in cycles per second, for the statistical wavelet scenario

4.2 Spectral Shape Attributes from Statistical Wavelet Synthetic

The synthetic seismic line follows an amplitude variation described by the acoustic impedance results in the previous section. For the spectral skewness results, there are no negative skewness values observed. Skewness varies from low, around 0, to greater than 1.5 in the zone below the BSR and GHSZ. Within the GHSZ, the strongest positive skewness (approximately 1.1-1.3) occurs within layer 1, and then in layer 6 and 7, with moderate positive skewness in layer 2, 4, 5, 9, and 10 (approximately 0.7). The lowest skewness is observed in layers 3, 8, and 11 (approximately 0.41). These three layers with the lowest skewness are all shales that contain gas hydrates. The intermediate skewness layers generally are sandstones, with or without hydrates,

and shales with no hydrates make up two of the higher skewness layers. The highest skewness is in a hydrate-saturated sandstone layer (layer 6).

For the kurtosis spectral attribute results, kurtosis ranged from predominately negative to three thin intervals of medium positive kurtosis at the top of the attribute line, in a layer 6, and below the BSR/GHSZ. Kurtosis was strongest negative in layers 2, 3, 10, and 11 (maximum -1.09), medium negative in layers 1, 4, 5, 7, 8, and 9 (maximum -0.89) and nearly every interface between layers was 0 skewness. There was one layer, layer 6, with positive kurtosis within the GHSZ (0.5), and corresponded to a sandstone layer with 40% gas hydrate saturation over- and underlain by hydrate-free shale. The most negative kurtosis occurs along the transition between hydrate-free sandstone and hydrate-saturated shale (between layers 2 and 3, 3 and 4, and 10 and 11. The positive kurtosis response occurs along the top and base interface between a hydrate-free shale, hydrate-saturated sandstone, hydrate-free shale sequence (layer 5 to 6 and layer 6 to 7). The other two positive kurtosis response occurs at the very top of the well log and at the very base, where there is no heterogeneity of data after the BSR.

4.3 Spectral Attributes from Ormsby Wavelet Synthetic

The synthetic seismic line follows an amplitude variation described by the acoustic impedance results in the section 4.1, although the Ormsby wavelet has higher resolution than the statistical wavelet, and therefore, there are more seismic reflectors present compared to the seismic computed from the statistical wavelet (see Figures 2 and 4). For the spectral skewness results (Figure 4b), there are only a few intervals of negative skewness, each of which correspond to a gas hydrate-filled shale layer. The strongest positive skewness results correspond to gas hydrate-filled sand layers or along the interface between two layers with contrasting lithology and hydrate saturation. It is worth noting that the skewness results from the Ormsby wavelet follow the same

trend as the skewness results from the statistical wavelet; the main difference is in the amplitude *of the skewness attribute*. The low positive skewness values in the statistical wavelet seismic correspond to low negative skewness values in the Ormsby wavelet seismic, and the overall strength or amplitude of the strong positive observed in the Ormsby wavelet seismic is lower than that observed in the statistical wavelet seismic. For the spectral kurtosis results (Figure 4c) from the Ormsby wavelet, the kurtosis was overwhelmingly negative throughout, with a few low negative to 0 kurtosis values along the interface between contrasting lithologies and hydrate saturations.
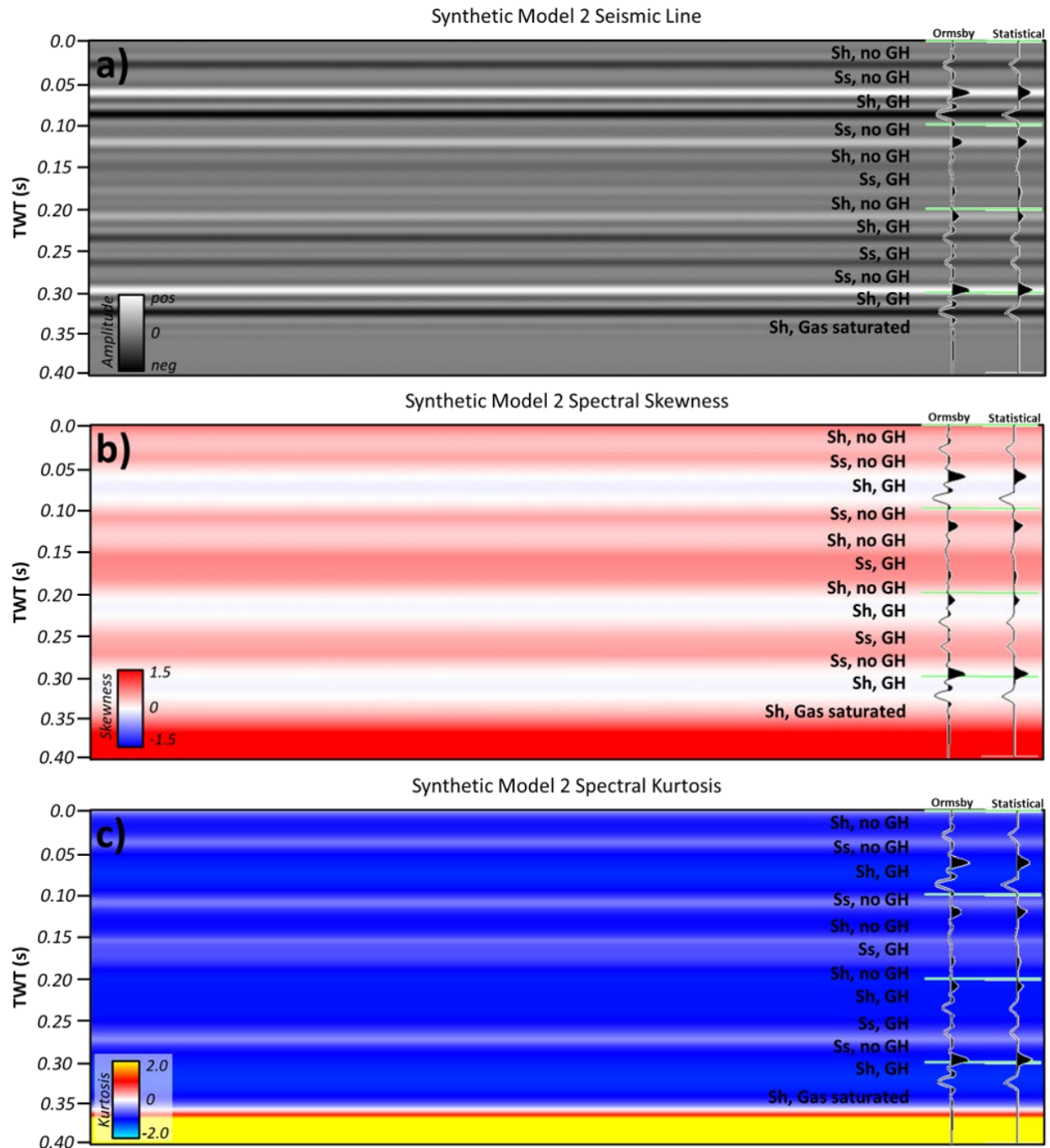
Fig. 4 a seismic amplitude with Ricker and statistical wavelets, and lithology and gas hydrate saturation sequence, **b** spectral skewness with Ricker and statistical wavelets, and **c** spectral kurtosis with Ricker and statistical wavelets
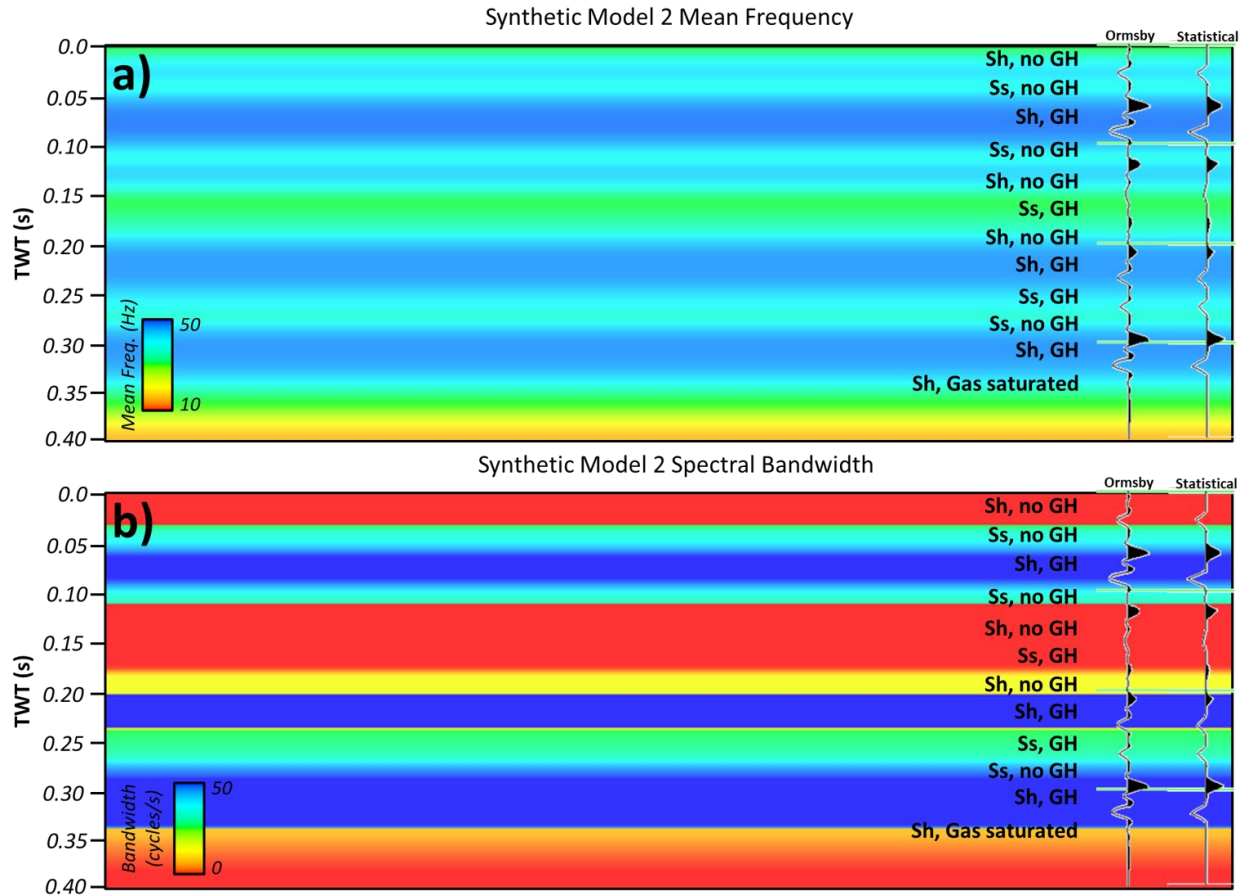
Fig. 5 a mean frequency, in Hertz, and **b** spectral bandwidth, in cycles per second for the Ormsby wavelet scenario

5. Discussion

5.1 Synthetic Well Logs and Seismic Data

It is observed that there is not a linear one-to-one correlation between hydrate saturation increasing the amplitude of the seismic trace, although there are noticeable velocity and density contrasts between layers of differing lithology and/or hydrate saturation. It is likely that the lack of correlation within this particular synthetic dataset is due to the actual rock properties and the similarities in those values for each respective layer. For example, the p-wave velocity of a hydrate-filled sand (2761.98 m/s) is very similar to that of a hydrate-free shale (2726.24 m/s). [See Table 2 for a complete description of rock properties and values used to create the synthetic well

logs.] This creates the low impedance contrast between the hydrate filled sand layers and a hydrate-free shale layer, while the opposite combination of hydrate-filled shale (V_p of 3022.10 m/s) to hydrate-free sand (V_p of 2451.62 m/s) contains a quite large positive reflection coefficient. It is important that one considers not only the hydrate presence (or lack thereof), but also the underlying rock properties, when analyzing the impact of hydrates on the amplitude of the seismic waveform.

5.2 Spectral Shape Attributes from the Statistical Wavelet

The particularly low skewness responses all correspond to layers of shale with no hydrate saturation or the interface between two shale layers with hydrate saturation in one of the layers, with the highest skewness was in a hydrate-saturated sandstone layer. Based on these results, it does not appear that hydrates alone are impacting attribute responses, at least not in a one-to-one relationship. What is happening may better be understood when compared to the frequency of the seismic data. Ever layer with low skewness corresponds to a layer of higher frequency in the mean frequency attribute, calculated from spectral decomposition. The highest values of skewness, on the other hand, correspond to lower frequencies. Although the total range of frequencies represented is small (approximately 20-42 Hz), there is a distinct contrast between zones of high and low skewness in the respective frequency zones. Therefore, it seems more likely that skewness is related to variations in frequency than the actual amplitude of the seismic trace; as was observed in the hydrate-filled sand layer with high skewness, the amplitude of the seismic trace was very low. Hydrate saturation alone did not appear to be the controlling factor on skewness response, but rather the frequency variations observed in each zone. However, the frequency variations are likely tied to hydrates, but without applying an attenuation factor, it is difficult to estimate the true impact of hydrates on skewness.

It appears that positive kurtosis, at least as observed in this simplified model, is tied to low amplitude variations along the seismic trace. The positive kurtosis occurs within the GHSZ only where there was a very low impedance contrast in the original acoustic impedance log and corresponding seismic trace. At the top of the GHSZ, the data contains no heterogeneity, and therefore, no contrast until the first interface. Likewise for the positive kurtosis observed below the BSR. Considering kurtosis in terms of the bandwidth or tailed-ness of the data, positive kurtosis is showing that there is a narrower bandwidth of data, or very large tails. That leads to the explanation that the data contains a large amount of outliers, which is not intuitive for layers with consistent rock properties throughout. Perhaps more intuitive is to think in terms of the amplitude and frequency of the data. In a thick, homogeneous layer, such as those described in this model, there will be a narrow range of frequencies within *synthetic* data given that the model used a synthetic wavelet and the rock properties were consistent throughout. This effect is likely responsible for the positive kurtosis in zones with high similarity (either because of lithology or GH saturation or a combination of the two giving similar rock property values), and therefore, similar (and low) frequencies. In real seismic data, there will be a significant amount of heterogeneity and frequency variations within the data that will likely result in a broader bandwidth, and subsequently, lower to negative kurtosis.

Within the model presented here, the negative kurtosis corresponds to a broader bandwidth and therefore, a larger range of frequencies. This negative kurtosis corresponds to layers that have significantly varying rock property values, such as between a hydrate-free sandstone and a hydrate-saturated shale. Therefore, kurtosis may be better described in terms of how it describes the contrast *between* layers or the variation *within* a thick, heterogeneous lithology sequence. Likely, however, at the scale of most seismic resolution, kurtosis will not be applicable to resolve

heterogeneity within individual lithologies but on a resolve larger-scale variations between layers and sequences.

Although kurtosis did not appear to be tied directly to gas hydrate saturation, at least in the fashion expected, it is closely related to variations occurring in the frequency spectrum of the data. Likely, the model is too simplistic, and without a proper attenuation factor applied, the true nature of hydrate's impact on attenuation is not being captured by density and velocity and subsequent seismic data.

5.3 Spectral Attributes from the Ormsby Wavelet

The skewness results observed in the Ormsby wavelet seismic are very similar to that observed in the statistical wavelet seismic, albeit with a lower amplitude *of the skewness* response. Therefore, the interpretation of these skewness responses are generally consistent for both wavelet scenarios. The main consideration is that the Ormsby wavelet contains inherently lower positive skewness than the statistical wavelet (see Appendix E Figure 1 and 2), which impacts the skewness results for that scenario. The kurtosis results are also impacted by this wavelet shape. While the spectrum from the statistical wavelet varied slightly across the seismic data, the spectrum for the Ormsby wavelet was very consistent throughout, following the Ormsby bandpass values that were used to create the wavelet. Additionally, the shape of the spectrum was consistent for the negative kurtosis example (see Figure 4). Therefore, kurtosis was inherently negative across almost the entirety of the Ormsby wavelet seismic, even where gas hydrate layers were present. With respect to gas hydrates, then, the Ormsby scenario did not provide much utility in distinguishing layers of gas hydrates or how attenuation varies throughout the GHSZ.

5.4 Model Limitations

Based on the initial results and interpretations from this brief investigation into spectral attribute response on gas hydrates in synthetic seismic data, it is observed that the model, whether based on the statistical or Ormsby wavelet, was not able to capture the heterogeneity that occurs intrinsically within hydrates to cause attenuation. From the Cordon et al (2006) study, it was shown that synthetic seismic data showed little to no amplitude losses in gas hydrates when no Q-factor was applied. The results in Model 2 reflected a similar response. Therefore, a limitation to this study was that, without applying attenuation to the model, the model was only able to capture the background elastic heterogeneity from the varying lithology and hydrate layers, but not attenuation itself. However, these results are still useful for illustrating the *intrinsic*, although poorly understood, mechanism of attenuation that is observed in gas hydrates, as well as highlighting anomalies that may be caused by hydrates when a proper Q-factor is applied.

Another possible limitation is the wavelet used to compute the synthetic seismic. Based on results from the statistical wavelet used in this model, it is observed that the wavelet has inherently positive skew. While real-world seismic data also exhibits a similar statistical shape, using an Ormsby wavelet may produce data that is more normalized, or at least, less inherently skewed, however this is observed to create more inherent negative kurtosis, which illustrates that synthetic models can often fall short of the complexities that are present within real-world data.

6. Conclusions

The model presented here was created from synthetic well logs and synthetic seismic data. Spectral attributes skewness and kurtosis were computed on the 2D seismic data. The results showed that skewness and kurtosis lacked a clear one-to-one correlation with hydrate saturation, but *were* directly correlated with frequency variations. Likely, the model was unable to tie the

spectral shape attributes to hydrate saturation because rock physics equations used to create the model do not include metrics for frequency and attenuation, of which attenuation is especially critical for gas hydrate studies. However, the model was able to capture the elastic property variations that are expected in hydrates, namely, reduced porosity and sonic velocities. Future workflows should include application of attenuation metrics in order to properly capture the heterogeneity within a gas hydrate setting. Additionally, skewness and kurtosis attributes calculated from seismic data should be correlated with confirmed gas hydrate-bearing intervals in well log data to verify the model's accuracy and advantage for future applications in gas hydrate settings.

7. References

Bünz S, Mienert J, Vanneste M, Andreassen K (2005) Gas hydrates at the Storegga Slide: Constraints from an analysis of multicomponent, wide-angle seismic data. GEOPHYSICS 70:B19–B34. https://doi.org/10.1190/1.2073887

Cordon I, Dvorkin J, Mavko G (2006) Seismic reflections of gas hydrate from perturbational forward modeling. Geophysics 71:F165–F171. https://doi.org/10.1190/1.2356909

Cunha A, Pochet A, Lopes H, Gattass M (2020) Seismic fault detection in real data using transfer learning from a convolutional neural network pre-trained with synthetic seismic data. Computers & Geosciences 135:104344. https://doi.org/10.1016/j.cageo.2019.104344

Dvorkin J, Gutierrez MA, Grana D (2014) Seismic Reflections of Rock Properties. Cambridge University Press, https://doi.org/10.1017/CBO9780511843655

Dvorkin JP, Mavko G (2006) Modeling attenuation in reservoir and nonreservoir rock. The Leading Edge 25:194–197. https://doi.org/10.1190/1.2172312

Dvorkin J, Mavko G, Gurevich B (2007) Fluid substitution in shaley sediment using effective porosity. GEOPHYSICS 72:O1–O8. https://doi.org/10.1190/1.2565256

Guerin G, DS Goldberg (2002) Sonic waveform attenuation in gas hydrate-bearing sediments from the Mallik 2L-38 research well, Mackenzie Delta, Canada. J Geophys Res 107:2088. https://doi.org/10.1029/2001JB000556

Hamilton EL (1980) Geoacoustic modeling of the sea floor. The Journal of the Acoustical Society of America 68:1313–1340. https://doi.org/10.1121/1.385100

Hato M, Inamori T, Bahar A, Matsuoka T (2004) Application of AVO Analysis to Seismic Data for Detection of Gas below Methane Hydrate Stability Zone in Nankai Trough Area. Resource Geology 54:105–113. https://doi.org/10.1111/j.1751-3928.2004.tb00192.x

Hornbach MJ, Holbrook WS, Gorman AR, et al (2003) Direct seismic detection of methane hydrate on the Blake Ridge. Geophysics 68:92–100. https://doi.org/10.1190/1.1543196

Kumar D, Sen MK, Bangs NL (2006) Seismic characteristics of gas hydrates at Hydrate Ridge, offshore Oregon. The Leading Edge 25:610–614. https://doi.org/10.1190/1.2202665

Li F, Verma S, Zhou H, et al (2016) Seismic attenuation attributes with applications on conventional and unconventional reservoirs. Interpretation 4:SB63–SB77. https://doi.org/10.1190/INT-2015-0105.1

May B, Hron F (1978) Synthetic seismic sections of typical petroleum traps. Geophysics 43:119-1147. https://doi.org/10.1190/1.1440883

Riedel, M, Willoughby EC, and Chopra S (2010) Geophysical Characteristics of Gas Hydrates. Society of Exploration Geophysicists Geophysical Developments Series No. 14. https://doi.org/10.1190/1.9781560802197

Appendix A, Gas Hydrate Stability Zone Profile and Schematic
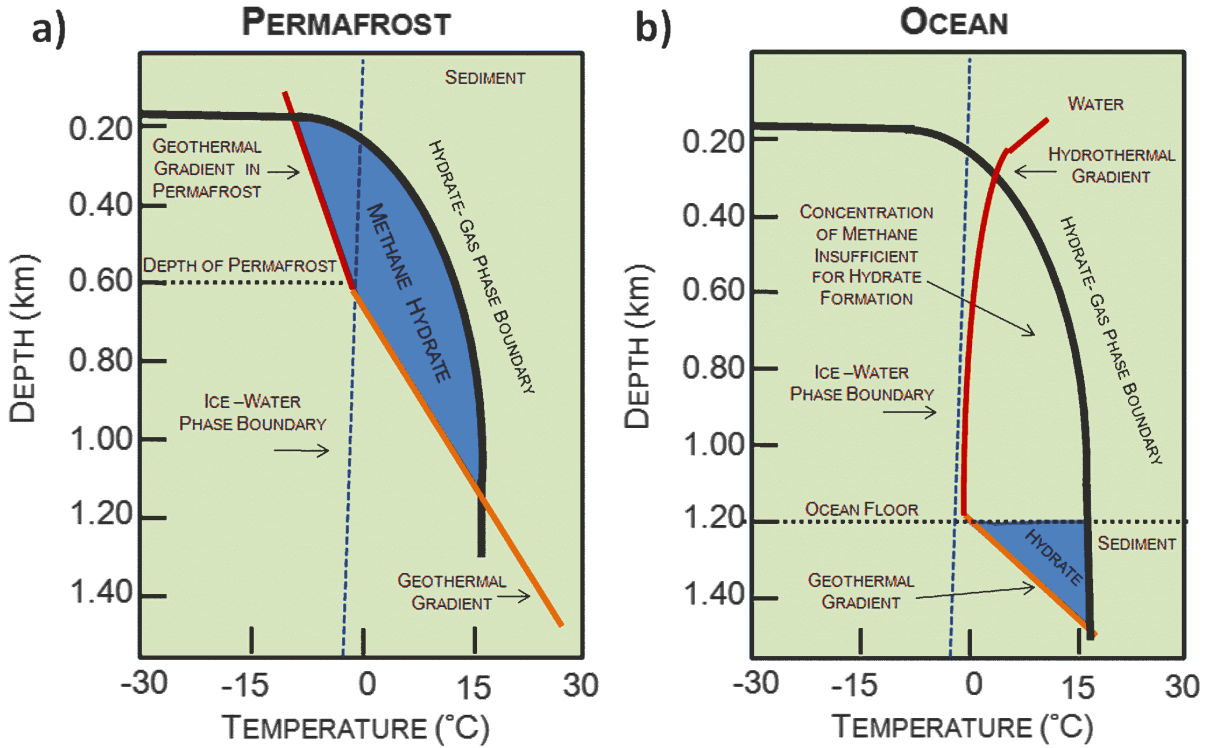
Appendix A Fig. 1 a GHSZ profile for a permafrost setting and **b** GHSZ profile for an oceanic setting. Figure from Harison (2010) http://large.stanford.edu/courses/2010/ph240/harrison1/. Accessed 21 February 2023

Appendix B, Supplemental Mathematics and Equations

Appendix B.1 SOM Implementation and Detailed Mathematics

A detailed outline of the SOM implementation in the AASPI som3d volumetric classification module is available through the AASPI website at the University of Oklahoma's Mewbourne College of Earth and Energy: https://mcee.ou.edu/aaspi/documentation.html

Appendix B.2 Attenuation math

The attenuation coefficient or spatial attenuation factor, α, is defined by Mavko et al. (2009) and Dvorkin et al. (2014) as (Equation 1)

$$A(x, t) = A_0 \exp[-\alpha(\omega)x] \exp[i(\omega t - kx)] \qquad \text{Equation 1}$$

where A is the amplitude of the signal, A_0 is ithe input-signal amplitude, t is the time, x is the spatial coordinate, ω is the angular frequency, f is the linear frequency, and k is the wavenumber. The attenuation coefficient is the exponential decay coefficient of a harmonic wave (Mavko et al., 2009) and is related to the inverse quality factor Q^{-1} such that (Equation 2)

$$\alpha = \frac{Q^{-1}\pi f}{V} \qquad \text{Equation 2}$$

where V is the phase velocity (Dvorkin et al., 2014).

Appendix C, Seismic Spectra Analysis

Attribute Response:	Time Start (seconds, TWT)	Time End (seconds, TWT)	Crossline Start (cdp)	Crossline End (cdp)
Negative skewness	3.62	3.732	3900	5250
Positive skewness	3.8	3.976	4250	5250
Negative kurtosis	3.616	3.736	4500	5170
Positive kurtosis	3.8	3.964	4500	5180

Appendix C Table 1 Cutoff values for seismic spectra computation where strong negative and strong positive skewness and kurtosis attribute responses occur.
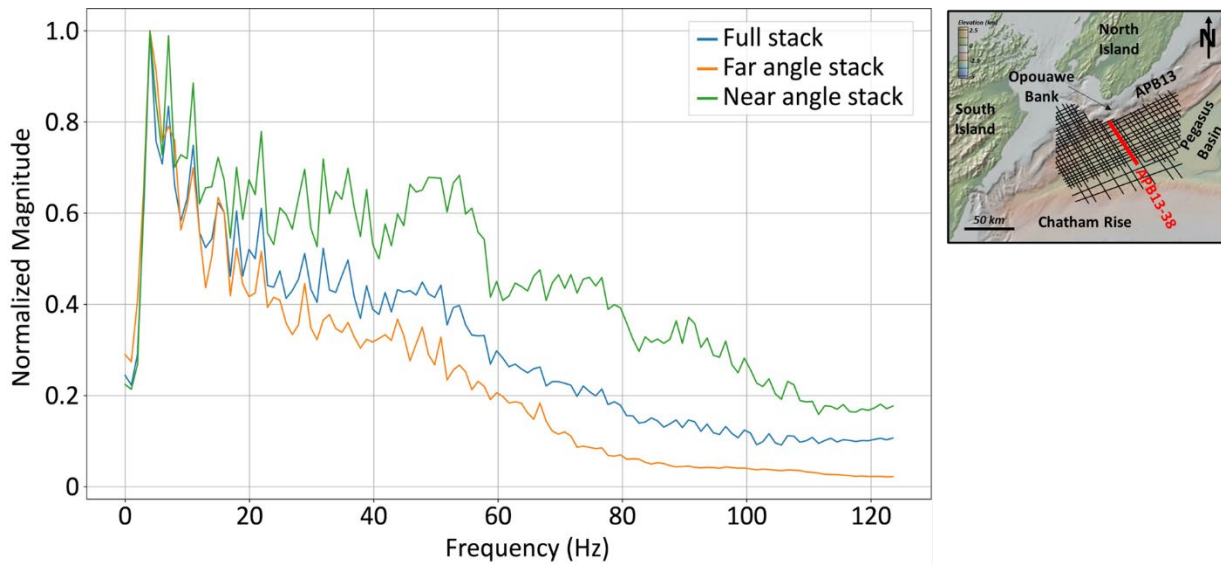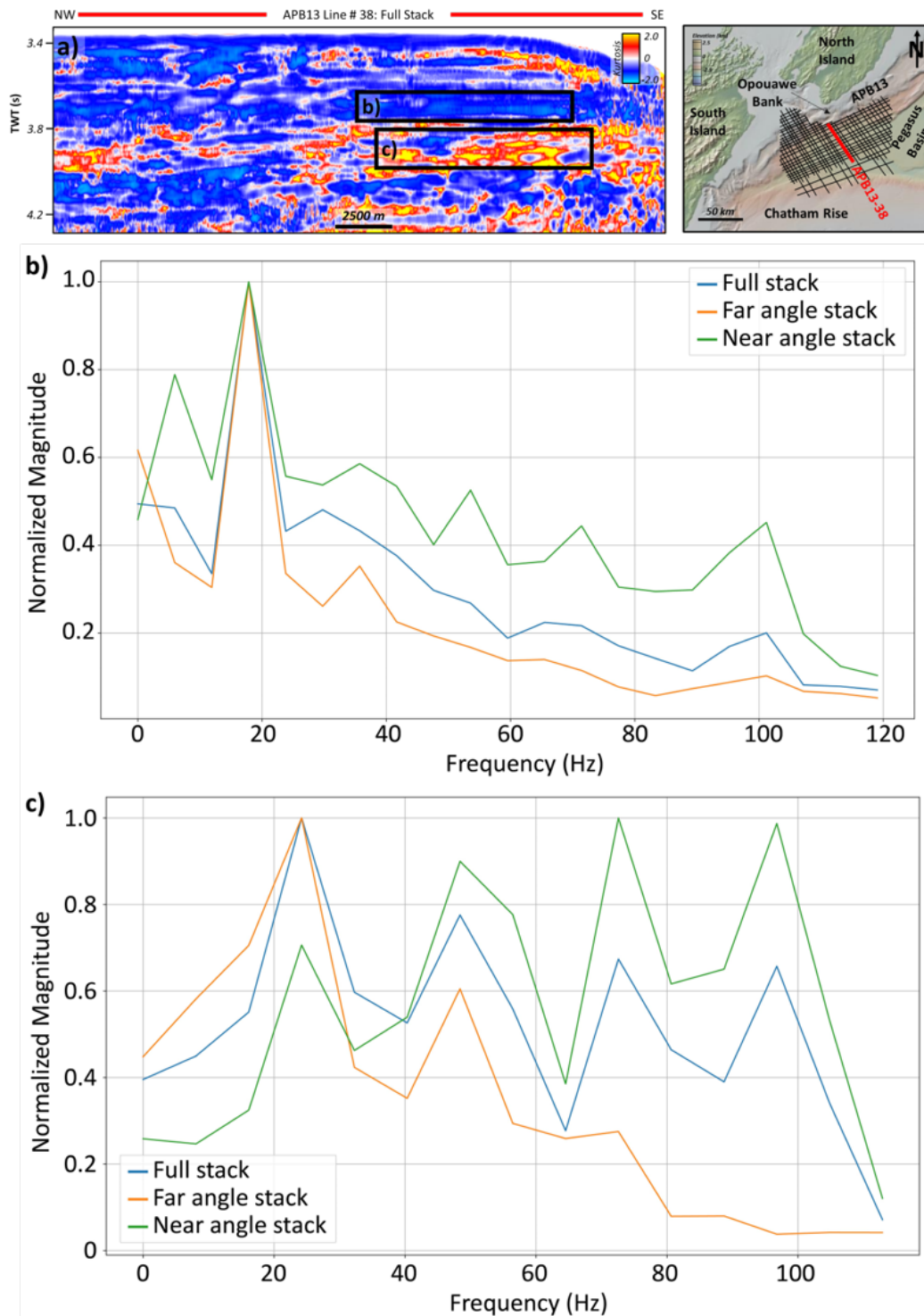

Appendix C Fig. 1 Amplitude spectrum calculated across the cropped interval shown in Figure 6b for the full, far, and near angle stacks; seafloor bathymetry map from GeoMapApp

Appendix C.1 Seismic Spectra and Skewness Variations
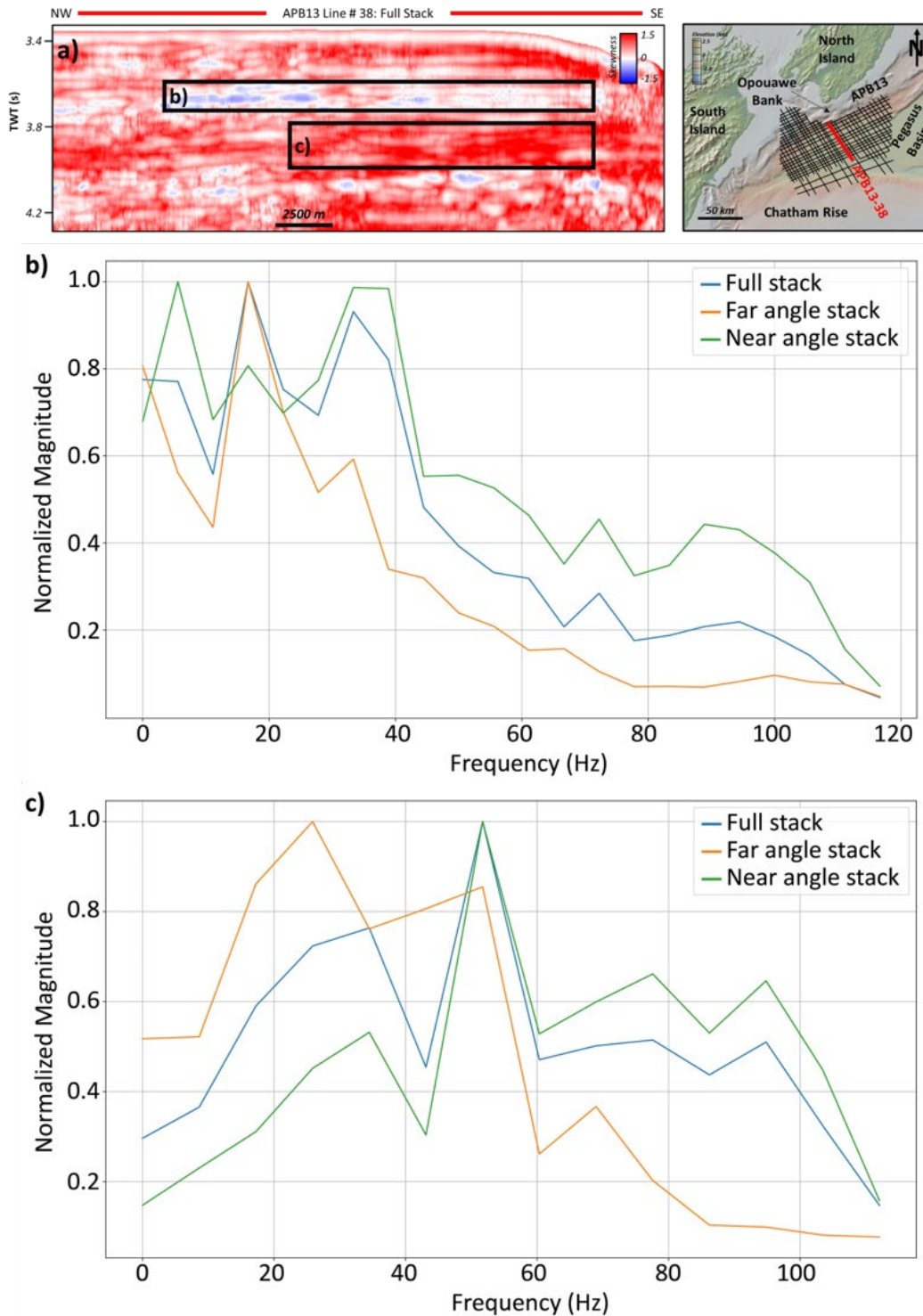
Appendix C Fig. 2 a skewness attribute calculated from the full stack seismic line, **b** amplitude spectrum calculated between 3.62 – 3.732 seconds (TWT) and 3900 – 5250 cdp, **c** amplitude spectrum calculated between 3.8 – 3.976 seconds (TWT) and 4250 – 5250 cdp; seafloor bathymetry map from GeoMapApp

Appendix C.2 Seismic Spectra and Kurtosis Variations

Appendix C Fig. 3 a kurtosis attribute calculated from the full stack seismic line, **b** amplitude spectrum calculated between 3.616 – 3.736 seconds (TWT) and 4500 – 5170 cdp, **c** amplitude spectrum calculated between 3.8 – 3.964 seconds (TWT) and 4500 – 5180 cdp; seafloor bathymetry map from GeoMapApp

Appendix D, SOM Case 3

SOM Case 3 was implemented between two horizons that were modified from the original ocean bottom seismic horizon and BSR seismic horizon that were used to calculate SOM Case 2. For SOM Case 3, the purpose was to exclude the "outlier" or "anomalous" clusters that classified the ocean bottom and BSR facies. Therefore, two new seismic horizon were used: an ocean bottom reflector -30 units (units specific to the seismic interpretation software) and the BSR +20 units. The SOM was implemented between these two horizons at the same user-defined parameters as SOM Case 1 and Case 2. The results are shown below.
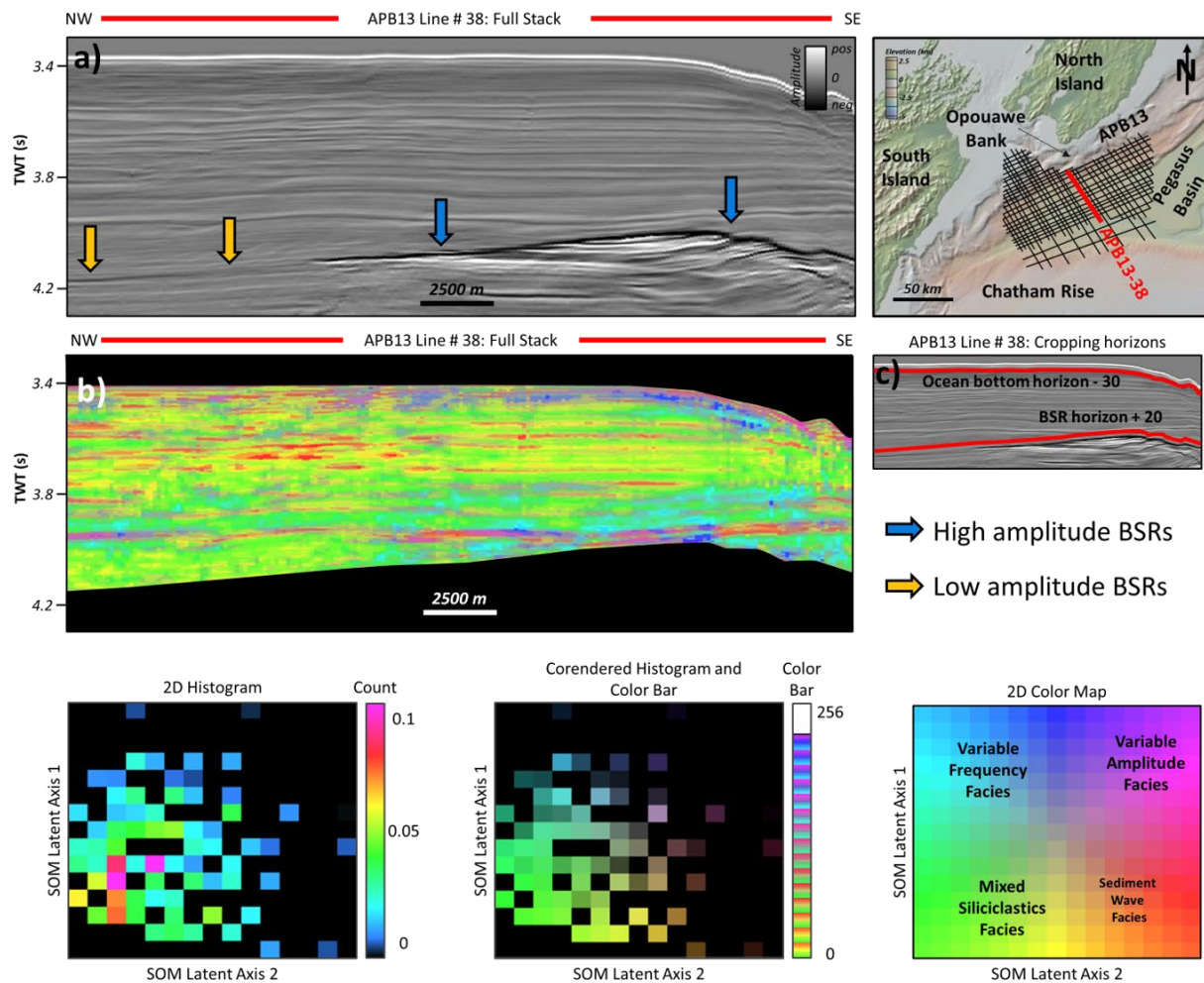

Appendix D Fig. 1 a full angle stack seismic line with high and low amplitude BSRs, **b** SOM results calculated from the full stack seismic line, and **c** cropping horizons. The histograms and 2D color map are used to determine the SOM colors represented in **Fig 1b**

The results for SOM Case 3 are able to highlight the subtle changes in amplitude that were likely overprinted by the high amplitude ocean bottom and BSR (compare the histogram for SOM Case 1 and 2 to SOM Case 3) in SOM Case 1 and Case 2. However, it appears that the attenuation variations classified by the Variable Frequency Facies cluster is relatively unchanged within Zone 3, whereas in Zone 1, toward the Hikurangi Channel, there are slightly more dark blue colors that may be due to amplitude variations throughout that zone, rather than attenuation variations alone.

Appendix E, Statistical and Ormsby Wavelets for Synthetic Studies
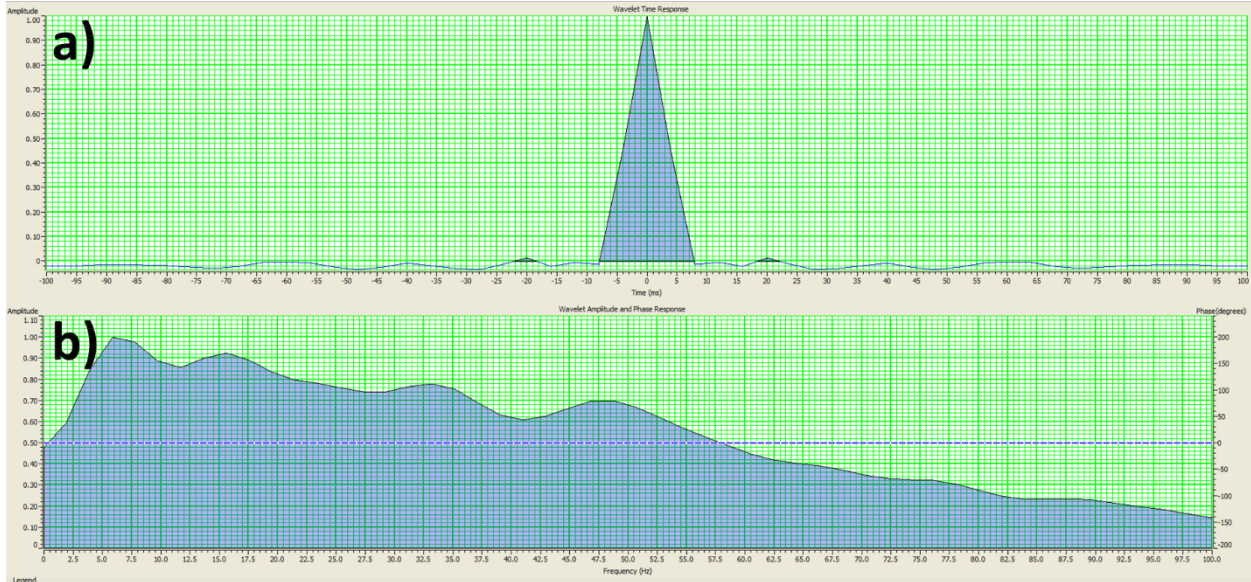
Appendix E Fig 1 a statistical wavelet and **b** spectrum from statistical wavelet seismic
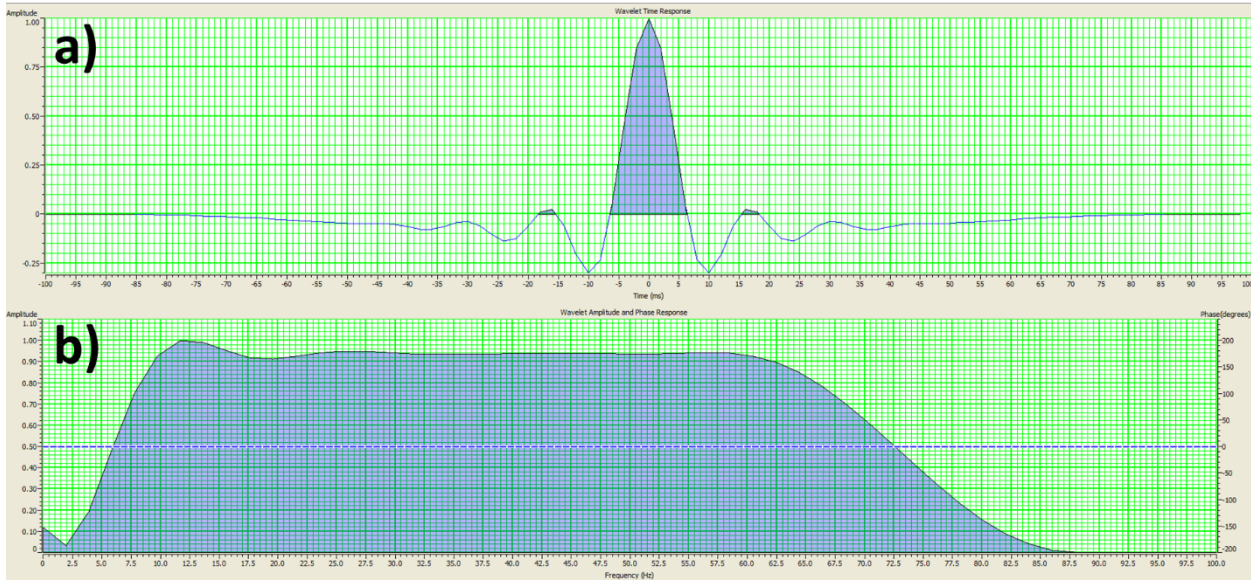
Appendix E Fig 2 a Ormsby wavelet and **b** spectrum from Ormsby wavelet seismic